Integrated multi-wavelength transmitter using filtered-feedback

Please check the document version of this publication:

• A submitted manuscript is the version of the article upon submission and before peer-review. There can be important differences between the submitted version and the official published version of record. People interested in the research are advised to contact the author for the final version of the publication, or visit the DOI to the publisher's website.
• The final author version and the galley proof are versions of the publication after peer review.
• The final published version features the final layout of the paper including the volume, issue and page numbers.

Link to publication

Download date: 04. Oct. 2023

Integrated Multi-Wavelength Transmitter using Filtered-Feedback

Integrated Multi-Wavelength
Transmitter using Filtered-Feedback

PROEFSCHRIFT

ter verkrijging van de graad van doctor aan de
Technische Universiteit Eindhoven, op gezag van de
rector magnificus, prof.dr.ir. C.J. van Duijn, voor een
commissie aangewezen door het College voor
Promoties in het openbaar te verdedigen
op dinsdag 1 oktober 2013 om 16.00 uur

door

Jing Zhao

geboren te Xi'an, China

Dit proefschrift is goedgekeurd door de promotoren:

prof.dr.ir. M.K. Smit
en
prof.dr. D. Lenstra

Copromotor:
dr. X.J.M. Leijtens

This thesis is dedicated to my parents and grandparents for their endless love, support and encouragement.

Contents

iii

List of Acronyms

ALMA   Atacama millimeter array

AOM   Acousto-optic modulator

APL   Analog photonic link

AR   Anti-reflection

ATA   Allen telescope array

AWG   Arrayed waveguide grating

AWGL   Arrayed waveguide grating based laser

BPM   Beam propagation method

CATV   Community antenna television

CW   Continuous wave

DC   Direct current

DFB   Distributed feedback

DS-DBR   Digital supermode distributed Bragg reflector

E/O   Electrical to the optical

EA   Electro-absorption

EAM   Electro-absorption modulator

EDFA   Erbium-doped fibre amplifier

ENA   Electrical network analyser

EO   Electro-optic

EO	Electro-optic
ER	Extinction ratio
ESA	Electrical spectrum analyser
FDTD	Finite-difference time-domain
FFMWL	Filtered-feedback multi-wavelength laser
FKE	Franz-Keldysh effect
FP	Fabry–Pérot
FPR	Free propagation region
FSR	Free spectral range
FWHM	Full width at half maximum
GaAs	Gallium arsenide
HD	Harmonic distortion
HR	High-reflective
IMD	Intermodulation distortion
InGaAs	Indium gallium arsenide
InGaAsP	Indium gallium arsenide phosphide
InP	Indium phosphide
IP3	Third order intercept point
ITU	International Telecommunication Union
LE	Lumped element
LEO	Linear electro-optic
LNA	Low noise amplifier amplifier
LOFAR	Low-Frequency array for radio astronomy
MIR	Multi-mode-interference reflector
MPW	Multi-project wafer
MQW	Multiple quantum well

MWL	Multi-wavelength laser
MWP	Microwave photonics
MZM	Mach-Zehnder modulator
O/E	Optical to the electrical
OBFN	Optical beam forming network
OSA	Optical spectrum analyser
PD	Photodiode
PHS	Phase shifting section
PIC	Photonic integrated circuit
PM	Polarisation-maintaining
PR	Partially reflective
QCSE	Quantum-confined Stark effect
QW	Quantum well
RAU	Remote antenna unit
RF	Radio frequency
RO	Relaxation oscillation
ROF	Radio over fibre
SFDR	Spurious-free dynamic range
SG-DBR	Sampled-grating distributed Bragg reflector
SKA	Square kilometer array
SMB	SubMiniature version B
SMSR	Sidemode suppression ratio
SNR	Signal-to-noise ratio
SOA	Semiconductor optical amplifier
SOI	Silicon on insulator
SSG-DBR	Super structure grating distributed Bragg reflector

TIR	Total internal reflection
TW	Travelling-wave
VCSEL	Vertical-cavity surface-emitting laser
WDM	Wavelength division multiplexing
DBR	Distributed Bragg reflector

Chapter 1

Introduction

This chapter provides a general introduction to integrated multi-wavelength transmitters. It reviews the two main components used in transmitters: the multi-wavelength laser and the optical modulator.

1.1 Introduction

The demand placed on the data transport infrastructure by bandwidth-hungry applications and the explosive growth of the internet are pushing the need for fibre optical communications. Transmission of multiple optical channels over the same fibre in wavelength division multiplexing (WDM) systems and Gigabit Ethernet systems provide a simple way to use the unprecedented capacity (signal bandwidth) offered by fibre optics. This multiplexing closely resembles the way radio stations broadcast on different wavelengths without interfering with each other. For a WDM optical network, there are a number of independent wavelength channels that simultaneously transmit data over one physical fibre. In a broadband WDM networking system, the key components are optical transmitters and receivers, which transmit and receive optical signals at different wavelengths.

Currently, in wavelength division multiplexing networking systems, the optical transmitters and receivers are mostly based on a number of fixed-wavelength laser devices that are either directly modulated with the data to be sent, or are combined with an external modulator for improved performance. After light generation and modulation, the signals will be multiplexed or directly sent to the next element, where they may be amplified, switched or experience other processing. Separate lasers and dedicated modulators are used for each wavelength transmission channel. However, using lasers and associated components for each wavelength channel can be very costly and inefficient. A possible way to improve the

multi-wavelength transmitter system is by monolithically integrating multiple laser sources and electro-optic modulators on a single chip, thus forming an integrated multi-wavelength transmitter. Especially when more functionalities are required in the system, such photonic integrated circuits (PICs) will be of key importance in WDM networks. They can dramatically reduce the size and cost of network elements as well as increase their reliability, by reducing the number of discrete components and by reducing the electrical and optical interconnections between them [1].

1.2   Photonic integrated circuit

In 1969, a remarkably prophetic paper [2] articulated a vision of a new art: integrated photonics. The paper showed a vision for integrated laser and device circuitry. If photonic integrated circuits could be realized, they would have many attractive features:

- Monolithic interconnection of device elements, providing simpler packaging and assembly, using standard processes can greatly reduce component cost: all the components in the circuit are monolithically integrated on the same chip, fabricated together, and packaged on the chip at circuit level.

- High reliability, less interfaces. As all the components are on the same chip and are connected by waveguides on the chip, the number of interfaces is much reduced, which in turn makes the circuit more reliable and robust.

- High functionality. Various active and passive components can be integrated on a single chip, with many more functional elements at very low incremental cost. This gives room for highly creative circuit designs.

- High phase stability. An accurate phase control over the circuit is very difficult to realize in discrete devices connected with fibres. A high phase stability can only be realised on the same integrated chip structure, and it can provide the device with excellent phase matching which permits interferometric structures.

- Lower power consumption. With less interfaces there is less loss in the integrated circuit, which also leads to a reduced power consumption.

Although photonic integrated circuits could also bring different challenges, such as packaging, crosstalk, thermal management, by the time of writing the 1969 paper, work was beginning in the direction indicated and the goals were being identified. Throughout the years to follow, this vision stimulated a wide spectrum of developments. We mention the development of integrated optic materials and technologies, the development of integrated optic analysis concepts and tools, the development of integrated optic passive and active components. After all the hard work that has been done, these areas have matured sufficiently for us to put them together to create photonic integrated circuits.
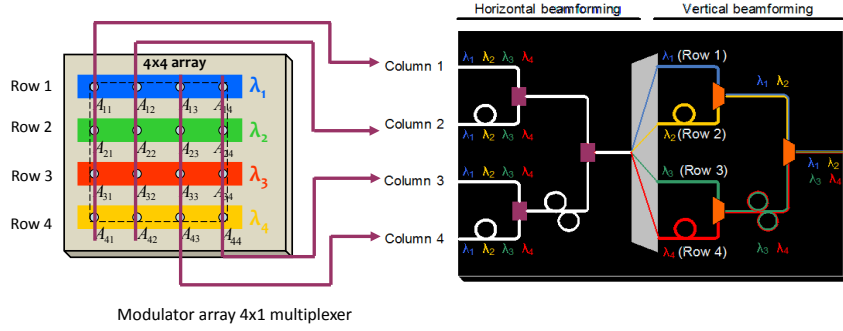
Figure 1.1: Schematic of a smart-antenna receiver system. In this work the multi-wavelength laser, monolithically integrated with electro-optical modulators is being researched. [6]

1.3 Background information

Recently, part of a Dutch national project MEMPHIS [3], was devoted to the development of a phased array smart antenna system. The system employs integrated optical beam forming networks (OBFNs) to realize large bandwidths, and true time delay (squint-free) performance [4]. The optical-ring-resonators-based true-time-delay units can be cascaded in a binary tree topology and tuned for continuously-adjustable broadband time delay. Nonetheless, with large number of antenna elements, the OBFN may become very complex [5]. In order to make the system capable to handle hundreds or thousands of antenna radars, while keeping a low system complexity and cost, a novel scheme using optical wavelength division multiplexing (WDM) in combination with a multi-wavelength OBFN is considered. The basic idea is to create multiple signal paths on the same beamformer, by using different wavelength light signals to carry different radio frequency (RF) antenna signals and multiplex them to a common waveguide. In this way, a single delay line carries the signals of different antenna elements, thus significantly reducing the network complexity. Fig. 1.1 illustrates the general system approach for a 4×4 antenna array. Instead of having 16 channels time delay for each element, the delay of the 16 channel signals are processed horizontally and vertically in two consecutive stages. Signals from each row of the antenna elements are modulated on different wavelength, and the signals from each column on a different wavelength can be multiplexed and share the same beam forming paths for horizontal beam forming. After that, the signals of different wavelength are demultiplexed, and experience the vertical beam forming. This WDM approach allows reduction of network complexity (from N^2 to $2N$), which in turn will lead to higher integration capability and improved scalability to large arrays [7].

The goal of our work in this framework is to design, fabricate and characterize the four channel WDM transmitter part, the monolithically integrated indium phosphide (InP) chip of compact multi-wavelength lasers (MWL) with fast electro-optical modulators for this antenna analog photonic link with optical beam forming network. In this smart antenna (phased array) system (see Fig 1.1), for each column of of the antenna array, the RF signals from four antenna element will be modulated on the four different wavelength of laser signals by the integrated multi-wavelength transmitter (MWT) chip, then the multiplexed signal will be processed by the optical beam forming network (OBFN).

Within the system, there are some hard specifications required for the multi-wavelength transmitter: (i) As this smart antenna approach aims at a receiver demonstrator working at 2 to 5 GHz, the modulator bandwidth should cover the range of 2 to 5 GHz. (ii) The linewidth of the laser should be able to fit inside the passband of the ring resonator, which is 2 MHz, which means the linewidth of the laser should be lower than 2 MHz. (iii) The channel spacing of the multi-wavelngth laser should be accurate according to the design, which will need to match the free spectral range (FSR) of the ring resonator. Moreover, due to the application in the smart antenna system, the analog performance is relevant for the transmitter. However, there was no hard requirement defined within this project. In this thesis, the multi-wavelength transmitter is discussed in the context of an analog photonic link. But in general, the multi-wavelength transmitter (MWT) is a versatile component, which is most often used for digital communication in WDM systems, for which the market is even larger than that for the analog photonic link.

1.4   Analog photonic link

In an analog photonic link (APL), an RF signal is converted into an optical signal, transmitted via an optical fibre and subsequently restored to the electrical format at the recipient's end using a photodetector. Taking advantage of the low propagation loss of the optical fibre, the APL has become the heart of an emerging field of microwave photonics (MWP), in which various functionalities like generation, distribution, control and processing of RF signals are explored.

The APLs have been used in various systems involving the generation, processing, control and distribution of RF or microwave signals. Here we will review some of the notable applications of APLs.

CATV Distribution Network

During 1970s, using optical fibres to replace copper cables in the CATV (Community antenna television) distribution networks were investigated [8, 9]. The idea was to modulate the optical carrier with multiple CATV signals, thereby exploiting the

available bandwidth of the optical fibres. This technique is also known as the sub-carrier multiplexing. However, since the system uses a large number of RF carriers (in some cases up to 110 carriers), it requires high linearity and, moreover, low noise.

Radio over Fibre for Wireless Systems

Radio over fibre (ROF) systems use APLs to distribute RF signals from a central location to remote antenna units (RAUs). This allows the RAUs to be very simple, because they only need to contain electrical to optical and optical to electrical conversion devices and amplifiers. As the low-loss of the optical fibre permits the shift of most advanced functions away from the antenna, functions like coding, modulation, multiplexing and up-conversion can be performed at a central location [10]

Antenna Remoting

Using APLs for antenna remoting is attractive in military and warfare applications. A typical application in this field requires the APL to bridge very short distance which is less than 100 m [11]. The APL is used to replace the coaxial cables due to its low propagation loss, wide bandwidth, small size, light weight, flexibility for system reconfiguration and immunity to electromagnetic interference [12]. The large number of coaxial cables used on military platforms make the size of the cable plant a significant issue for avionic, submarine, and even surface ship applications. Especially in avionics applications, the heavy weight of these cables becomes an issue.

Radio Astronomy Applications

The use of APLs in radio astronomy is mainly directed towards antenna remoting [13] and local oscillator signal distribution [14]. To increase the sensitivity, radio telescopes nowadays are designed as arrays of small antennas capable of very large collecting areas. Some of the examples of these antenna arrays are the Allen Telescope Array (ATA) [15], Atacama Large Millimeter/submillimeter Array (ALMA) [16], the Low Frequency Array (LOFAR) [17] and the Square Kilometer Array (SKA) [18]. These arrays contain of a large number of elements, covering a large area.

APLs can be used in such a large scale antenna array to distribute the signals among the antenna elements (or antenna tiles) and the connections to the central processor. The APLs offer low propagation loss independent of the frequency in contrast with the coaxial cables, where the loss increases with the carrier frequency.

1.5   Review of the state-of-the-art

The monolithic photonic integrated transmitter enables great consolidation of system functionality and compared to discrete optical devices, it has huge advantages of reduced volume and packaging costs. In order to carry out the monolithic integration of the multi-wavelength transmitter, we need to investigate the two essential parts of this integrated circuit, (i) multi-wavelength lasers and (ii) optical modulators. In the following sections, an overview will be given of different types of optical modulators, multi-wavelength lasers, and their possibility to be implemented in this integration, as well as the published result of these devices.

1.5.1   Multi-wavelength laser

In a WDM system, the multi-wavelength transmitters need a light source which provides multiple wavelengths. Most multi-wavelength transmitters are currently built with discrete laser components, but discrete components takes more space, have high packaging cost and the burden from multiple fibres and connectors. Integration of lasers into a multi-wavelength laser array has been proposed as a promising approach, which can generate multiple wavelengths simultaneously. Different ways of realizing integrated multi-wavelength lasers have been reported in the literature, both hybridly and monolithically integrated, e.g. (i) by cascading InP micro-disk lasers [19], by vertical-cavity surface-emitting lasers (VCSELs), (ii) by semiconductor optical amplifier based ring lasers [20], (iii) by combining the signals of an array of distributed feedback (DFB) [21, 22] or distributed Bragg reflector (DBR) lasers with a power combiner [23], or (iv) by combining in one cavity a number of semiconductor optical amplifiers (SOAs) as well as an intra-cavity filter like an arrayed waveguide grating (AWG) [24]. Here, we present a short discussion of a few of these types.

VCSELs and microdisk lasers

In a VCSEL, light is resonating in a vertical cavity between two Bragg mirrors, and then emitted perpendicular to the layer stack, from the top surface. The Bragg reflectors consist of alternate layers of low and high refractive indices. VCSELs have a number of nice characteristics. (i) Their nearly circular spot with low divergence makes the fibre-coupling easier, (ii) their epitaxial growth can be done in one process run, (iii) they can be tested without prior cleaving or dicing. All these features lead to a low fabrication cost. However the light emission of VCSELs is vertical to the plane, which can not be easily guided to modulators. Due to the out-of-plane emission, the only way to modulate the light is by using direct modulation. Direct modulation at a wavelength around 1.5 µm has been shown in the 10-15 Gbit/s range, at distances of up to one kilometer [25], but when aiming for a higher modulation frequency up to 40 GHz for WDM, VCSELs may not be a good choice.

The microdisk laser is a very small semiconductor laser that consists of a bulk or quantum well structure formed into a disk, such that total internal reflection of photons travelling around the perimeter of the disk results in high-Q whispering-gallery resonances. Semiconductor lasers in the form of thin disks on pedestals were first successfully demonstrated in the early 1990s as extremely compact sources of light [26]. The main features of such lasers are (i) ultra low thresholds, and (ii) pre-dominantly in-plane light emission. Besides these pros and this compact size, the output power is only in the order of micro watts, which can fulfil neither the need of a WDM head-end station nor the power budget for the beam-forming in the smart antenna system.

DFB and DBR lasers

A DFB laser uses diffraction gratings, which act as distributed reflectors inside the amplifying waveguide of the laser, to create the photonic resonance and oscillation in the cavity. The grating provides feedback of a single wavelength within the active region. By using a power combiner or an AWG, one can create a multi-wavelength laser out of an array of DFB lasers [22]. To extend the typical DFB laser tuning range of 5 nm, multi-section DFB lasers are used, in which several active sections have their own grating that can be temperature-tuned individually, reaching tuning ranges of up to 15 nm [27]. DBR lasers operate in a similar way as DFB lasers, except that the Bragg grating and the gain section are spatially separated. The laser cavity is between two DBR gratings or between one grating and the cleaved facet at the amplifier end. A multi-wavelength laser made with an array of DBR lasers was demonstrated for instance by Ménézo *et al.* [23]. Infinera has realized a DBR transmitter PIC consisting of 40 tunable DBR lasers [28]. Within the DBR-category, there are sampled-grating DBR (SG-DBR) lasers or super structure grating distributed Bragg reflector (SSG-DBR) lasers [29], and digital supermode distributed Bragg reflector (DS-DBR) lasers [30].

AWG-based lasers

In 1994, Zirngibl published the first AWG-based multi-wavelength lasers (AWGL) [31]. This AWGL consists of a series of integrated semiconductor optical amplifiers (SOAs) with an arrayed-waveguide grating (AWG) acting as an intra-cavity filter on a single chip using an active–passive integration technology. In the most straight forward designs, a series of SOAs is connected to the demultiplexed ports of an AWG. At the multiplexed port, either the facet or a DBR can be used as a common reflector for each laser channel. On the demultiplexed port side, there are facets or other reflectors providing the mirror for each laser cavity. In an AWGL designed for multi-wavelength operation, the number of wavelengths is equal to the number of SOAs integrated in the device. In such devices each wavelength is generated from a dedicated SOA, thus simultaneous operation of all wavelengths is possible.

An integrated multi-wavelength laser on InP has been reported as a multiple-channel laser source as well as a digitally tunable laser [32]. The coupling of two AWGL-cavities was reported in [33]. This device can produce 16 wavelengths with 8 SOAs and 2 AWGs. A laser based on serial coupling of two AWGs with different channel spacings was also reported [24]. The highest number of wavelength channels (56) was reported in [34]. This device couples two AWGs in series with the same channel spacing but different free spectral ranges (FSRs).

1.5.2   Optical modulator

Light waves have various characteristics that can be modulated to carry information, including the intensity, phase, frequency and polarisation. Among these, the intensity modulation is the most popular for optical fibre communication systems, primarily due to the simplicity of intensity photodetection.

The intensity of laser light can be modulated either directly, i.e. while being generated, or externally. In direct modulation, the electrical signal that contains the information is directly applied onto the laser by modulating the injection current so that, the output light power is modulated; while for external modulation, the laser emits continuous wave (CW) and a modulator is used to modulate the output. In direct modulation, the laser can suffer from the large shifts in the optical carrier frequency as a result of modulation switching, which is known as *chirp*[1]. Moreover, inside the laser cavity, the internal charge transport and recombination mechanisms limit the laser frequency response, because the laser noise increases significantly above the laser relaxation oscillation frequency [35]. As the modulation frequency increases towards the relaxation resonance frequency of a semiconductor laser, both the relative intensity noise and distortions increase rapidly. This severely limits the feasibility of direct modulation for high-frequency (>20GHz) links [36]. External modulation can reduce these effects but adds system complexity.

Most of the modern wide-bandwidth modulators are based on two types of physical effects: one is the linear electro-optic (EO) effect, also known as the Pockels effect, and the other is the electro-absorption (EA) effect. Both effects depend on the applied electric field, which makes the modulators voltage-controlled devices. Several types of external optical intensity modulators have been developed over the past few decades for optical communication applications. These include Lithium niobate (LiNbO$_3$) Mach-Zehnder modulators, polymer Mach-Zehnder modulators, semiconductor electro-absorption modulators (EAMs) and semiconductor Mach-Zehnder modulators (MZM).

Lithium niobate is the most widely used material for manufacturing different electro-optic modulators due to its large electro-optical coefficient, low optical loss and high optical coupling efficiency with a single mode fibre. Among all types of

---

[1]The intensity modulation is accompanied by an index (thus phase) modulation, which in turn results in a broadening of the optical wavelength. This is so-called wavelength chirp.

MZMs, the LiNbO$_3$ MZM is considered as the device with the best performance, which has broad optical bandwidth, zero or tunable chirp and temperature insensitivity [36]. But its large size, and polarisation sensitivity make it difficult to integrate with other components, and its material makes it unsuitable for single chip integration of lasers. Compared with LiNbO$_3$ and III-V semiconductors, organic polymers are relatively immature as EO materials. Although polymer modulators have the potential of integration capability with various electronic and optoelectronic components, even stacking in vertical direction, the size, thermal and photochemical stabilities are major problems.

Considering the monolithic integration with lasers, the III-V semiconductors-based electro-absorption modulators (EAMs) and Mach-Zehnder modulators (MZMs) should be good choices for our use. Now we will discuss and compare these two types of modulators and summarize the characteristics and performance of reported modulators.

InP based electro-absorption modulators

Electro-absorption modulators are based on the electro-absorption effect, which occurs as a change of material absorption in the presence of an electric field. The EA effect depends on a shift in the absorption band of a semiconductor material in response to an applied electric field. The absoption of the optical signals passing through the EA modulated waveguide varies with the applied electric field, which directly results in an optical intensity modulation. Thus no further optical circuitry is required. In addition, due to the high modulation efficiency, EAMs can be given a compact size, which is attractive for integration. Moreover, the primary material for fabricating EAMs working at 1.3~1.6 μm are currently III-V semiconductors, specifically ternary and quaternary alloys grown on an InP substrate, which are also the materials for fabricating many other active optoelectronic components operating in the same wavelength range, including lasers, SOAs and photodetectors. This also makes EAMs more suitable for integration.

There are two types of electro-absorption effects: the Franz-Keldysh effect (FKE) in bulk materials and Quantum-confined Stark effect (QCSE) in quantum-well (QW) materials. Due to strong exciton resonance, the QCSE-induced absorption change is much larger than that of FKE [36]. The larger absorption change along with the high modulation efficiency attributed to the tight and strong optical and electric field confinement of the quantum well structure, provide EAMs another advantage of low modulation voltage.

The bandwidth limiting factor in such a modulator is the time it takes to charge and discharge the capacitance of the diode through the series resistance of the lumped element (LE) electrodes and the semiconductor layers. This bandwidth limit is given by the reciprocal of the time constant $\tau = RC$. Since the series resistance R is often already minimized, the only way to increase the bandwidth of a lumped EAM

Type	Loss [dB]	V [V]	Ext. [dB] [dB]	$f_{3\,dBe}$ [GHz]	L [µm]	Z [Ω]	Material	Year	Ref.
-	5.2	3	11.5	38	900	-	MQW	2002	[37]
LE†	10.2	1.3	-	0.7	1300	-	MQW	2004	[38]
TW‡	13.5	3.5	10	60	100	30	MQW	2005	[39]
TW	20	1.2	15	60	75	81	MQW	2007	[40]
-	1	1.5	20-30	35-39	125	-	IQW	2007	[41]
-	<10	1.1	10	50	100	50	MQW	2007	[42]
-	13	-	30	60	350	20.4	-	2008	[43]
TW	-	2.1	10	70	210	35	QW	2008	[44]

† LE: *lumped element*
‡ TW: *travelling-wave*

Table 1.1: Overview of InP-based EAMs.

is to decrease its capacitance by shortening the absorption length. To overcome the bandwidth limit imposed by the *RC* time constant, one can use a travelling-wave (TW) configuration. Then, the optical signal is modulated by a microwave signal that is travelling along the electrode. In TW-EAMs, velocity matching of the optical and electrical signals is not as important as in Mach-Zehnder modulators, since the active length is much shorter. Disadvantages of EAMs are large chirp (caused by a refractive index change accompanying the absorption change) and high insertion losses due to the bandgap wavelength of the absorption layer, which is close to the signal wavelength. Also it should be noted that electro-absorption is accompanied by photocurrent generation, which may affect the modulator performance at high optical power, including the optical absorption coefficient and modulation bandwidth. Thus the optical bandwidth and thermal instability are also issues for EAMs. Table 1.1 gives a selected overview of InP-based electro-absorption modulators. It shows that the TW-EAMs have better performance and the TW-EAMs have the potential to reach even higher bandwidths, while increasing the extinction ratio at the same time due to a longer absorption length.

InP based Mach-Zehnder modulators

Different from the EAMs that directly change the intensity of the optical signal, the MZMs realize the intensity modulation by exploiting the electro-optic effect to induce a phase change. In InP-based materials, the EO effect depends on the material crystalline asymmetries to produce a change in the refractive index in response to an applied electric field. A phase modulation is changed into an amplitude modu-

Bias [V]	Loss [dB]	V_π [V]	Ext. [dB]	$f_{3\,dBe}$ [GHz]	L [mm]	Z [Ω]	Year	Ref.
-	-	1.5	>12	-	0.4	-	2004	[46]
7.8	10	2	>10	-	20×0.18	-	2005	[47]
2.8	-	2.6	11.6	45	4	50	2006	[48]
4.2	-	-	-	63	2	50	2006	[48]
7.5	-	<2.5	>16	-	1.5	-	2008	[49]
6	14	1.2	>15	28	1	50	2008	[50]
8.85	2.5	2.1	18	-	3	50	2009	[51]

Table 1.2: Overview of InP-based MZMs.

lation by using constructive or destructive interference effects in an interferometric structure. If both arms of the interferometer are designed as EO waveguides, they can be driven in a push-pull configuration. This push-pull modulation allows different voltage swings at the two arms, but with opposite phases, in which case the phase changes in the two arms are opposite, doubling the overall phase change $\Delta\Phi$. In this way, V_π can be reduced to half of its normal value, and still have the same modulation effect.

III-V compound semiconductors such as InP, GaAs and their alloys exhibit electro-optic effects. The coefficient of the bulk material is about 20 times less than that of LiNbO$_3$, but the optical mode can be confined to a much smaller area, resulting in an increased electric field. In addition the refractive index, around 3.2 for InP, is larger than that of LiNbO$_3$ ($\sim$ 2.2), which also improves the index change [36]. It is possible to strongly enhance this index modulation using the QCSE in a QW structure [45]. So InP-based MQW Mach-Zehnder modulators can therefore provide a similar performance as LiNbO$_3$-based modulators with a much smaller device size.

Table 1.2 gives a selected overview of InP-based Mach-Zehnder Modulators, which are all with quantum well material. The highest bandwidth reported so far (63 GHz), was realized with a modulator with capacitively loaded travelling-wave electrodes, which enabled both a velocity and impedance match. The periodical loading of the phase shifter was originally developed by Walker [52]. The loaded-line design concept is able to combine the high efficiency of vertical p-i-n-type phase modulators with a velocity-matched 50 Ω structure to obtain very high bandwidth/voltage ratios. A 40 Gbit/s modulator was reported with 4.2 V reverse bias and low driving voltage (2.6 V) [48].

After the comparison between the features of these two kinds of modulators, Mach-Zehnder modulators appear to be suitable for our use. First of all, in analog applications, the nonlinearity of a modulator causes distortions and reduces the dynamic

range of a RF link. In an EO MZM, the transfer curve is well known as a sinusoidal function and is relatively independent of the input optical and RF signal powers. On the other hand, an EAM has a nonlinear transfer function that has a strong dependence on input optical wavelength and power, which could limit the dynamic range and the link gain of an RF link and makes linearisation difficult [53]. For digital applications as transmitter in a WDM system, the larger wavelength independence of MZMs is beneficial for WDM systems, while the EAMs have a narrow optical bandwidth. Secondly, for integration with lasers, EAMs may need an extra epitaxial step for their material, because they need a different bandgap than the laser material to have good absorption properties. On the other hand, MZMs can do with bulk material and also waveguides can do with multiple-quantum-well (MQW) material as well. Besides, MZMs offer better power handling than EAMs since less photocurrent is generated in most designs and the optical power is split into two to each arm. One more advantage of MZMs is that they induce much less thermal control problems than EAMs. Moreover, EAMs have relatively high insertion loss, albeit with a shorter device length. MZM devices are fairly long in comparison with EAMs. The length of the modulator is a trade-off between the insertion loss and efficiency of the modulator.

1.5.3   Integrated multi-wavelength transmitter

Regarding the integration of a multi-wavelength laser and modulator, co-packages of DFB laser with GaAs MZM have been commercialized by Bookham-Marconi (subsequently Oclaro, Caswell, UK), and lasers co-packaged with multi-quantum well Mach-Zehnder modulators operating at 10 Gbit/s have been commercialized by Nortel Network (subsequently Oclaro, Canada). This kind of co-packaged devices can reduce footprint and improve operation, and it is indeed cheaper than discrete components, but fully monolithic integration of the laser and modulator on a single chip can offer an even more compact size, and reduce the coupling loss. A monolithically-integrated tunable transmitter has been reported by the University of California, Santa Barbara [54]. This transmitter uses a Sampled-Grating (SG) DBR laser, followed by a push-pull Mach-Zehnder modulator and an SOA for boosting the output power. It realizes an extinction ratio of l0 dB at 40 Gbit/s, with $V_{bias} = 2$ V. Transmitters formed by SG-DBR lasers integrated with EAMs were reported in 2007 [41]. The SG-DBR lasers demonstrated 30 nm of tuning with output powers up to 35 mW. The integrated QW EAM provided 3-dB optical modulation bandwidths in the 35–39 GHz range, low-drive voltage (1.0–1.5 V_{pp}).

However, all above-mentioned publications are single-channel lasers or tunable lasers integrated with modulators. Little has been done on multi-wavelength transmitters. Intel has filed a United States patent of a transmitter-receiver with integrated modulator array and hybrid bonded multi-wavelength laser array in 2007. It describes a single multiple quantum well based InP gain chip that is flip-chip bonded

or wafer bonded across the silicon rib waveguides in the silicon layer of a silicon-on-insulator (SOI) wafer. The Si Mach-Zehnder Interferometer modulators can operate at the speed of 10-40 Gbit/s and beyond [55]. Infinera has reported a 40-channel InP transmitter photonic integrated circuit with EA modulators up to 40 Gbit/s per channel [56].

1.6 Thesis overview

1.6.1 Novel contributions

This thesis focuses on using the concept of filtered-feedback for developing a multi-wavelength transmitter that can be fabricated making use of the building blocks available in InP generic integration platforms. These platforms provide the standard basic elements of InP circuits with low-cost fabrication in a standard process, which will be described extensively in the next chapter. All the circuits presented in this thesis were designed by the author making use of the building blocks offered by the platforms and custom-designed components. The author produced mask designs, characterized the circuits, and developed the circuits. All circuit fabrication was done in multi-project wafer runs of the platforms.

The work starts with the development of a Fabry–Pérot (FP) laser which can be fabricated in a standard InP active-passive integration process, continues with the filtered-feedback multi-wavelength laser, and finishes with the realisation of a combination of the multi-wavelength laser with high-speed modulators, thus creating a multi-wavelength transmitter. After the development and analysis of these specific components, the final transmitter devices are demonstrated and tested in an analog photonic link within the telecom wavelength range. The significant contributions that resulted from this work are listed below:

1. Demonstration and characterisation of FP lasers with integrated multi-mode-interference reflectors (MIRs) [57]. These lasers are among the first integrated photonic devices that were fabricated using an industrial generic integration technology. They are proven to be versatile building blocks for large-scale integrated photonic circuits [58].

2. Demonstration of the world's first filtered-feedback multi-wavelength laser, simultaneously lasing in four channels. A four-channel monolithically integrated filtered-feedback laser has been successfully designed, fabricated in a multi-project wafer run, and characterised. The lasers show accurate channel spacing, high sidemode suppression ratio (>40 dB), low threshold current (<16 mA) [59] and narrow linewidth (<150 kHz) [57].

3. Investigation of the stability of filtered-feedback laser. The stability of the laser has been studied both experimentally and theoretically as a function of the

feedback phase [60].

4. Demonstration of the optical link using the above mentioned transmitter. The bandwidth, crosstalk, and dynamic range of this integrated multi-wavelength transmitter are investigated.

1.6.2   Preview of the thesis

This thesis presents the theory, design, integration, and results of an integrated filtered-feedback multi-wavelength transmitter. This transmitter is realized in three steps, where each next step builds further on the previous one. In step 1, a FP laser with on-chip broadband reflectors is developed. Step 2 extends this laser concept to a filtered-feedback multi-wavelength laser. In the final step 3, the Mach-Zehnder modulators are added to form a single multi-channel transmitter chip. These three steps are described in detail in three consecutive chapters 3 to 5. The thesis is organized as follows:

In Chapter 2, the design theory used for the filtered-feedback multi-wavelength transmitter is outlined. The concept of the AWG, of the AWG-based laser and of the filtered-feedback laser are presented.

Chapter 3 introduces the novel FP laser with multi-mode-interference reflectors. Beside the basic characterisation of the FP laser, the linewidth enhancement factor is measured by external injection locking on this FP laser.

Chapter 4 deals with the characterisation of the filtered-feedback multi-wavelength laser. The circuit performance is validated for simultaneous lasing in four channels. The laser linewidth is measured and the laser stability is investigated. This chapter highlights the world's first filtered-feedback multi-wavelength laser with very narrow linewidth, and an understanding of the laser stability with respect to the feedback.

Chapter 5 presents the results of the integrated multi-wavelength transmitter. First, DC performance of the filtered-feedback laser with Mach-Zehnder modulators is presented and analysed. Next, high-speed and multi-channel optical-link experiments are performed. And lastly, dynamic range and crosstalk results are presented, providing a basis for further expansion and improvements to the current achievements.

Finally, Chapter 6 summarises the dissertation and makes suggestions for future work.

Chapter 2

Theory and fabrication of multi-wavelength transmitter

This chapter starts with a brief explanation of the arrayed waveguide grating (AWG), and follows with a conventional AWG-based multi-wavelength laser design and its transmitter design. Then this chapter continues with the transmitter based on a novel filtered-feedback AWG multi-wavelength laser. The transmitter is realized by using an external Mach-Zehnder modulator, the theory of which is also described. Finally the InP generic integration platform, in which our devices are fabricated, is introduced.

2.1   Arrayed waveguide grating (de)multiplexer

An arrayed waveguide grating (AWG) is an optical multiplexing/demultiplexing device, which is playing a very important role in wavelength division multiplexing (WDM) systems. AWG devices are performing the function of demultiplexing and multiplexing a large number of wavelengths from and to a single optical waveguide or fibre and this function considerably increases the transmission capacity of WDM systems.

AWG devices were first proposed by Smit in 1988 [61]. The first devices working with short wavelengths (776.5 nm-781.2 nm) were reported by Vellekoop and Smit [62, 63]. Through the dispersive effect of an array of waveguides with varying path length, the AWG images the field of an input waveguide onto an output plane, where the position of the image in the output plane is dependent on the wavelength of the light. By proper positioning of output waveguides, the different wavelengths are spatially separated and are each collected by a different waveguide. The design
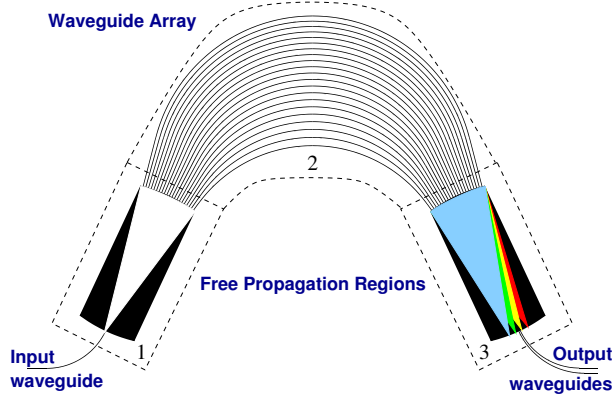
Figure 2.1: Illustration of an AWG (de)multiplexer: (1) input free propagation region (FPR), (2) waveguide array, (3) output free propagation region (FPR).

rules of AWGs have been extensively described in [64]. Here we only briefly explain the operating principle and functionality of an AWG in an integrated circuit.

In the schematic example of Fig. 2.1, the light couples from the input waveguide into the free propagation region (FPR) (1), where the light is no longer laterally confined in the waveguide. Then the diverged light is coupled into an array of waveguides. Because the array waveguides have different lengths, the light in each arm accumulate a different phase change. However, the waveguides are arranged in such a way that that the optical path length difference between adjacent waveguides equals an integer multiple of the central wavelength λ_c of the AWG. Each waveguide in the array (2) increases in length by ΔL compared to the previous one in the array, where $\Delta L = m\lambda_c/n_{eff}$. Here m is called the diffraction order of the array and n_{eff} the effective group index of the waveguide mode [64]. As a result, the light is again in phase when exiting from the array waveguides and the field of the central wavelength is projected at the center of the output focal plane, where an output waveguide is positioned to capture the focused light. Other wavelengths of light will undergo different amounts of phase change, and the phase front will change along the arrayed waveguides, causing the focal point to move along the focal plane at the end of the output FPR (3). By placing the output waveguides at the corresponding positions, the light of different wavelengths can be picked up by the proper output waveguide. An AWG is periodic in wavelength (see Fig. 2.2), and the period is called the free spectral range (FSR). It corresponds to the wavelength spacing between two successive maxima. Each maximum corresponds to a certain diffraction order of the array, e.g. $m-1, m, m+1$.

An AWG provides a compact solution for combining or splitting signals of different wavelengths. In the multi-wavelength lasers that will be described in the following sections, the AWG plays a crucial role because of its wavelength filtering feature.
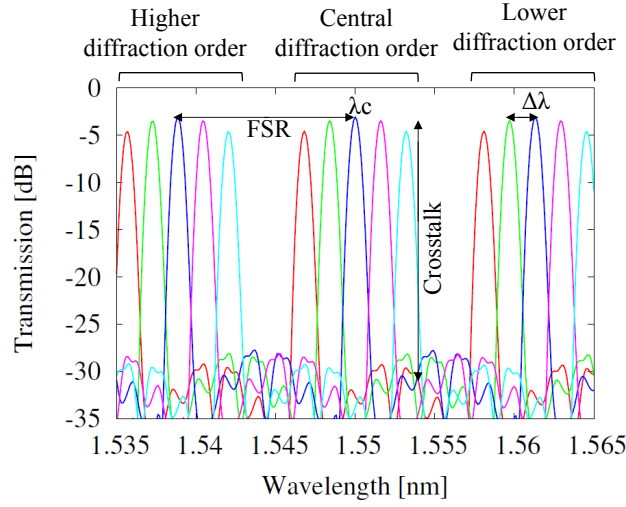
Figure 2.2: This figure shows the superimposed transmission spectra from one input of an AWG to four different output waveguides. The definition of the main properties of an AWG are indicated in the transmission plot.

2.2 Conventional AWG-based multi-wavelength lasers and transmitters

As described in section 1.5.1, multi-wavelength lasers can be realized by combining several semiconductor optical amplifiers (SOA) with an arrayed-waveguide grating (AWG) in a Fabry-Pérot cavity. Using monolithic integration, these components have been fabricated on a single chip using an active/passive integration technology in InP. An early example is given by Zirngibl and Joyner [31]. Such an AWG-based multi-wavelength laser (AWGL) has several advantages over other multi-wavelength and tunable lasers. First, it has the ability to deliver light at the available wavelengths simultaneously and efficiently into the same output waveguide. Second, it has a good long-term wavelength stability due to the fact that the wavelength selection is done by a passive optical element. Third, it has a much simpler wavelength-control mechanism compared to the more conventional multi-section tunable devices that rely on accurate control of tuning currents.

The conventional AWGL configuration consists of an AWG-multiplexer with an array of SOAs connected to its demultiplexed ports and a common output waveguide connected to its multiplexed port [65]. The extended laser cavities are formed between the common output facet and at the individual waveguide facets from the SOAs. Fig. 2.3 shows two different basic schemes of such a laser with four wavelength channels, where the AWG is acting as an intra-cavity wavelength fil-
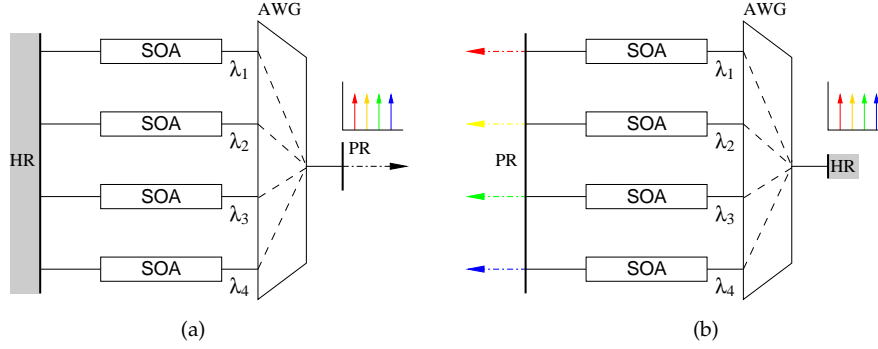
Figure 2.3: Two different basic arrayed-waveguide-grating laser configurations, (a) with multiplexed laser outputs; and (b) with separate laser outputs. Partial and high reflection facets are denoted by PR and HR, respectively.

ter. The cavity loss is only minimal for the specific wavelength corresponding to the maximum transmission of the corresponding AWG passband. In this way, each amplifier has a fixed lasing wavelength, determined by the filter characteristics of the AWG. In practice, one side of the chip is often high-reflective (HR) coated to form good mirrors for the laser cavities, and the other side of the chip is partially reflective (PR) coated to enable the out-coupling of the light. In these devices, depending on whether multiplexed or separate wavelength outputs are needed, the PR coating can either be applied on the common output facet, while HR coating is applied on the individual facet side, see Fig 2.3a, or the other way around, see Fig. 2.3b. Based on these basic AWGL schemes, in combination with integrated optical modulators, various configurations of AWG-based multi-wavelength transmitters can be designed, as described below.

For high-speed modulation, the modulators have to be placed outside the laser cavity, to ensure the stability of the laser and to avoid a large frequency chirp originating in the SOA, due to the modulation of the carrier density which modulates the effective refractive index of the guided mode [66]. Conceptually, it is straightforward to tap a fraction of power from the laser cavity and feed that light into a modulator. This is depicted schematically in Fig. 2.4a, which shows how 1×2 multi-mode-interference (MMI) power splitters are included to tap out half of the light reflected from the individual facets of each laser cavity and that how the light is routed to the respective modulators. Then the different wavelengths of the light can be coupled out from the AR coated side of the chip. Alternatively, the outputs can be multiplexed by a second AWG that has passbands matching the AWG in the laser cavity.

A more elegant solution is shown in Fig. 2.4b, where instead of using a second AWG for multiplexing, the different wavelengths are multiplexed by the same AWG that also provides the intra-cavity filtering. In this single AWG solution, for an *N*-channel
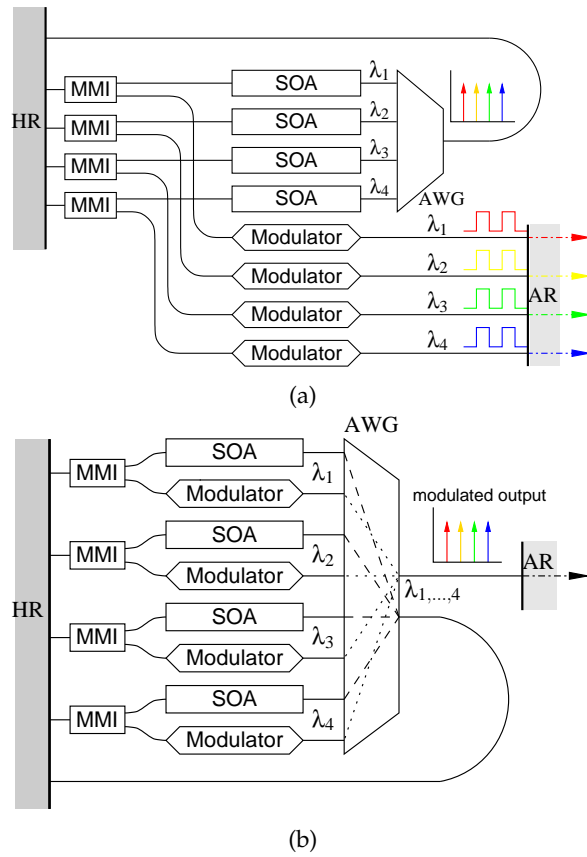
(a)

(b)

Figure 2.4: Configuration layout of (a) cleaved-facet cavity MWL with modulators and with separate modulated outputs; (b) cleaved-facet cavity MWL with modulators and with multiplexed common outputs.
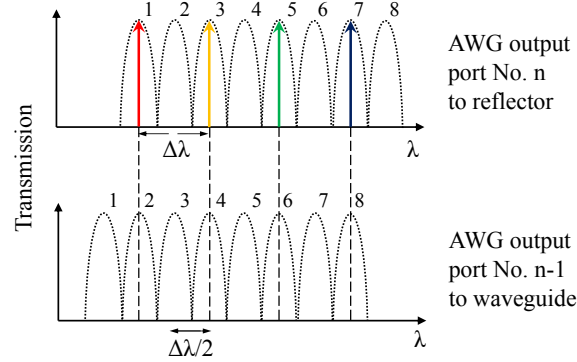
Figure 2.5: Schematic drawing of the transmission spectra of an 8-channel AWG. The passband from 8 input ports of the AWG to output port n and its adjacent port $n - 1$ are superimposed. Each passband corresponds to the input channel which is labeled beside the passband. The passbands shift by $\Delta\lambda/2$ when changing from output port n to output port $n - 1$.

laser with laser channel spacing of $\Delta\lambda$, the AWG needs to have $2 \times N$ channels with a spacing of $\Delta\lambda/2$. An illustration of an 8-channel AWG arrangement to realize four channel wavelength filtering and multiplexing is shown in Fig 2.5. The odd-numbered input ports of the AWG are connected each to a different laser cavity, and the AWG central output port (No. n) is connected to a common reflector for the filtering function to select the laser wavelengths. The even-numbered input port passband towards the adjacent output port (No. $n - 1$) are aligned with the filtering passband. By routing the laser channels back to the even-numbered input ports, these four wavelengths will be multiplexed to output port (No. $n - 1$). This solution performs the filtering and the multiplexing function with alternate ports in a single AWG. A disadvantage of the two-AWG solution, which may suffer from possible channel misalignment caused by fabrication imperfections, is avoided in this single-AWG configuration. However the penalty of the single AWG solution is that a larger-sized AWG is needed with twice the number of channels at half the channel spacing.

2.3 Multi-wavelength lasers integrated with modulators

Conventional AWG-based transmitters can be designed as shown in Fig. 2.4, where the laser cavity is formed by (coated) cleaved facet(s). In this configuration, however, the light is difficult to be kept on the chip, which makes integration with modulators more complex, introducing waveguide crossings (Fig. 2.4a) and extra components,
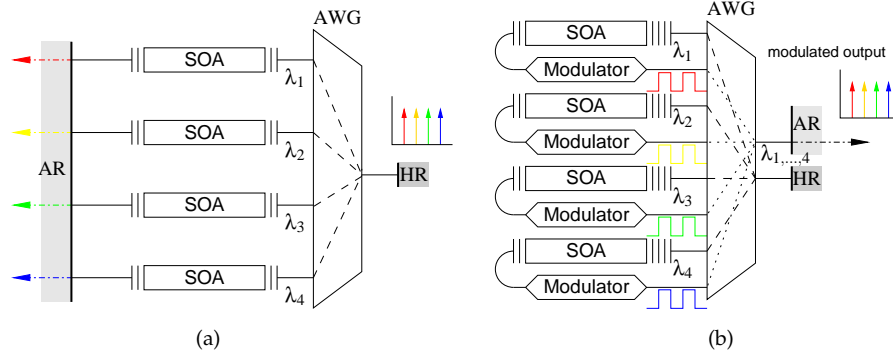
Figure 2.6: Configuration layout of (a) MWL with deeply etched DBR laser cavities; (b) MWL with deeply etched DBR laser cavities integrated with modulators and with multiplexed output.

such as MMI couplers (Fig. 2.4a,b). Moreover, using the AWG as intra-cavity filter has the disadvantage that it needs a long laser cavity extending to both sides of the chip facets, while the AWG inside this long cavity creates unwanted losses and possibly extra reflections.

A promising alternative is to have short Fabry-Pérot lasers that are wavelength stabilized through an AWG filter positioned outside the cavity [67]. Such an integrated laser requires on-chip broadband reflectors that allow the signal to be partly transmitted and partly reflected. Examples of such broadband reflectors are deeply etched DBR mirrors [68], multi-mode-interference reflectors [69] and loop-reflectors [70].

Taking the the deeply etched DBR mirror as an example of the on-chip broadband reflector, Fig. 2.6a shows the schematic of an AWG-based filtered-feedback multi-wavelength laser design. The wavelength selection is now done outside the laser cavity, by the feedback provided from a reflected signal which is filtered by the AWG. The main Fabry-Pérot laser cavity is formed by the SOA and the two deeply etched DBR mirrors located on either side of the SOA. A small fraction of the light is transmitted through the DBR mirror and will be filtered by the AWG and fed back into the laser cavity, thereby locking the laser to the wavelength determined by the feedback (see [67] for a more thorough description of this mechanism). Compared to the conventional AWG based laser configuration, in this short cavity design, the undesired reflections and losses introduced by the AWG are outside the main laser cavity and their influence on the laser performance will be much reduced. Moreover, the laser cavity length can be precisely defined, because the on-chip reflectors can be positioned anywhere on the chip with lithographic precision, while the position of a cleaved facet is difficult to control accurately. The accurate control of the laser cavity length enables tight control over the longitudinal mode spacing of the laser. In addition it allows us to create a short laser cavity with a relatively large longitudinal

mode spacing. This is important to ensure that at most only a few lasing modes fit in the AWG passband which reduces the competition between various modes within the AWG passband and prevents unwanted longitudinal mode hopping.

The utilisation of on-chip broadband reflectors also simplifies the integration of the laser with modulators. The fraction of the light that is transmitted through the reflector on the left hand side can be directly routed to the modulator. In this way the extra loss from the 3-dB splitter in the conventional design can be avoided. This loss is significant, since it consists of a fundamental 3-dB loss in addition to the insertion loss of the splitter. After modulation, the signals can exit separately from an AR coated facet. Alternatively, they can be multiplexed by the same AWG, as is illustrated in Fig. 2.6b and as discussed in the previous section.

2.4   Mach-Zehnder modulator

There are several options for realizing on-chip modulators in InP-based semiconductors. The two main choices for optical intensity modulation are electro-absorption modulators (EAMs), and Mach-Zehnder modulators (MZMs). EAMs have the advantage of small device size, but MZMs employing the electro-optical effects in InP-based materials, have the advantage of larger wavelength independence, high optical-power handling, and zero chirp [36]. We decided to use MZMs in our multi-wavelength transmitter (MWT) designs.

In Mach-Zehnder modulators, the intensity modulation is achieved by phase modulation on one or both of the two waveguide arms by applying an electrical field across the waveguide. The Mach-Zehnder interferometer configuration realizes the conversion from phase modulation to intensity modulation. Fig. 2.7a shows a schematic drawing of the MZM. At the input port, an optical splitter divides a continuous-wave optical input into two equal portions. At the output port, an optical combiner combines the light again. The power splitter and combiner can be a 1×2 coupler, a Y-junction or a 2×2 (directional) coupler.

Consider an MZM with a 1×2 splitter and a 2×1 combiner as an example (Fig. 2.7a). After splitting, half the power propagates in each of the two waveguides which have equal length. These waveguides are referred to here as arm 1 and arm 2. The contributions from each arm interfere constructively in the 2×1 combiner and are guided to the output of the MZM. Each of the MZM arms is provided with an electrode which can be reversely biased to induce an electric field across the optical waveguide. By applying this electrical bias on one of the arms, the refractive index of that waveguide changes, which in turn causes the phase of the light in that arm to change. If the relative phase difference $\Delta\varphi$ between two arms is 0°, the interference is constructive and a maximum intensity output will result. If on the other hand the phase difference $\Delta\varphi$ is ±180°, the interference is destructive and light will be lost from the MZM and the output intensity is minimum. In this scenario, the output in-
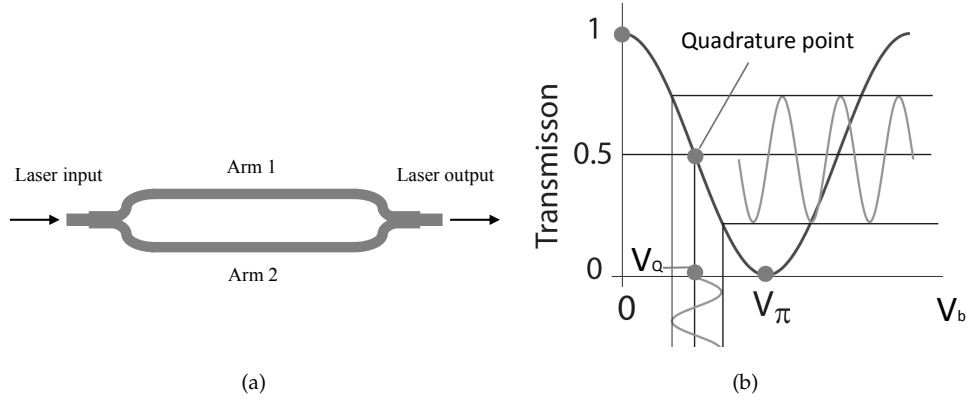
Figure 2.7: (a) Schematic drawing of a Mach-Zehnder modulator; (b) Illustration of electrical/optical conversion in a MZM modulator with linear electro-optic effect.

tensity is therefore controlled by the phase difference between the two arms, caused by a change of optical length of one or both arms.

In Mach-Zehnder modulators that are based on $LiNbO_3$, GaAs, or organic polymers, the change in refractive index is induced though the linear electro-optic (LEO)-effect, also known as Pockels effect [71]. In InP-based semiconductor MZMs, the refractive index change is usually caused by the LEO-effect in bulk material and by a combination of the LEO-effect and electro-absorption effects in multi-quantum well material, due to the quantum-confined Stark effect (QCSE) [72]. In this latter case the relation between the index change and the applied voltage is nonlinear. These two effects will add up or cancel each other depending on the waveguide orientation.

Now we describe the MZM operation principle in a mathematical way. At the output of the MZM, the amplitude of the optical field can be generally represented by the sum of two branches of the light wave:

$$A_{\text{out}} = \frac{\sqrt{2}}{2}(A_1 e^{j\varphi_1} + A_2 e^{j\varphi_2}) \tag{2.1}$$

Where A_1, A_2 and φ_1, φ_2 are the real optical amplitudes and the real phase delay in each arm respectively. So if $\Delta\varphi \equiv \varphi_1 - \varphi_2$ the output optical power is

$$P_{\text{out}} = |A_{\text{out}}|^2 = \frac{1}{2}[A_1^2 + A_2^2 + 2A_1 A_2 \cos\Delta\varphi] \tag{2.2}$$

Dividing P_{out} by the MZM input optical power $P_{\text{in}} = A_1^2 + A_2^2$, the optical intensity transfer function of the MZM can be written as:

$$T_{\text{MZM}} = \frac{1}{2}[1 + b\cos(\Delta\varphi)] \tag{2.3}$$

with $b = 2A_1A_2/P_{in}$. When the input light power is equally split in to two arms, $b = 1$. If one arm of MZM is grounded, $\Delta\varphi$ is a function of the bias voltage V_b on the other arm. To achieve a maximum modulation slope efficiency, the modulator bias should be at the quadrature point ($V_b = V_Q$) of the modulator, At this point $V_b = V_Q$, the electrical to optical conversion has the maximum slope responsivity as shown in Fig 2.7b.

When exploiting the linear electro-optic effect, the bias voltage V_b applied to one arm and the resulting phase difference $\Delta\varphi$ between the arms are related as:

$$\Delta\varphi = \Gamma\frac{2\pi}{\lambda}\Delta n L = \Gamma\frac{2\pi}{\lambda}\left(\frac{1}{2}n_0^3 r_{ij}\frac{V_b}{d}\right)L = \pi\frac{V_b}{V_\pi} \tag{2.4}$$

and

$$V_\pi = \frac{\lambda}{n_0^3 r_{ij}}\cdot\frac{d}{\Gamma L} \tag{2.5}$$

where n_0 is the optical group index of the waveguide at zero waveguide orientation applied voltage; r_{ij} is the relevant EO coefficient[1], determined by the material, optical polarisation and the electrode design; Γ is the confinement factor for the optical field in the externally applied electrical field; d is the distance across which the bias voltage is applied; L is the length over which the bias voltage is applied and V_π is the voltage at which the bias-induced phase difference reaches π.

In the case of linear electro-optic effect, insertion of Eq. 2.4 in Eq. 2.3, yields

$$T_{MZM} = \frac{1}{2}\left[1 + b\cos\pi\frac{V_b}{V_\pi}\right] \tag{2.6}$$

For a MZM using the QCSE-effect, the relation between the bias voltage V_b and phase difference $\Delta\varphi$ is not linear [73]. In addition to a strong index change, the QCSE introduces electro-absorption as well. This can be understood on the basis of the Kramers-Kronig relation. A typical transfer curve for an MZM using the QCSE is shown in Fig. 2.8b. For comparison the typical transfer curve using the EO effect in shown in Fig. 2.8a.

2.5   Fabrication platforms

Above we have discussed on circuit level how to design the filter-feedback multi-wavelength transmitter. In order to transfer the design into a real device, a mature technology is need for fabrication. All the devices described in this thesis, including the lasers with multi-mode interference reflector, the filtered-feedback multi-wavelength laser and filtered-feedback multi-wavelength transmitter are all designed and fabricated on a so-called generic integration platform.

---

[1]r_{ij} depends on orientation of the index ellipsoid of the material and the orientation of the applied electrical field.
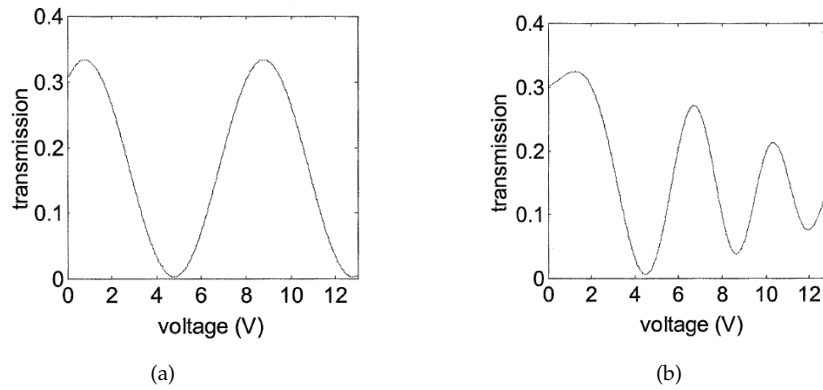
Figure 2.8: Typical transfer function of a Mach-Zehnder modulator, using (a) the linear electro-optic effects and (b) the quantum-confined Stark effect. In reality, the modulator transmission at zero bias may not be at the maximum, due to an initial optical imbalance of two arms (arising from fabrication nonuniformities).

2.5.1 Generic integration platform

Photonic integrated circuits (PICs) are being pursued to keep up with the desire for increasingly high bandwidth and a high degree of functionality. In 2005, the company Infinera introduced the first truly complex PIC in a commercial wavelength division multiplexing (WDM) system: a 10-channel WDM transmitter with more than 50 components integrated on a single InP chip, with a total capacity of 100 Gb/s [74]. But after three decades of research in PICs, still very few of the advanced PICs reported in the literature have been transferred to commercial components or systems. In order to drive the development of PICs faster, the photonic integration group of Eindhoven University of Technology is working on the introduction of a generic integration technology, in which a variety of components and functionalities can be integrated in a single integration process, similar to the established practice in microelectronics [75]. Such a generic approach for realising indium phosphide (InP) PICs is being explored by the Joint European Platform on InP-based Photonic integrated Components and Circuits (JePPIX) [76, 77] through various programmes, such as the Dutch national project MEMPHIS [3], the EU projects EuroPIC [78], and PARADIGM [79]. In this generic photonic integration approach, different photonic circuits with a broad range of functionalities can be constructed from a limited number of basic building blocks, such as optical amplifiers, modulators, detectors, and passive components like waveguides, couplers, filters and (de)multiplexers. Ideally these basic building blocks are provided in the technology design library of a generic photonics foundry, similarly to what is standard practice in the microelectronics sector. With accurate models of these building blocks as well as powerful circuit simulation and layout tools, the designers can create new circuits without the need for a

deep understanding of the physical design for each component/building block used in the circuit. Afterwards, the circuits from different designers using the same generic platform can share the common fabrication process in a wafer-fab, with a much more reliable quality and a higher yield. In this case, the research on basic circuit components and the development of processes for each new circuit application can be avoided, which promises not only a dramatic reduction of the cost for both PIC R&D and manufacturing, but also a reduction of lead time from innovation to final products [80].

All the devices described in this thesis, including the lasers with multi-mode interference reflector, the filtered-feedback multi-wavelength laser and filtered-feedback multi-wavelength transmitter are all designed and fabricated in trial runs of such an InP PIC industrial generic integration process. For each run, the building blocks are described in the platform design manual. The design manual gives the information on the properties of the building blocks and the design rules that restrict the design to fit in the generic run. Based on all the available building blocks, the mask of the circuit is designed. Afterwords, the mask is included in a common mask/reticle set alongside various other designs sharing the same generic process for making a combination of active and passive devices. All circuits are fabricated simultaneously as a multi-project wafer (MPW) fabrication run in the fab of Oclaro (Caswell, UK).

In the following thesis, the three circuits/devices, FP laser with MIRs, filtered-feedback multi-wavelength laser and filtered-feedback multi-wavelength transmitter are fabricated in three of such MPW runs. The FP laser with MIRs and the circuit of multi-wavelength laser use the building blocks of waveguide, waveguide components, gain section and deep-shallow transition. The multi-wavelength transmitter circuit uses one additional building block, the phase modulator. In the next section the building blocks used in the design will be introduced briefly.

2.5.2   Building blocks

In this integration platform, the substrates used are 3" n-doped InP, which is thinned to a thickness of 135 μm. The waveguide structure is based on the InGaAsP alloy system, and the higher-index quaternary layer is sandwiched between InP cladding layers.

Passive waveguide and waveguide components

The standard passive waveguide is a deep-etched waveguide. The waveguide is formed by etching parallel trenches on either side, leaving the majority of the wafer area un-etched. The deep etched waveguides with typical width of 1.5 μm have high lateral mode confinement, allowing bend radii down to 100 μm. The core region is a multi-quantum well (MQW) structure providing enhanced electro-optic (EO) phase
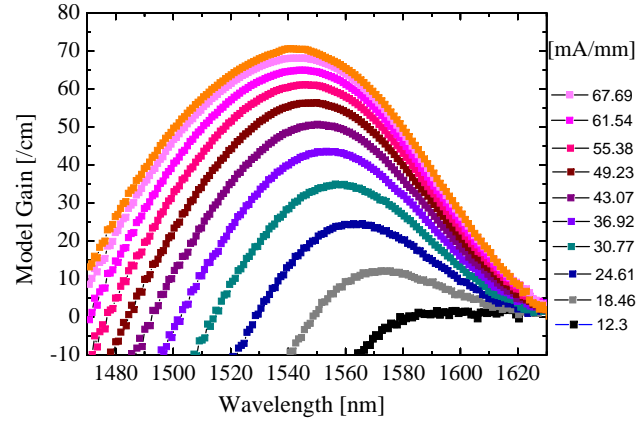
Figure 2.9: The gain information provided by the platform for the gain building block. These spectra are derived from Hakki-Paoli gain measurements on a 325 µm Fabry–Pérot (FP) test structure with different injection currents. The legend is the injection current density in mA/mm.

tuning through the quantum-confined Stark effect (QCSE). The typical waveguide propagation loss is ~3 dB/cm.

Based on the waveguide structure, tapers, AWGs, multi-mode-interference couplers and multi-mode-interference reflectors can be freely designed and used in the circuit design.

Gain section

Building block gain section comes as a single-moded, shallowly etched waveguide structure with gain material, as well as a standard bond-pad on top of the waveguide. The waveguide contains a multi-quantum well gain section. This structure is optimised to provide optical gain for TE polarisation. So the laser light that is generated using this gain section is considered to be TE polarisation.

Although the details of the gain building block are hidden, the gain information is provided from the Oclaro process manual (unpublished) as a typical set of modal gain curves versus wavelength and drive current (Fig 2.9). These are derived from Hakki-Paoli gain measurements on a 325 µm Fabry-Perot (FP) test structure. According to this gain information, the proper length of the section can be chosen for the use in the laser or amplifier in the integrated circuit design.
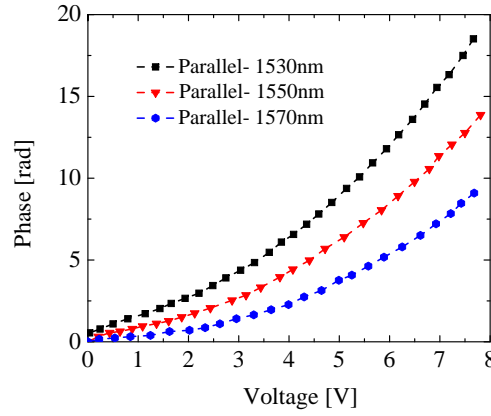
Figure 2.10: The extracted TE mode phase tuning versus the reverse bias of the for a 1 mm long phase shifter which is orientated parallel to the wafer's major flat. The data are from Oclaro process manual (unpublished).

Deep-shallow/shallow-deep transition

In a passive-active integration we use the deeply etched passive waveguide and a gain section with a shallowly etched waveguide. Transition elements between these two types of waveguide are also provided as a building block. This transition building block has a standard length of $100 \, \mu m$ and the optical loss of this element is around 1~1.5 dB.

Electro-optic phase modulator

As mentioned in the passive waveguide section, the core of the strong passive waveguide is an InGaAsP alloy with different MQWs compared to the gain section. The MQW structure can provide efficient EO modulation through the QCSE effect. On the waveguide, where EO phase shifters are required, the InGaAs p-contact layer is left in place and p-metal electrodes are deposited on top.

The performance of the electro-optic phase modulator is significantly more efficient for the orientation parallel to the major flat compared to the perpendicular direction, and therefore it is recommended to lay out this element parallel to the major flat. Typical phase results of the TE mode in a 1 mm long device are shown in Fig 2.10. The electrode and bond-pad designs are included in building block. The length of 1 mm is recommended to achieve an efficient and high frequency (~10 GHz) modulation. In the following chapter, the 1 mm phase shifter is used in the arms of the Mach-Zehnder modulator.

Facet

The optical facets will be parallel to the major flat. There are standard multi-layer coatings available from the platform for interfacing to air: anti-reflection (<0.2%) and high reflection (95%). In order to have ultra-low reflection, the optical waveguide is curved before the output to give an output facet angle of 7°, for further suppressing the reflection from the facet into the fundamental mode.

2.6   Conclusion

In this chapter we discussed the designs of a number of AWG-based lasers. Various configurations can be constructed using three main components: (i) passive waveguides and one or more AWGs, (ii) SOAs, and (iii) reflectors, either a cleaved facet reflector for the conventional AWG-based lasers or on-chip broadband reflectors for filtered-feedback AWG lasers. Filtered-feedback AWG lasers show the advantage on easy integration and simplified structures. We decided to use the filtered-feedback version for realising the multi-wavelength transmitter. For the modulators in the transmitter, the MZ modulator has been chosen. The operation concept of a MZM was explained in detail. Furthermore, fabrication of the devices is explained. All the devices discussed in this thesis are designed and fabricated on a generic integration platform. All the building blocks used in our devices have been introduced.

Chapter 3

Fabry-Pérot lasers with multi-mode-interference reflectors

In this chapter, the multi-mode-interference reflector-based Fabry-Pérot (FP) laser is described, which is the main building block of our filtered-feedback multi-wavelength laser. The chapter begins by introducing the multi-mode-interference reflector (MIR), followed by the design of the MIR-based FP laser device and its test device. Then, the basic laser characterisation will be shown with the study of the MIR reflection and active waveguide properties. Finally an external injection locking measurement is carried out on this MIR-based FP laser, where the linewidth enhancement factor is estimated.

3.1   Multi-mode interference reflector (MIR)

Fabry-Pérot (FP) lasers are formed by a gain medium in the centre and two mirrors on either side, which form the FP cavity. Because the mirrors have no significant wavelength selectivity, the FP laser generates a broad spectrum of multiple longitudinal lasing modes within the wavelength range of the gain curve. The conventional way to make a FP laser in semiconductor material is to utilize the semiconductor-air interface of the cleaved facets of the chip as mirrors to form the laser resonator cavity. Although such FP lasers are easy to fabricate, there are a number of drawbacks, especially when the lasers are used as part of an integrated circuit. The laser cavity has to extend to the edge of the chip, which limits the design freedom of the laser and the integrated circuit geometry. Moreover, because the facets can be cleaved only with limited accuracy (~2 μm at best), the laser cavity length and hence the longitudinal
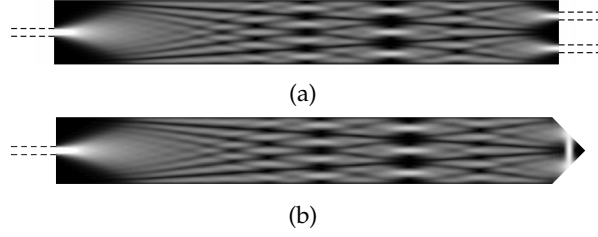
Figure 3.1: Intensity distributions in (a) the original 1×2 MMI coupler and (b) the 1-port MIR after introducing a 90° corner mirror.

mode spacing is not well controlled. Most importantly, since the laser light is emitted from the facets out of the chip, no light is available on-chip for use in other parts of the integrated circuit.

To keep the laser output light on the chip for further use in the integrated circuit, integrated reflectors are preferred. To this end, various on-chip broadband reflectors have been reported, such as deeply etched DBR mirrors [67, 81] and loop mirrors [82, 83]. These on-chip reflectors not only keep the light available for further processing or routing to other sub-circuits, they can also be positioned anywhere on the chip with lithographic precision, thus making it possible to choose a specific cavity length for a desired FP mode spacing. The deeply etched DBR mirrors are strong gratings which have a small number of grating periods and small dimensions (~10 μm^2), but involve non-standard etching steps for fabrication of the high-aspect-ratio structures, which complicates the processing. The loop mirror is easy to fabricate in a normal waveguide process, but unfortunately the required 360 degree turn implies a rather large footprint (~100×100 μm^2 in high-contrast InP waveguides).

To avoid the complexity of the fabrication and keep the footprint small, a novel multi-mode-interference reflector (MIR) is investigated. These MIRs are based upon total internal reflection (TIR) mirrors that can achieve in principle 100% reflection, without the need for a dedicated high-reflection coating. These reflectors are fabricated along with the deeply-etched waveguide structure in any integration process flow which fabricates deeply-etched waveguides and need no extra process steps. The reflectors have relatively small size, and are therefore very promising reflection building blocks for large-scale photonic integration.

A 1-port MIR was originally introduced in [84]. The device is based on a 1×2 multi-mode-interference (MMI) coupler (see Fig. 3.1a), where the output ports are replaced by two deeply etched 45° mirror facets as indicated in Fig. 3.1b. First the light enters in the central input port and after propagation, two images are formed, which will be totally internally reflected by the two etched mirrors, as in a retro-reflector, and the reflected light is imaged back onto the input port of the MMI coupler. In this way, ideally, all the incoming light would be reflected back into the input port, thus creating a 100% reflector.
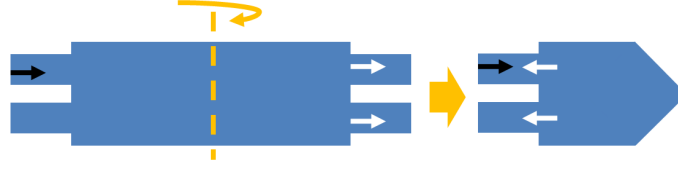
Figure 3.2: Schematic drawing of the realisation of a 2-port MIR reflector.

Similarly, a 2-port MIR device with a 50%-50% reflection/transmission is obtained by "folding back" of a symmetric 2×2 MMI coupler, see Fig. 3.2. The light comes in from one port, and the reflected light is split equally into both ports, which means that the 2-port MIR has equal reflection and transmission. The port where the light carries a bidirectional signal is identified as the reflection port and the other one with only light going out is used as transmission port. By tapering the width of a 2-port-MMI-reflector, the reflection and transmission of the reflector can be tuned to other ratios rather than an equal split [85]. Throughout this thesis only the 50%-50% 2-port MIR devices are used in all FP lasers.

To obtain good performance of the total internal reflection mirrors, the MIR has to be deeply etched with vertical sidewalls. Fig. 3.3a presents a schematic drawing (left) and a scanning electron microscope (SEM) photograph of a high-contrast (deeply-etched) passive waveguide used in the Oclaro platform, which is formed by deep etching through the waveguiding layer. The SEM picture demonstrates a near-vertical side wall ($< 3°$ off-vertical), which shows that with a deep etching step the etched mirrors at the end of the MMI coupler can be obtained [84].

Based on the layer stack of this waveguide building block on the Oclaro platform, the geometry of the MIR can be determined according to the theory and the mechanisms explained by Soldano and Pennings [86]. Fig. 3.3b is a schematic and a SEM picture showing the top view of a 2-port MIR that we used in the FP laser, with a dimension of $9\,\mu m \times 57\,\mu m$. In general, the width of MIR reflectors is chosen by considering the size and fabrication limitations, for example, the wider the width, the lower the device loss, but longer the device, and the minimum lithographical gap width also determines the minimum width of the MMI reflector. For the MIR devices described in this thesis, the width of each MIR has been chosen to be $9\,\mu m$ [85]. Then the beam propagation method (BPM) and the finite-difference time-domain (FDTD) method [87] have been employed to optimize the input waveguide width, position and the length of MMI reflector for minimized loss. Fig. 3.4a shows that at a wavelength of $\lambda = 1550\,nm$, with a waveguide width of $2\,\mu m$ and a multi-mode section width of $9\,\mu m$, the optimum length is $57\,\mu m$ for the TE mode, while the reflection and transmission is not completely symmetric with 5% deviation. Fig. 3.4b is the simulation result for the sensitivity to wavelength in a range from $1.53\,\mu m$ to $1.58\,\mu m$, which confirms that the MIR is broadband, showing less than $0.5\,dB$ variation within

(a)

(b)
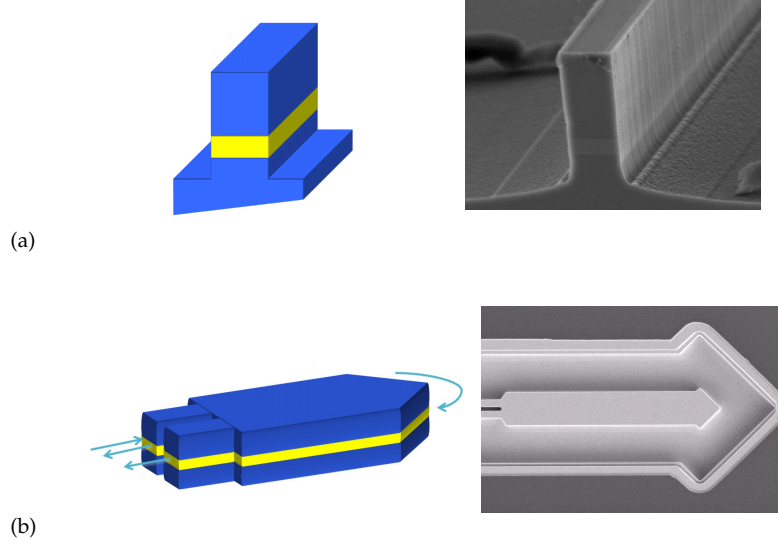
Figure 3.3: (a) 3D schematic drawing of a high-contrast/deeply-etched passive waveguide, with a SEM picture showing its cross section. The waveguiding layer, shown in light colour, is sandwiched between the cladding and the substrate; (b) 3D schematic drawing of a 2-port MIR, and the corresponding SEM picture. To obtain highly reflective mirrors the device has to be deeply etched with vertical sidewalls. The 2-port MIR reflector measures $9 \times 57\,\mu m^2$, inside the etched trench.

(a)   (b)
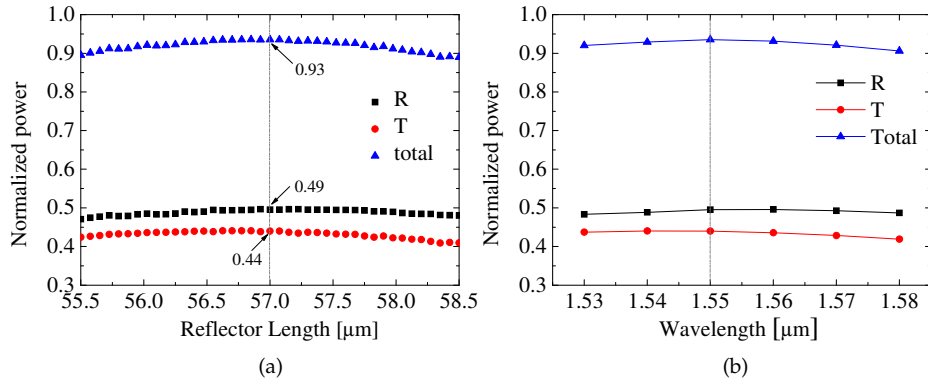
Figure 3.4: Simulation of transmission and reflection for TE mode of the 2-port MIR as a function of (a) device length, at 1550 nm central wavelength; (b) wavelength, with device length of 57 μm. The width of the input waveguide is 2 μm and the width of multi-mode section is 9 μm.

Figure 3.5: Microscope photograph of the Fabry-Pérot laser with MIR reflectors and its corresponding mask layout. Each part of the device is labeled in the figure. The right side waveguide is also routed to an angled facet (not shown). A zoom-in of the part in the dashed line is shown in Fig. 3.6.

this range. Simulation shows that the loss of the MIR is 0.3 dB even when it contains two perfect 45° mirrors. Modal reflection simul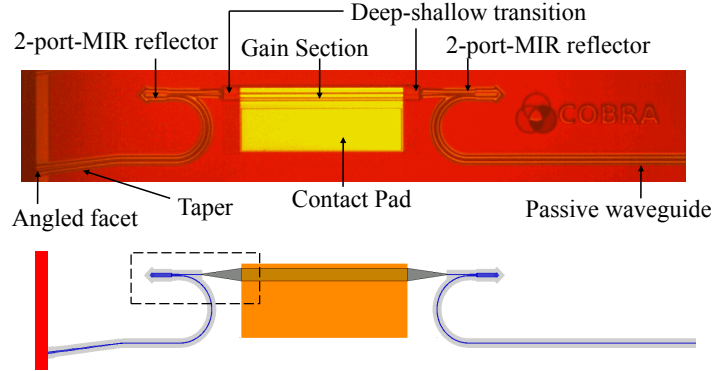ations in [84] show that two deeply etched 45º mirrors with perfectly smooth and vertical sidewalls could induce a loss of 0.5 dB. So in total, from simulations, the 2-port MIR is expected to have loss of around 0.8 dB.

3.2   Design of MIR-based FP laser

After having obtained the optimized design of the 50-50% 2-port MIR, these MIRs have been included as reflective mirrors in the FP lasers. An optical microscopic image of the fabricated MIR-based FP laser is illustrated in Fig. 3.5. The device consists of a centre gain section with a shallowly etched active waveguide, deeply etched passive waveguides, deep-shallow transitions and MIR reflectors. The reflection ports of both MIRs are connected to the gain section through a deep-shallow transition element, thus forming an extended-cavity FP laser. The laser output light is tapped out of the cavity from both sides through the transmission ports of the MIR, and is routed by curved waveguides. To characterize the lasers, the outputs are directly guided to the chip facets at a 7º angle, for minimizing the facet back reflection [88].

Fig. 3.6a presents a zoom-in mask layout on the laser part where the MIR connects to the gain section. To taper the 2 µm MIR port to the standard 1.5 µm wide standard deeply etched waveguide, a 20 µm long parabolic taper is used. To avoid overlap of the trench of the curved waveguide with the deep-shallow transition region, a 55 µm passive waveguide extends the taper and connects to the deep-side of the

deep-shallow transition. The full cavity physical length is the sum of the length

(a)

(b)
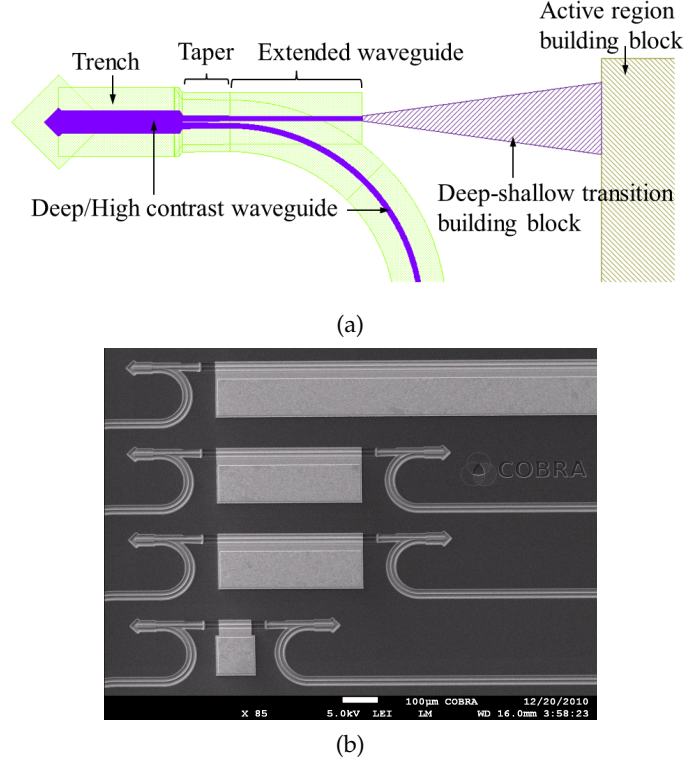
Figure 3.6: (a) Mask layout of the MIR with gain section connection; (b) Lasers based on MIR with active section lengths of 1270 µm (not shown completely), 420 µm (2×) and 100 µm. The 100 µm laser is not used in the rest of the analysis.

of two MIRs with tapers, extended waveguides, two deep-shallow transitions and the gain section. Thanks to the lithographic accuracy of the MIR positioning, the cavity length can be precisely defined, such that, in turn the FP mode spacing can be designed more accurately than with cleaved facet mirrors. The FP mode spacing is $\Delta f = c/(2 \times L_{\mathrm{ocav}})$. L_{ocav} is the optical length of the cavity $L_{\mathrm{ocav}} = 2 \times L_{\mathrm{d}} \times N_{\mathrm{g,d}} + (L_{\mathrm{s}} + 2 \times L_{\mathrm{ds}}) \times N_{\mathrm{g,s}}$, where L_{d} is the length of the deeply etched structures of the laser, including the length of the reflector, taper and the extended waveguide shown in Fig. 3.6a; L_{ds} is the length the deep-shallow transition with fixed design values; L_{s} is the length of shallowly etched waveguide in gain section; and $N_{\mathrm{g,d}} \simeq 3.69$, $N_{\mathrm{g,s}} \simeq 3.55$ are the group indices of the deeply and shallowly etched waveguides. The values were obtained from 2D mode-solver simulations using input from the

Figure 3.7: Schematic MIR based laser, Device A (top), and its corresponding facet test laser Device B (bottom).

design manual[1].

For the first run of this novel device on a new technology platform we designed two sets of test devices:

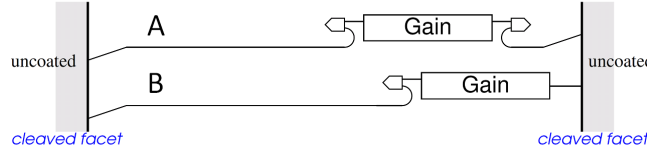**Type A** three MIR based FP lasers with the same passive part and different gain section length as shown in Fig. 3.6b; by comparing the measured FP mode spacing, the effective group index for the deeply etched and and shallowly etched part $N_{g,d}$ and $N_{g,s}$ can be calculated. Gain section length values of 100 µm, 420 µm and 1270 µm are chosen in order to have an approximate FP longitudinal mode spacing of 100 GHz, 50 GHz and 25 GHz, respectively.

Type B the FP lasers have the same gain section length as device type A, but with the cavity formed by a MIR on one side and the cleaved facet on the other side. The facet is designed 125 µm away from the deep-shallow transition (±10 µm depending on the cleaving position), which is close to the physical length of the passive waveguide between the amplifier and the end of the right MIR in device A, in order to make device type B have a similar cavity length. In this condition, by comparing the laser threshold current with the corresponding device type A, the reflection factor of the MIR can be estimated. The calculation is based on the threshold current model [89]

$$I_{th} \simeq \frac{qVBN_{tr}^2}{\eta_i} e^{(\langle \alpha_i \rangle + \alpha_m)/\Gamma g_0} \tag{3.1}$$

where $\langle \alpha_i \rangle$ is the net internal optical loss (in units of m^{-1}), Γg_0 is the transparency modal gain, η_i is the internal quantum efficiency, N_{tr} is the transparency carrier density, V is the volume of the active region, B is the bi-molecular recombination coefficient, for most III-V materials of interest, $B \sim 10^{10}$, q is the electron charge. For the devices of type A and B with same length of the gain section, all the parameters can be expected to be identical, due to the high uniformity resulting from the platform process on 3-inch wafers, except for the mirror loss $\alpha_m = \frac{1}{L} \ln(\frac{1}{r_1 r_2})$. In the mirror loss, r_1 and r_2 are mirror reflectivities from two sides, for which the type A and B lasers are different. Thus by

---

[1]The Oclaro design manual, distributed within the EuroPIC consortium, confidential document.
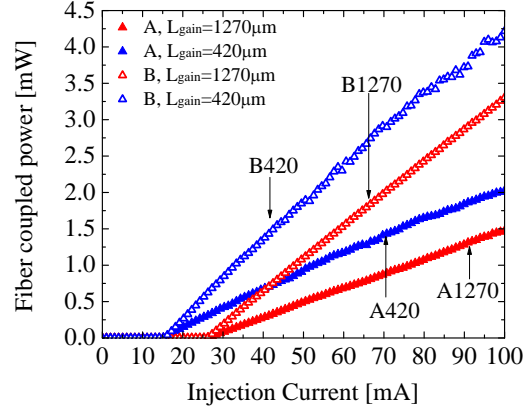
Figure 3.8: The light-current characteristic of MIR reflector based lasers, device A and device B with gain section length of 1270 μm and 420 μm, respectively.

comparing the threshold from laser type A and B, the reflectivity of the MIR can be estimated. Furthermore, the MIR transmission coefficient can also be deduced by comparing the slope efficiency from the light-current characterisation of type A and B devices, which will be shown in the next section.

3.3   FP laser basic characterisation

The fabricated devices are available on several chips. Some of the chips have the facets provided with an anti-reflection (AR) coating and some of the chips are without coating. AR coated type A lasers and uncoated type B lasers are used in the following characterisation. The AR coating on type A is to make sure the reflection to the laser cavity is only provided by the MIRs, rather than by the facets; the uncoated facet on type B is to provide a known 32% facet reflection to form one side of the laser cavity as a reference. The reflection coefficient value was calculated by considering the two-dimensional beam profile [88].

Fig. 3.8 gives the laser light-current characteristic of the lasers of type A and B with different cavity lengths, where the devices are denoted by the name formed by its type with the length of gain section. The traces with solid triangle symbols show that for type A with lengths of 420 μm and 1270 μm gain section, the threshold currents are 15 mA and 26 mA, respectively. An optical output of 2 mW in the fibre can be reached with 100 mA injection current without a significant thermal roll-over. The light is coupled from the deeply etched waveguide to a lensed fibre, where the coupling loss is ~5 dB.
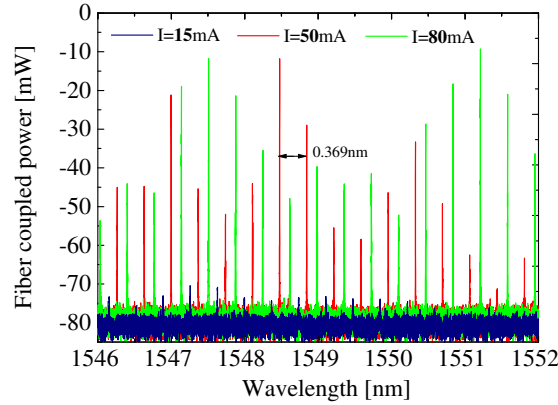
Figure 3.9: The optical spectrum of device A420, type A laser with 420-µm-long gain section, at an injection current of 15 mA (threshold), 50 mA and 80 mA.

The *L-I* curves of the corresponding devices of type B are plotted with open symbols, and the type B lasers have the same threshold current as their type A counterparts. However, the type B devices have a relatively higher slope efficiency than the type A devices by a factor of 2.1±0.1 for both devices of 420 µm and 1270 µm gain sections. With the same length of the gain section and similar cavity length, the lasers of type A and type B have the same modal gain and internal loss. According to Eq. 3.1 an identical threshold current indicates that the MIR has a similar reflectivity as the cleaved facet, which is calculated to be 32%. Due to the same internal properties of lasers type A and B, under the same injection current they should generate the same amount of power inside the laser under the same injection current, while the slope efficiencies of A and B type *L-I* curve differ by a factor of 2.1. The difference is caused by the different out-coupling mirrors, the cleaved facet for type B and the MIR for type A. The cleaved facet has a transmission of ~68%, so the power transmission of the MIR is expected to be close to 68%/2.1 = 32.4%. Compared with the reflection and transmission ratio 50%-50% that we designed for this 2-port MIR, there is approximately $(32\% + 32\%)/100\% = 1.9\,\mathrm{dB}$ loss, of which 0.8 dB is predicted from the simulation and the other 1.1 dB deviation could come from imperfections in the fabrication, e.g. the etched mirror surface quality or the verticality of sidewall, or a possible deviation from the optimum width of the MMI. The estimation of MIR reflection and transmission values shows a good agreement with the measurement results from the purely passive MIR characterisation in [85].

Table 3.1 lists the threshold current, threshold lasing wavelength and the FP mode spacing at 50 mA injection current for the two types A and B with the gain section lengths of 420 µm and 1270 µm. The spectra of type A420 measured by a high resol-

Device	I_{th}	λ_{th}	Mode spacing[†]
A1270	26 mA	1557.39 nm	23.87 GHz
B1270	26 mA	1557.09 nm	23.89 GHz
A420	15 mA	1549.10 nm	46.19 GHz
B420	15 mA	1548.40 nm	46.22 GHz

Table 3.1: The threshold current, threshold lasing wavelength and mode spacing of different FP lasers under test. [†]The mode spacing is measured at 50 mA current injection.

ution spectrum analyser [2] are plotted in Fig. 3.9 for three different injection currents, 15 mA (threshold), 50 mA and 80 mA, respectively. Based on the mode spacing of the laser with various gain section length, the group index of the active waveguide is calculated to be around 3.56, and the average group index of the passive waveguide part is 3.73, including the MIR, taper, extended waveguide and deep-shallow transition. The values are quite close to the platform data. They are used to design the 50 GHz FP laser for the multi-wavelength transmitter device which will be explained in the following chapters. As the MIR and taper are wider than the standard passive waveguide, the average group index of the passive part of the laser is lower than the group index of the passive waveguide given by the design manual.

The set of recorded spectra of device A420 is plotted in Fig. 3.10 as a contour map with the colour brightness indicating the intensity of the modes, where the laser injection current varies from 0 mA to 120 mA with steps of 1 mA, and the resolution bandwidth of the optical spectrum analyser is 0.06 nm. The map of Fig. 3.10, it shows that the FP laser starts lasing at injection current of 15 mA at a wavelength of 1542 nm. When the injection current increases, the FP laser lasing frequencies redshift by approximately 0.6 GHz/mA. At certain injection currents, the lasing mode hops to other frequencies, and then multiple lasing-peaks appear. In most of the cases the main lasing-peaks have a spacing which is several times larger than the FP longitudinal mode spacing, indicating that there are additional intra-cavity reflections in the laser resonator.

The sub-threshold spectrum of device A420 has been measured to inspect the reflections inside the laser cavity using the method described in [90]. In this method sub-threshold spectra of laser are analysed. With intracavity reflections, these spectra will show a series of resonances at a regular spacing. The intra-cavity reflections generate a number of modulations of the intensity of the resonance peaks. The frequency of a modulation is inversely proportional to the distance between the reflection points. The Fourier-transform for this sub-threshold spectrum in shown in Fig. 3.11a, where the time axis has been translated into the physical distance. The

---

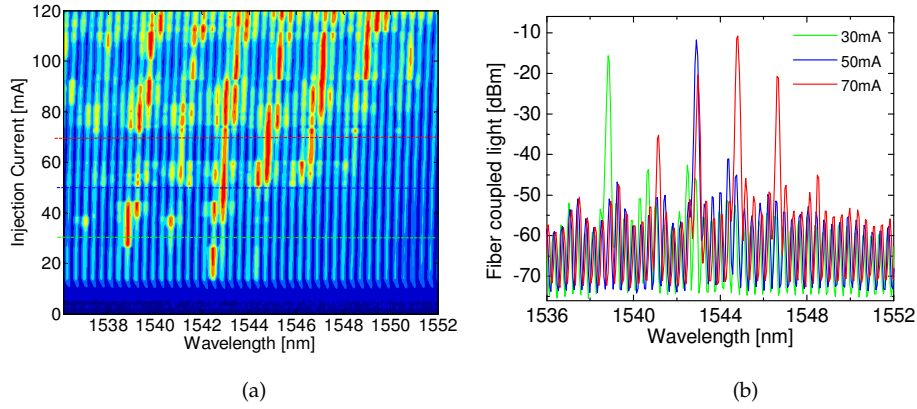[2]APEX AP2041B with 0.16 pm resolution (20 MHz @ 1550 nm)

Figure 3.10: (a) Mapping of laser A420 resonant mode intensity as a function of injection current and wavelength; the colour brightness indicates the power intensity. Three horizontal dashed lines indicate the currents at which the spectra in the right figure are taken. (b) Laser spectra at the injection current of 30 mA, 50 mA and 70 mA.

highest peaks correspond to the main cavity reflections formed by MIRs (at $0\,\mu m$ and $890\,\mu m$). Other peaks are due to spurious reflections inside the main cavity. Clearly visible are the two small reflection peaks at L1 and L2 which correspond to the locations of the shallow-deep transitions, indicating that these are responsible for the spurious reflections.

3.4 External injection measurement

The linewidth enhancement factor α is known to have an important impact on semiconductor laser frequency stability. In semiconductor lasers the intensity-phase coupling is intimately connected to the active gain medium, and its underlying cause is that the real (dispersive) part of the effective index n' of a laser mode is perturbed by a change in the imaginary (absorptive) part n''. The usual measure of the intensity-phase coupling is the linewidth enhancement factor α, which is normally defined as the quotient between changes in n' and n'' with changes in carrier density [91]. To measure the linewidth enhancement factor, several methods have been reported, such as interferometric measurement [92], RF-modulation measurement [93], amplified spontaneous emission (ASE) method [94] and injection-locking method [95].

Here the method of injection-locking on this MIR based FP laser will be used to determine the linewidth enhancement factor of the laser building block under real
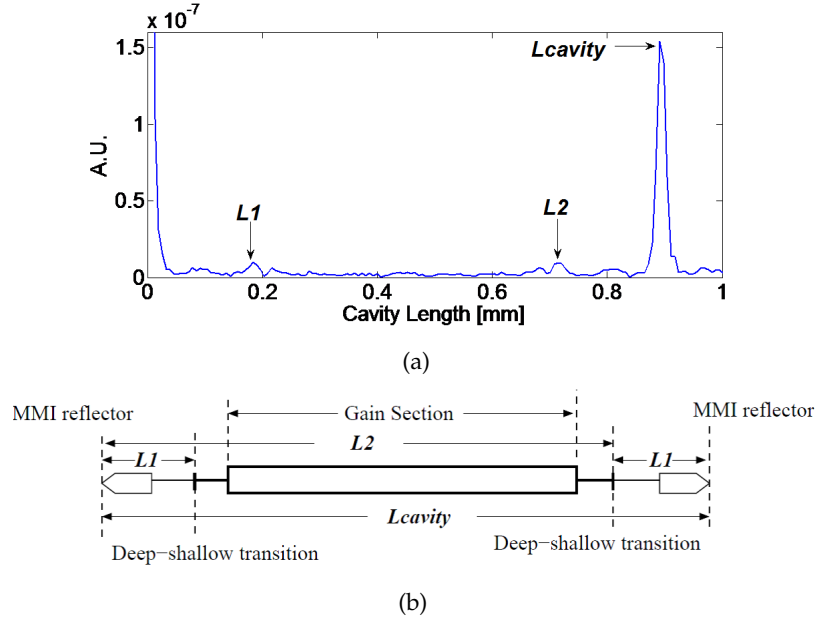
(a)

(b)

Figure 3.11: (a) Fourier transform of a 50 nm span sub-threshold laser spectrum for the laser with a 420 μm-long gain section at 14mA injection current; (b) is a schematic drawing of the possible resonator cavities in this laser.

operating conditions. In addition, with the external injection-locking measurement, the injection power that would be required to lock the laser mode is also investigated, in order to obtain an estimate for the power level of the feedback light needed the further design of the filtered-feedback multi-wavelength laser. It is well-noted that the feedback is not the same mechanism as injection. Instead it is rather a self-injection [96], with the injection laser of the same wavelength, and strongly phase correlated. We will see in chapter 4 that the feedback needs much less power than the injection to achieve a single mode lasing.

As mentioned chapter 2, the MIR-based FP laser will be used as a building block in a filtered-feedback multi-wavelength laser circuit. Here we use the external injection-locking measurement on FP laser A420 in order to get a hint of how much feedback power is required in the filtered-feedback multi-wavelength laser, and also to obtain a measurement of linewidth enhancement factor of the laser.

The process of optical injection is carried out as follows: light from a single-frequency master light source, generally a tunable laser, is injected into the slave FP laser diode. The master laser light is going one way into the slave laser, and there is no back reflection from the slave laser to master laser. When the injected light from the master laser is strong enough, it is amplified by the available gain in the slave FP laser. At
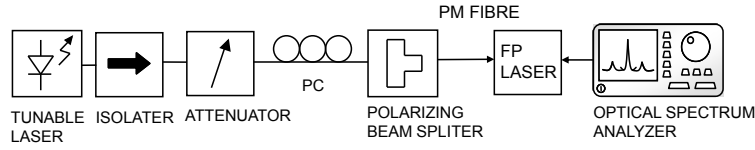
Figure 3.12: Injection locking measurement setup. The FP laser used in the test is laser A420. See the text for other details.

the same time the gain of other longitudinal modes in the slave FP laser is saturated, and these modes are suppressed. Then in the slave laser there is only single-mode lasing, which is on the frequency of the injected light from the master laser. At this point the FP laser is locked to the master laser frequency. Once a locking state is reached, all the power of the FP laser is at the frequency of the master laser.

In the following, we are going to study the injection locking measurement on the MIR-based FP laser A420, with a tunable laser (Agilent 86100B) as the master laser. The setup of the measurement is shown in Fig. 3.12. An optical spectrum analyser (APEX) is used to measure the optical spectra of the test laser and the master laser. The tunable master laser and laser A420 were both temperature stabilised during the measurements. The tunable laser was set to a certain output power, and was attenuated by a variable optical attenuator. After the attenuator, the light was connected to a polarising beam splitter (PBS) though a polarisation controller (PC). The PC tunes the TE-polarized output from the PBS to the maximum, and the TE light is injected into the FP laser via a polarisation-maintaining (PM) fibre. On the other side of the chip, a lensed fibre is aligned to the output facet of the FP laser to couple out the output light, and the light is sent to an optical spectrum analyser (OSA) for spectral analysis of the emission.

When operating without external injection, laser A420 has a longitudinal mode spacing of ~46.5 GHz (~0.368 nm @ 1550 nm). It has a multi-mode lasing spectrum, with some favoured modes due to the spurious reflections inside the cavity (see Fig. 3.13a). The threshold current is 15 mA. In this injection locking measurement, the FP laser was driven with 35 mA current, which is a little higher than twice of the threshold current.

The lasing spectrum of the FP laser is measured with varying injection power. The modes that are numbered in the figure will be followed during the measurement. Modes 1 and 7 are the favored modes in the FP cavity, and the master laser emits at 1547.19 nm, which is close to mode 3 (Fig. 3.13). When the external light is strong enough, all the power of the FP laser is at the frequency of the master laser. This is shown in the top two spectra in Fig. 3.13, when the sidemode suppression ratio (SMSR) is larger than 20 dB. Fig. 3.14 indicates how the modes 1 to 7 compete for the gain as a function of the increasing injection power as the power in mode 3 increases and finally reaches the locked status.
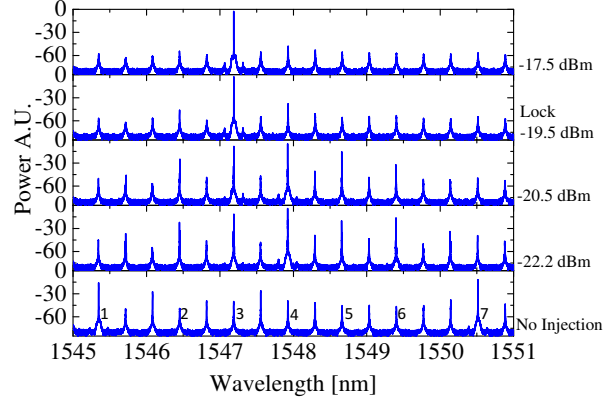
Figure 3.13: Measured optical output spectra of the FP laser with no laser injection and with laser injection power increasing from $-22\,\mathrm{dBm}$ to $-17\,\mathrm{dBm}$. FP laser is under injection current of 35 mA at 18°C. At injection power of $-19.5\,\mathrm{dBm}$, the laser is locked.
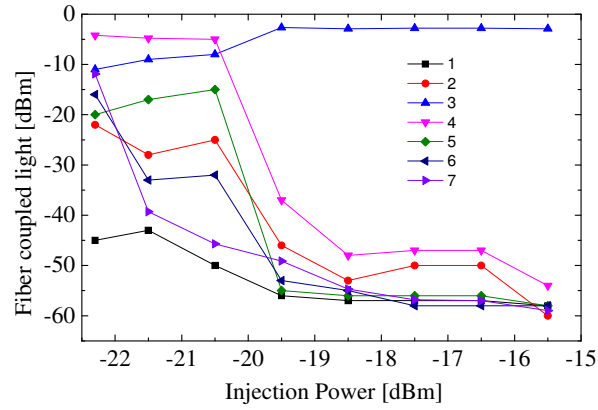

Figure 3.14: The power change of modes 1 to 6 as a function of the injected laser power at a wavelength close to that of mode 3.

The locking range of this FP laser at $35\,\text{mA}$ pump current for mode 3 is also measured. The locked region is determined by both frequency detuning and the scanning external injection light power at a fixed laser pump current. At each injection power, the wavelength is swept from below and above the frequency of mode 3, and the frequencies when the mode loses locking are recorded and plotted in Fig. 3.15a versus the square root of the injection power.

In theory, the locking bandwidth is expressed as a function of the injection rate $(c/2n_\text{g}L) \cdot \sqrt{S_\text{i}/S}$ and the phase difference θ [97]:

$$\Delta\omega = \frac{c}{2n_\text{g}L}\sqrt{\frac{S_\text{i}}{S}} \cdot (\sin\theta - \alpha\cos\theta) \tag{3.2}$$

where S_i is the external injected power and S is the emitted power by the slave cavity; θ is the phase difference between the injected and the free running field in the slave laser. c is the light velocity in vacuum, n_g the group index, L the cavity length. In Eq. 3.2 $\Delta\omega$ includes two parts: one is the detuning between the angular frequencies of the master injected light and the FP slave laser; the other part is from the slave laser frequency shift due to the optical injection as caused by the carrier-density induced refractive index change. Eq. 3.2 describes the linear relation between the detuning and the square root of the injection power.

By setting $\rho = (c/2n_\text{g}L) \cdot \sqrt{S_\text{i}/S}$ and $\theta_0 = \arctan\alpha$, the locking bandwidth $\Delta\omega$ can be rewritten as $\rho\sqrt{1+\alpha^2} \cdot \sin(\theta - \theta_0)$. It is then clear that $|\Delta\omega| \leq \rho\sqrt{1+\alpha^2}$, as $\sin(\theta - \theta_0) \leq 1$ is always true. Moreover, $\Delta\omega$ is restricted by the physical requirement that the injection-induced change in gain, which according to [98] is given by $\Delta G = -\rho\cos(\theta)$, be negative, i.e. $-\pi/2 < \theta < \pi/2$. In this interval the smallest value is $-\rho\sqrt{1+\alpha^2}$ for $\theta = \theta_0 - \pi/2$ and the largest value is for $\theta = \pi/2$. Hence, $\Delta\omega$ is bound by

$$-\rho\sqrt{1+\alpha^2} \leq \Delta\omega \leq \rho \tag{3.3}$$

The locking bandwidth is clearly asymmetric. From Eq. 3.3 we know $\Delta\omega_\text{max} = \rho$, $\Delta\omega_\text{min} = \rho\sqrt{1+\alpha^2}$, thus the linewidth enhancement factor can be obtained as

$$\alpha = \sqrt{\left(\frac{\Delta\omega_\text{min}}{\Delta\omega_\text{max}}\right)^2 - 1} \tag{3.4}$$

In Fig. 3.15a the locking detuning frequency is plotted with respect to the square root of the injection power according to 3.2. The boundaries of the locking region are fitted with linear fits shown as the two lines. Using the value extracted from the fits, and Eq. 3.4 the linewidth enhancement factor of the Oclaro active material can be estimated to be 2.6 ± 0.2 at the wavelength around $1550\,\text{nm}$, which has a good agreement with the value of a typical QW laser

Inspection of the dependency of the locked region with respect the detuning (Fig. 3.15a) shows that the locked region indeed has an asymmetric shape with respect to the zero detuning. This is due to the coupling between the amplitude and phase of the electric field in the semiconductor [99]. When the light injection increases, the laser intensity increases and decreases the carrier density, which increases the refractive index. As a result of the refractive index increase, the longitudinal mode wavelength also increases, i.e. the light injection increases the longitudinal mode wavelength. Therefore, optimum matching between the injected light wavelength and the longitudinal mode resonance wavelength is obtained, and the injected mode intensity takes its maximum at a wavelength longer than the original longitudinal mode wavelength. When the injecting light wavelength changes to a longer wavelength from the optimum wavelength, the mode intensity decreases very rapidly, because the carrier density increases and the refractive index decreases with detuning, which accelerates the detuning.

Fig. 3.15b plots the locking frequency width as a function of injection power for modes 1, 3, and 7 numbered in Fig 3.13a. Among all the modes in Fig 3.13a, mode 1 and 7 are the favored modes in the FP cavity by the intra-cavity reflection (see Sec. 3.3). The recorded locking range in Fig. 3.15b illustrates that favored modes are easier to lock compared with the "normal" modes. Furthermore a higher FP output power requires a larger injection power to lock.

3.5   Discussion and conclusion

In this chapter we looked at the design of Fabry–Pérot lasers with multi-mode interference reflectors. In addition, different test lasers have been designed and fabricated to obtain the MIR reflectivity experimentally and to measure the group index of shallowly etched waveguides. The performance of the MIR lasers and of the cleaved-facet lasers has been investigated, and with the analysis we obtained important information for the subsequent multi-wavelength laser design, which is the subject of the next chapter. There the MIR-based FP laser is used as an important building block. Furthermore, with the injection locking measurement on the MIR-based FP laser, we found that the injection power that would be required to lock the laser mode is around 5% of the laser emitted power. The linewidth enhancement factor has also been derived from the injection locking test and was estimated to be 2.6 for the Oclaro laser structure. This value will also be used in the laser feedback stability model to investigate the multi-wavelength laser (in chapter 4).
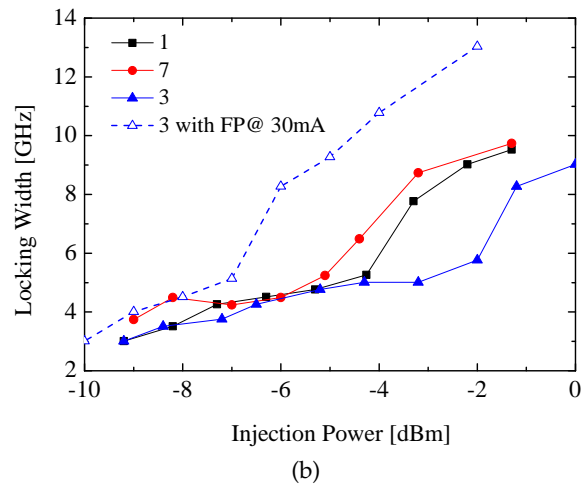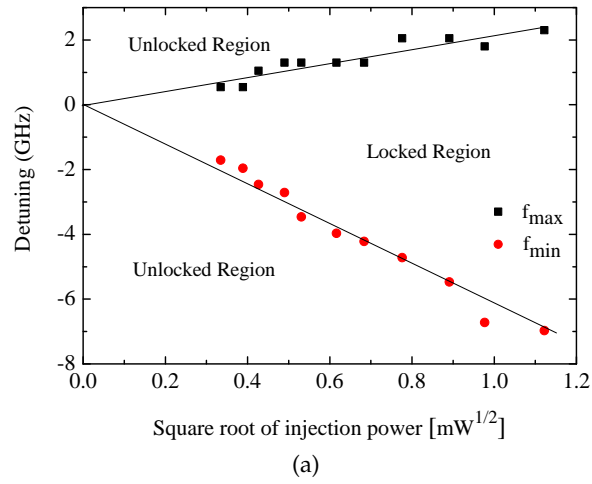
(a)

(b)

Figure 3.15: (a) Frequency locking range dependence on injected power. The FP laser A420 has a injection current of 35 mA at 18°C; (b) Locking width for mode 1, 3 and 7 at a FP laser injection current of 35 mA and for mode 3 at an injection current of 30 mA.

Chapter 4

Filtered-feedback multi-wavelength laser

This chapter describes the design and characterisation of the filtered-feedback multi-wavelength laser mentioned in Chapter 2. It is based on an array of Fabry-Pérot (FP) lasers and an arrayed waveguide grating (AWG). The chapter addresses the basic laser characterisation and linewidth measurement. Then the simultaneous lasing of four channels is described. The chapter ends with a study on the stability of the filtered-feedback laser and a comparison of the filtered-feedback phase-induced dynamics of the laser with a stability analysis model [60].

4.1 The filtered-feedback multi-wavelength laser

The operating principle of this multi-wavelength device can be understood from its schematic representation which is shown in Fig. 4.1a. The device consists of an array of FP lasers, each of which is formed by a semiconductor optical amplifier (SOA) and two on-chip broadband multi-mode-interference reflectors (MIRs). The reflectors have reflection and transmission ports, the latter to couple light into and out of the cavity. One side of each FP laser is coupled to an AWG filter through a phase shifter. The FP lasers generate a broad spectrum of longitudinal modes, the spacing of which is determined by the optical length of the cavity. The AWG multiplexes the light of the FP laser channels to a common output, which is connected to another on-chip broadband reflector. This reflector will reflect the light and subsequently the AWG will demultiplex the reflected signals and route them back to each FP laser. Only the FP modes that match in wavelength with the AWG passband are selected and are fed back to the laser cavity. The filtered-feedback mode with the highest power will enhance this particular longitudinal mode inside the cavity and the laser will lock on

(a)

(b)
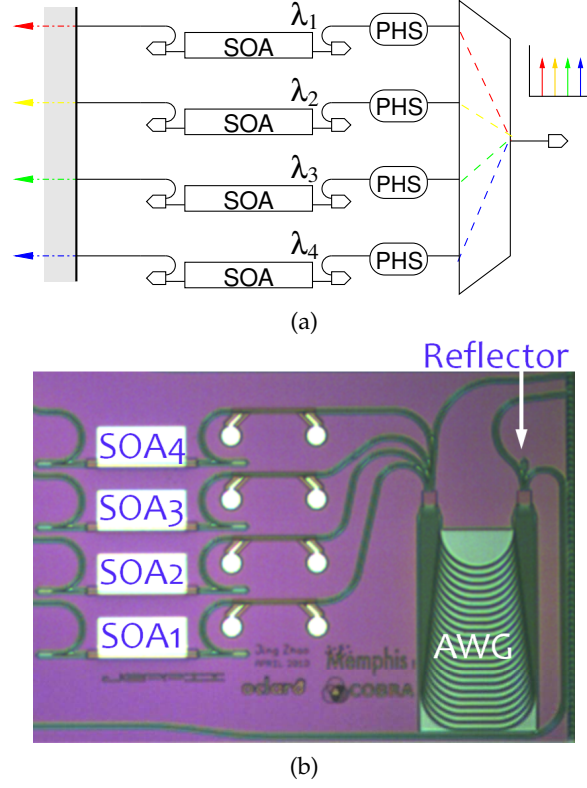
Figure 4.1: (a) Schematic of the device and (b) Microscopy photograph of the realized device. The chip dimensions are approximately 2 mm × 2.5 mm.

that wavelength, thus achieving single-mode operation. The phase shifting sections (PHS), see Fig 4.1a, can adjust the feedback phase with the FP-cavity modes.

Fig. 4.1b shows a microscope photograph of the fabricated multi-wavelength laser. There are four channels of lasers from bottom to up labelled 1 to 4. Here we use two-port multi-mode-interference reflectors (MIRs) [85] as broadband on-chip reflectors with SOAs to form the four FP laser cavities (Fig. 4.1b) [100]. The reason is that the simple fabrication of the MIRs makes the whole device compatible with the standard active/passive integration process of the fab. The laser gain sections are 360 μm long. This length is chosen to provide sufficient gain and aims to ensure a 50 GHz longitudinal mode spacing in the FP laser cavity, the physical length of which can be accurately designed because the elements are made with lithographic precision. The optical length of the cavity is calculated to be $L_{\text{ocav}} = 2 \times L_{\text{reflector}} \times N_{\text{g,p}} + (L_{\text{gain}} + 2 \times L_{\text{ds}}) \times N_{\text{g,a}}$, where $L_{\text{reflector}}$ and L_{ds} are the length of the reflector component

and the deep-shallow transition with fixed design values, L_{gain} is the length of gain section, and $N_{g,p} \approx 3.73$, $N_{g,a} \approx 3.56$ are the group indices of the passive and active waveguide respectively, which are calculated from the FP laser devices in chapter 3. Since the mode spacing $\Delta f = c/(2 \times L_{ocav})$, where c is the speed of light in vacuum, the gain section length of 320 μm corresponds to a mode spacing of 50 GHz (0.4 nm). In the filtered-feedback section, the AWG was designed using a in-house design tool, which is base on the theory discribed in [64]. The AWG has a central wavelength of $\lambda_0 = 1550$ nm, with 5 inputs and 3 outputs. Four of the inputs are connected to the four FP lasers and the other one is used as test port. The AWG has spectral channels spaced $\Delta f_{AWG} = 200$ GHz (1.6 nm), such that there are four FP modes in each AWG channel. The free spectral range (FSR) of the AWG is six times its channel spacing, FSR $= 6 \times 1.6$ nm $= 9.6$ nm. On the output side of the AWG, the central port is connected to a one-port MIR to provide a common reflector, with approximately 80% reflection [84]. The other output ports are left as test waveguides. Additionally, 250-μm-long phase shifting sections (PHS) are placed between each FP laser and the AWG wavelength selection section to allow the control over the phase of the feedback signal. On the left side of the FP laser arrays there are the separate outputs of the multi-wavelength lasers. Note that here the phase shifting sections used are the standard building blocks of electro-optic phase modulator mentioned in chapter 2. But due to the limited space, a length of 250 μm is chosen instead of the standard length 1 mm, and they will be used as foward-biased phase shifters. The forward-bias phase shift efficiency is 15 degree per 1 mA injection current, which is calibrated from test devices with forwards-biased phase shifters in a Mach-Zehnder interferometer configuration[101].

4.2 Basic laser characterisation

For performing the basic laser characterisation, the device was mounted on a copper chuck and its temperature was stabilized at 20 °C during the measurement. A lensed fibre mounted on a nano-positioning stage is used to collect the light. The light is coupled out from an angled facet which is not shown in Fig. 4.1b. In the figure, the four channels of the laser are labeled from one to four.

Fig. 4.2 presents a zoom of the measured spectrum from channel 1 at threshold. In this graph we observe the subthreshold longitudinal modes of the FP cavity, which are spaced by 0.39 ± 0.01 nm. This corresponds to a frequency spacing of 49.5 GHz, 1% deviation from the ITU (International Telecommunication Union) spacing for which it was designed. The dashed lines in Fig. 4.2 indicate the simulated AWG transmission bands with a spacing of 200 GHz. When one of the FP modes aligns with the peak transmission of the AWG, single mode lasing at that wavelength will occur.

Fig 4.3 shows the *L-I* and *V-I* curves of one laser channel; this is representative for all channels. The lasing threshold current for each channel is around 16 mA. Chan-
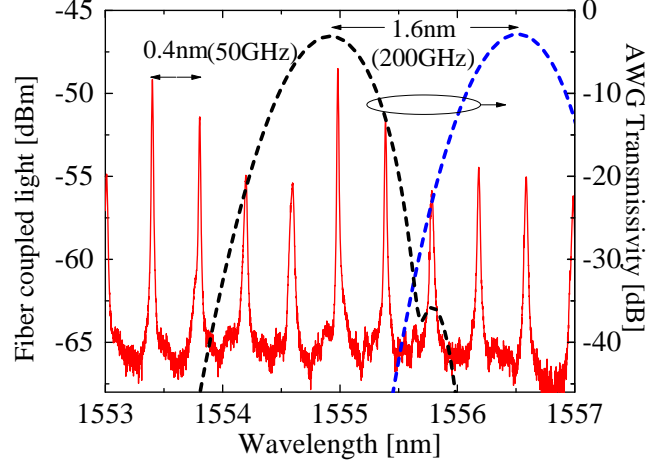
Figure 4.2: Part of channel 1 spectra showing the subthreshold modes (solid ine) and two simulated AWG passbands (dashed lines).

ging the injection current into the amplifier will change the behaviour of the laser. Different lasing modes will be present. This is illustrated in Fig. 4.4 which shows the measured spectra for different injection currents. With the increase of the injection current, one or more lasing modes are hopping, mostly between 3 orders of the AWG passbands, which are each separated by one free spectral range (FSR), which is 9.6 nm for this device. The change of the lasing mode is also the reason for the irregular shape of the *L-I* curve shown in Fig. 4.3. When the current increases, the optical phase inside the FP cavity changes. This phase change is induced by a change in effective group index, which is caused by the changing current and the resulting temperature variation. The optical phase change will shift the frequency of the FP modes and alter the spectral alignment of those modes with the AWG passband. As discussed in chapter 3, spurious reflections inside the FP cavity lead to certain preferred modes in the FP laser. The selected lasing mode is the result of the combination of the AWG filter and the location of the preferred FP modes. Our device has not been designed to suppress higher order passbands of the AWG (e.g. through chirping of the array [102]), so lasing operation in a single order of the AWG is not guaranteed.

By controlling the current injection to each laser channel carefully, we can select the position of the longitudinal modes. Single wavelength lasing is obtained for four adjacent channels within a single order of the AWG. The spectra of these simultaneously operating laser channels are superimposed in Fig. 4.5a. The four lasing peaks correspond to the laser channels labeled 1 to 4 in Fig. 4.1b. The injection current and

Figure 4.3: Laser L-I curve and I-V curve.

Figure 4.4: The spectrum of the laser with different injection currents.

(a)

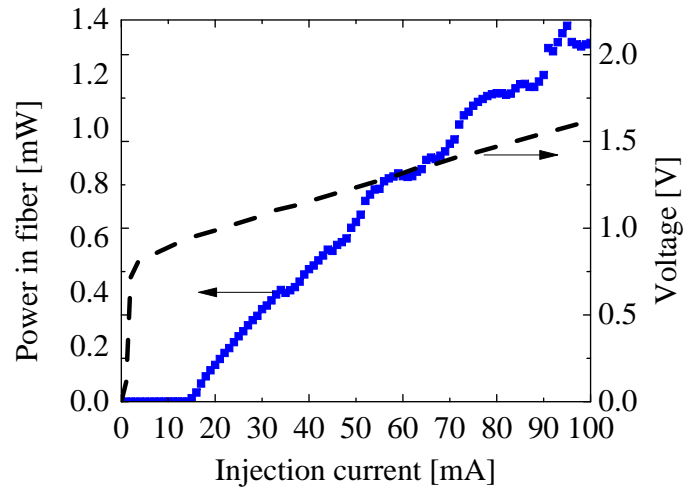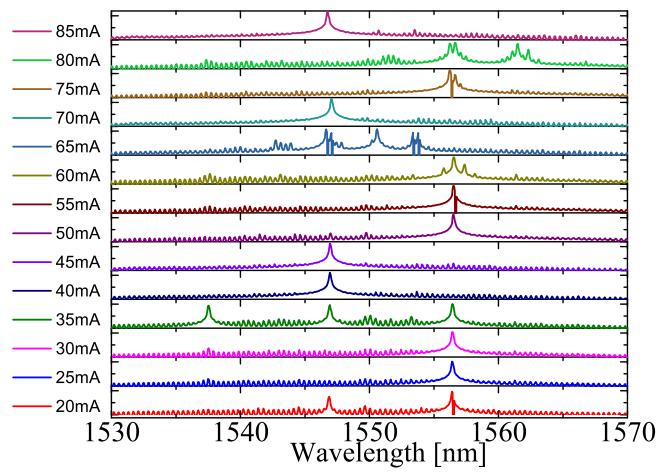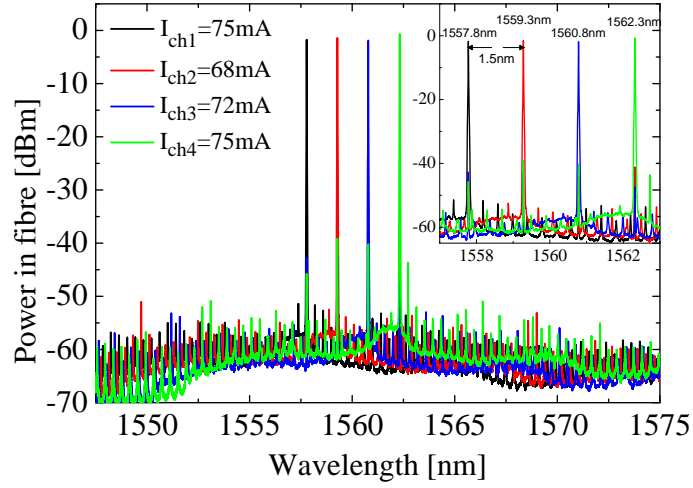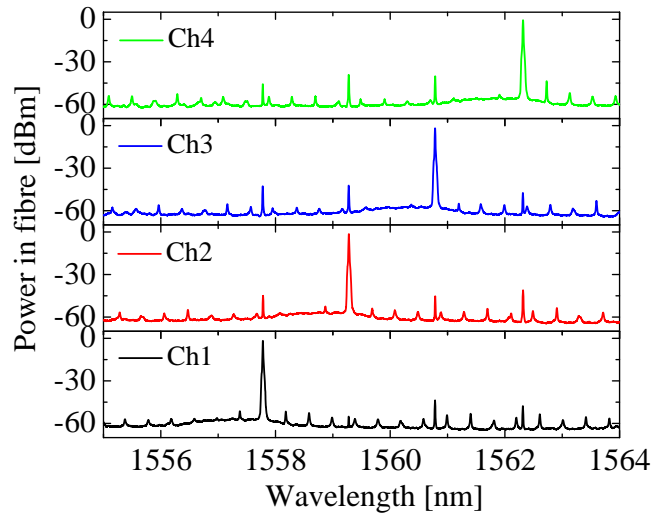(b)

Figure 4.5: (a) Superimposed lasing spectra of the four simultaneously operating laser channels; (b) Spectrum of each channel plotted separately.

lasing wavelengths are indicated in the figure. The wavelength distance of the lasing channels is around 1.52 nm, which is close to the designed AWG channel spacing of 200 GHz (1.6 nm). The sidemode suppression ratio (SMSR) is more than 40 dB in all cases. From the Fig. 4.5b, which shows the spectrum of each laser channel, the optical crosstalk into the other laser channels is observed. This should not be confused with laser sidemodes, but instead is due to the crosstalk of the AWG. The level of this crosstalk is seen to be less than -35 dB. When the laser signals are multiplexed by another AWG, we expect the crosstalk to be suppressed by an additional factor of ~30 dB.

4.3   Linewidth

The linewidth is often defined in terms of the full width at half maximum (FWHM) of the optical field power spectrum. The broadening of a laser line is mainly due to fluctuations in the phase of the optical field. These arise from two basic sources, a) spontaneous emission which changes the phase and intensity of the lasing field and; b) carrier density fluctuations.

For the calculation of the linewidth of our stable single-mode laser, the starting point is a formula given by Henry [103], which can be expressed as

$$\Delta\nu_0 = \frac{v_g^2 n_{sp} h\nu(1+\alpha^2)\ln(R_m^{-1})}{4\pi P_s \eta L^2} = \frac{n_{sp} h\nu(1+\alpha^2)\ln(R_m^{-1})}{\pi P_s \eta \tau_{in}^2} \qquad (4.1)$$

where v_g is the group velocity, n_{sp} a numerical factor of order unity, ν the optical frequency, R_m the power reflectivity of the mirrors, η the quantum efficiency, $L = v_g\tau_{in}/2$ the cavity length and τ_{in} the internal cavity roundtrip time. This formula takes no account of external feedback. We can include the external feedback by modifying the linewidth according to Agrawal [104], as follows

$$\Delta\nu = \frac{\Delta\nu_0}{[1 + C\cos\Phi]^2} \qquad (4.2)$$

where the feedback coupling parameter $C \equiv \gamma\tau\sqrt{1+\alpha^2}$ and Φ is the phase angle between the cavity field and the feedback field;. Here $\Phi = \omega\tau$ where ω is the angular frequency in the presence of feedback, and the field couples back into the laser cavity after a delay τ. In general, the linewidth decreases with increasing laser power and an optimized feedback phase can give a further reduction of the original laser linewidth.

Accurate measurement of linewidth in multi-section devices requires careful control. Grating-based optical spectrum analysers (OSAs) do not offer the measurement resolution required for laser linewidth measurement. A spectrum analyser based on an interferometric method, the APEX AP2041B with 0.16 pm resolution (20 MHz), has
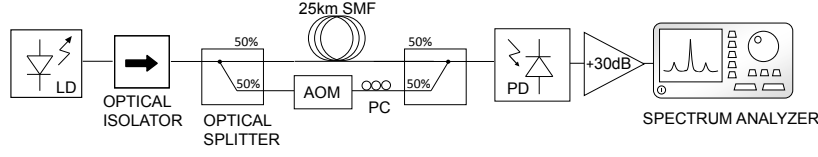
Figure 4.6: Self-heterodyne linewidth measurement setup.

been tried, but it could still not resolve the linewidth of our filtered-feedback laser. Consequently, a delayed self-heterodyne method [105] has been used to measure the linewidth. The setup used for this measurement is shown in Fig. 4.6. After passing through the optical isolator, the fibre-coupled laser output light is split into two paths by the optical splitter. One path is frequency-shifted in the acousto-optic modulator (AOM) by a frequency F. The other path is sent through a long delay line of 25 km long single mode fibre. Since the time delay is much longer than the coherence time of the laser, the two output signals are no longer correlated, when combined in the beam combiner. The two combined signals interfere as if they are from two independent lasers offset by a frequency shift. The AOM shifts the detection frequency away from DC, where the RF spectrum analyser does not work well.

The two optical fields incident on the photodiode (PD) are

$$E_{\mathrm{s}} = \sqrt{P_{\mathrm{s}}(t)} \exp\left\{ j \left[2\pi\nu_{\mathrm{s}} t + \phi_{\mathrm{s}}(t) \right] \right\} \tag{4.3}$$

$$E_{\mathrm{lo}} = \sqrt{P_{\mathrm{lo}}(t)} \exp\left\{ j \left[2\pi\nu_{\mathrm{lo}} t + \phi_{\mathrm{lo}}(t) \right] \right\} \tag{4.4}$$

In these expressions $P_{\mathrm{lo}}(t)$ and ν_{lo} are the power and optical frequency of local oscillator, while $P_{\mathrm{s}}(t)$ and ν_{s} are the power and optical frequency of the frequency shifted signal. $\phi(t)$ is the phase of the field and it takes all phase noise into account. The addition of the two light waves in the beam combiner leads to interference and causes intensity variations that are detectable using a photodiode. The photodiode gives a current proportional to the power of the sum of the two waves

$$\begin{aligned} I \quad &\propto \quad (E_{\mathrm{s}} + E_{\mathrm{lo}}) \left(E_{\mathrm{s}} + E_{\mathrm{lo}} \right)^{\star} \\ &= \quad P_{\mathrm{s}}(t) + P_{\mathrm{lo}}(t) \\ &\quad + 2\sqrt{P_{\mathrm{s}}(t)P_{\mathrm{lo}}(t)} \cos\left[2\pi t \left(\nu_{\mathrm{s}} - \nu_{\mathrm{lo}} \right) + \phi_{\mathrm{s}}(t) - \phi_{\mathrm{lo}}(t) \right] \end{aligned} \tag{4.5}$$

The first two terms correspond to the photocurrent for direct intensity detection and the third term is the heterodyne mixing term. The electronic spectrum of Eq. 4.5 will ignore the rapid fluctuations in P_{s} and P_{lo}, but produce a peak centred around the acoustic frequency $F = |\nu_{\mathrm{s}} - \nu_{\mathrm{lo}}|$ and with a width, determined by the phase fluctuations $\phi_{\mathrm{s}} - \phi_{\mathrm{lo}}$, which is twice the original width. This heterodyne measurement
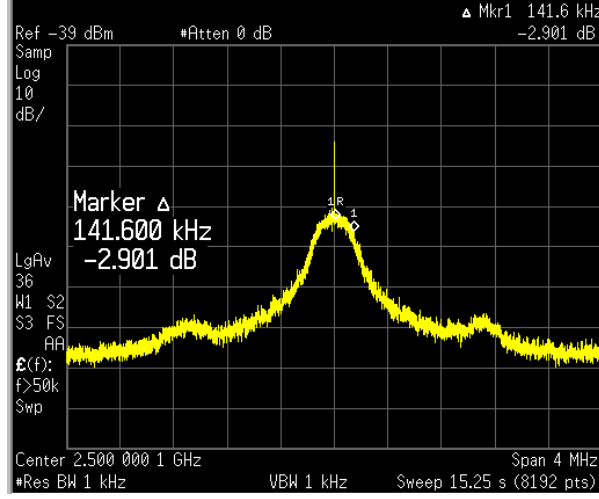
Figure 4.7: Mixer output spectrum as shown on the electrical spectrum analyser (ESA). The original spectral width is estimated from the mixer output spectrum to be 150 KHz. The marker measures the Δf from the top of the peak (excluding the spike) to 3 dB power drop on one side.

technique can be considered as a single-delay autocorrelation. The optical field at frequency f autocorrelates with the delayed and frequency shifted version of itself to produce a time-fluctuating spectrum centred at frequency F.

This measurement reveals that the smallest FWHM observed for this laser is less than 200 kHz. Fig. 4.7 shows the mixer output spectrum on the electrical spectrum analyser, for a case where laser channel one is biased at 72 mA. This yields a laser linewidth of ~150 kHz.

4.4   Stability theory and model

The lasers under study are subject to filtered feedback [106]. The filtering is achieved by the presence of the AWG. The main purpose of the AWG is to provide slightly reduced loss for the longitudinal mode that falls within a certain channel, so as to force that laser to operate in one particular mode. As the effective width (3-dB passband) of one channel of the AWG is ~50 GHz and the laser operates in a single mode, of which the feedback-induced frequency shift (<2 GHz) is much smaller than the passband of the filter, the filtering effect does not influence the selection of the lasing mode. Therefore, the feedback can be modelled as conventional feedback [107], which simplifies the treatment and leads to good qualitative agreement with obser-

vations.

We will express the optical field inside the laser cavity as

$$\sqrt{P(t)}e^{i\phi(t)+i\omega_0 t} + c.c$$

where the power P and the phase ϕ depend slowly on time on the scale of the rapid oscillations implied by the optical frequency ω_0 of the solitary laser and $c.c.$ stands for complex conjugate. The power is in dimensionless units, such that P is the number of photons in the cavity. The variable characterizing the gain is the slowly time-dependent number of electron-hole pairs $N(t)$, taken with respect to its threshold value for the solitary laser (i.e. without feedback). In terms of the three variables P, ϕ and N, the equations describing the time evolution of the laser in the presence of feedback are

$$\dot{P} = \xi NP + 2\gamma\sqrt{P(t)P(t-\tau)}\cos[\phi(t) - \phi(t-\tau) + \omega_0\tau]; \tag{4.6}$$

$$\dot{\phi} = \frac{1}{2}\alpha\xi N - \gamma\sqrt{\frac{P(t-\tau)}{P(t)}}\sin[\phi(t) - \phi(t-\tau) + \omega_0\tau]; \tag{4.7}$$

$$\dot{N} = -(1/T_1 + \xi P)N - \Gamma_0(P - P_0). \tag{4.8}$$

where ξ is the linearized gain coefficient at threshold; γ is the feedback rate, defined as [107]

$$\gamma = \frac{r_{\text{ext}}(1 - r^2)}{\tau_{\text{in}}r} \tag{4.9}$$

with r_{ext} the (amplitude) reflectivity of the external mirror, r the (amplitude) reflectivity of the laser mirror and τ_{in} the internal roundtrip time of the laser cavity. The parameter τ is the feedback delay time and α the linewidth-enhancement factor; T_1 is the effective carrier lifetime for spontaneous recombination at threshold, Γ_0 the cavity decay rate (inverse photon lifetime) and P_0 the solitary laser power, given by [107],

$$P_0 = \frac{J - J_{\text{thr}}}{\Gamma_0} \tag{4.10}$$

where J_{thr} is the solitary threshold current (in units of electrons per second).

This completes the model for the dynamical description of the laser with feedback section. In the next section we will study the steady-state solutions to the rate equations (4.6), (4.7) and (4.8), followed in Sec. 4.4.2 by a stability analysis for the corresponding stationary state.

4.4.1 Stationary state

Single-frequency laser operation corresponds to solutions of 4.6, 4.7 and 4.8 satisfying

$$P = P_\text{s}; \; N = N_\text{s}; \; \phi = \Delta\omega_\text{s} t \tag{4.11}$$

where P_s, N_s and $\Delta\omega_\text{s}$ are time independent. This yields

$$\Delta\omega_\text{s} = -\gamma\sqrt{1 + \alpha^2}\sin(\arctan\alpha + \omega_0\tau + \Delta\omega_\text{s}\tau), \tag{4.12}$$

$$N_\text{s} = -\frac{2\gamma}{\xi}\cos(\omega_0\tau + \Delta\omega_\text{s}\tau), \tag{4.13}$$

$$P_\text{s} = \frac{P_0 - \frac{N_\text{s}}{\Gamma_0 T_1}}{1 + \frac{\xi N_\text{s}}{\Gamma_0}}. \tag{4.14}$$

First, the frequency shift $\Delta\omega_\text{s}$ is numerically solved from Eq. (4.12). It was shown by Ref. [108] that, so long the feedback strength satisfies $C \equiv \gamma\tau\sqrt{1 + \alpha^2} < 1$, only one single solution to Eq. (4.12). exists. Substituting this solution in Eq. (4.13) yields a value for N_s, where after the value for P_s can be evaluated with Eq. (4.14). Thus we obtain for each setting of the laser, determined by the value of the feedback phase delay $\omega_0\tau$ and the solitary laser power P_0, a set of values for $\Delta\omega_\text{s}$, N_s and P_s. It is important to note that the applied phase ϕ_ps in the phase shifting element will be accounted for in $\omega_0\tau$ as well.

4.4.2 Stability

Now the issue at stake is that the stationary state defined by Eqs. (4.12), (4.13) and (4.14) is not always stable. It is known that the transition from stable to unstable operation is associated with a so-called Hopf bifurcation, which indicates the birth of an undamped relaxation oscillation (RO) [107, 109]. If this happens there are, among others, the following possible scenarios:

1. A self-sustained harmonic RO appears, notable as oscillations in P, N and ϕ, at a frequency approximately given by

$$\nu_\text{R} = \frac{1}{2\pi}\sqrt{\xi(J - J_\text{thr})} \tag{4.15}$$

   with typical values ranging from 1 to 10 GHz.

2. The oscillation period may double (frequency halved), often referred to as period-doubling bifurcation [110].

3. As the amplitude of the RO increases, higher harmonics appear.

4. The oscillations turn chaotic; in case the chaos is fully developed this state of operation is also referred to as coherence collapse [111].

The stability of the state characterized by Eqs. (4.12)-(4.14) is investigated by considering small deviations, i.e. putting

$$\phi = \Delta\omega_s t + \delta\phi; \ N = N_s + \delta N; \ P = P_s + \delta P. \tag{4.16}$$

After substituting Eq. (4.16) in Eqs (4.6)-(4.8) and Eqs (4.12)-(4.14) we obtain, in lowest order, three coupled first-order differential delay equations for $\delta\phi$, δN and δP, which are analysed for solutions with time dependence e^{st} for complex-valued s. This leads to a system determinant with zeros in the complex s-plane. If at least one zero has a positive real part, the corresponding solution, Eqs (4.12)-(4.14), is unstable. This has been investigated using the principle of the argument. In this manner, we have obtained a stability diagram for a laser with delayed feedback indicating whether the laser is stable or unstable as functions of the applied feedback phase ϕ_{ps} (between 0 and 2π) and the applied pump strength p, where the latter is defined as $p \equiv (J - J_{thr})/J_{thr}$. Here, the total effective feedback phase has been taken as $\omega_0\tau = \phi_{ps} + \omega_i' p I_{thr}\tau$, where ω_i' is the (empirical) injection-current-induced frequency shift per mA injection current and I_{thr} is the threshold injection current (in mA), i.e. $I_{thr} = 10^{-3} q J_{thr}$, with q the unit charge. We clearly observe tilted bands of stability and instability, respectively, which connect at 2π. The negative slope of the bands is due to the negative current-induced frequency shift of the solitary laser Fig. 4.8

4.5   Characterisation of stability

We investigated one channel of the integrated filtered-feedback multi-wavelength laser which has an external cavity length of ~3.0 mm. The measurement setup is depicted in Fig. 4.9. The laser chip is mounted on a copper chuck and its temperature is stabilized at 18 °C during the measurements. At this temperature the laser has a threshold current of 16 mA. The electrical currents applied to the SOA and to the phase shifter, respectively, are provided through two probe needles. A lensed fibre mounted on a nano-positioning stage is used to collect the light. An optical isolator is used to avoid the unwanted back reflection into the laser chip. The light is analysed using a 50 GHz bandwidth photodetector with a 200 MHz to 8 GHz 30 dB-gain low noise amplifier connected to a 50 GHz electrical spectrum analyser [Agilent E4448A]. A fraction of the light is sent to an optical spectrum analyser [APEX AP2041B] with a high resolution of 0.16 pm.
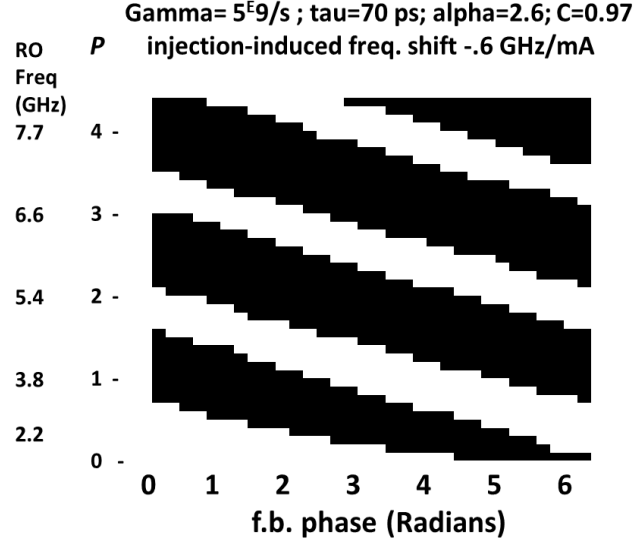
Figure 4.8: Theoretical stability diagram for a single-mode laser vs. pump strength p (vertical) and feedback phase (horizontal), with p defined as $p \equiv (J - J_{thr})/J_{thr}$. Color white denotes stable operation; black denotes unstable. Parameters are: feedback rate $5 \times 10^9 \text{ s}^{-1}$; feedback delay time 7×10^{-11} and $\alpha = 2.6$; the injection-current-induced frequency shift of the solitary laser is $-0.6\,\text{GHz/mA}$. The relaxation oscillation frequency in GHz is given in the left axis label.
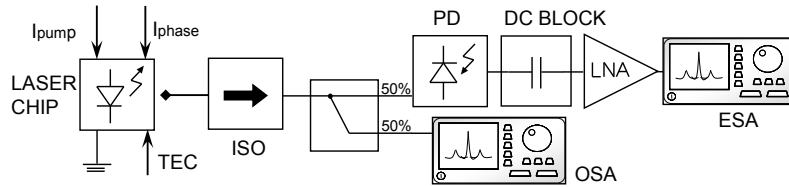
Figure 4.9: The measurement setup. I_{pump} is the laser injection current, and I_{phase} is the current on the phase shifter to tune the feedback phase; TEC denotes the temperature controller; ISO is an optical isolator. After the 50/50 coupler, one of the two branches of light is fed to a 50 GHz photodiode, amplified by a low noise amplifier (LNA) and measured with an electrical spectrum analyser, while the other branch connects to an optical spectrum analyser.

4.5.1 Spectral lasing regimes

Here we investigate the dynamic behaviour of the laser and start from a laser that is operated in a stable single mode fashion. First the SOA injection current is varied while the phase shifter is unbiased,until the laser shows a stable single wavelength lasing mode. Then keeping the injection current fixed to that value, the feedback phase shift is slowly swept from 0° to 210° in steps of 15° by injecting current to the forward-biased phase shifter. The phase shifter has an efficiency of 15° per 1 mA injection current, however, since the feedback light passes the phase shifter twice, the feedback phase change is 30° per 1 mA. We record the optical signal and the noise intensity signal, but only when there is a clear change in the signal appearance. The result is presented in Fig. 4.10. Regions exhibiting strong laser dynamics have been observed for certain feedback phase conditions, and the size of these regions varies with the injection current levels applied to the SOA. The results presented in Fig. 4.10 have been obtained by applying a fixed current of 65 mA to the SOA.

The electrical spectrum (Fig. 4.10a) presents a flat and relatively low-power response. The relaxation oscillation (RO) frequency is damped below the noise level of the spectrum analyser. With the feedback phase tuned to 90° (Fig. 4.10b), the laser is not stable anymore. The RO becomes undamped and it is identified as a narrow peak in the electrical spectrum at 6.8 GHz, while in the optical spectrum two series of side peaks appear at distances equal to multiples of the RO-frequency on both sides of the central peak. When the phase is increased (Fig. 4.10c), the laser enters a period-doubling regime, identified by more side peaks in the optical spectrum and a new peak at half the RO frequency in the electrical spectrum. In the next three cases, Fig. 4.10c-e, the RO has developed into a more complicated and ultimately irregular oscillation indicating period doubling and higher-harmonic effects, but with the dominant frequency near the RO frequency. Gradually, after entering the instability region, the noise floor increases significantly, as seen in the noise intensity spectra and optical spectra. The last case presented in Fig. 4.10e ($\phi = 210°$) shows coherence-collapsed operation [111] dominated by relaxation oscillations. The different lasing regimes with different feedback phase are very reproducible.

To get a clearer picture of the overall stability of our filtered-feedback laser, the same phase tuning procedure is repeated for all injection currents above threshold with a step of 2 mA. The situation as in Fig. 4.10a, single wavelength lasing with no relaxation oscillation dynamics, is considered to be stable. We have identified such stable regions and made a stability map, which is plotted in Fig. 4.11a. The map displays the laser stability as a function of the feedback phase (horizontal) and injection current (vertical), where white indicates stability and black indicates instability, which includes all other unstable regimes. With injection current increase, the laser demonstrates different stable regions. The location of these regions changes with changing feedback phase. Unfortunately, the full 2π phase shift could not be achieved, because the phase shifter starts to saturate at currents beyond ~7 mA and is fully saturated at 10 mA (Fig. 4.11a), thus limiting the maximum feedback tuning to 210°.
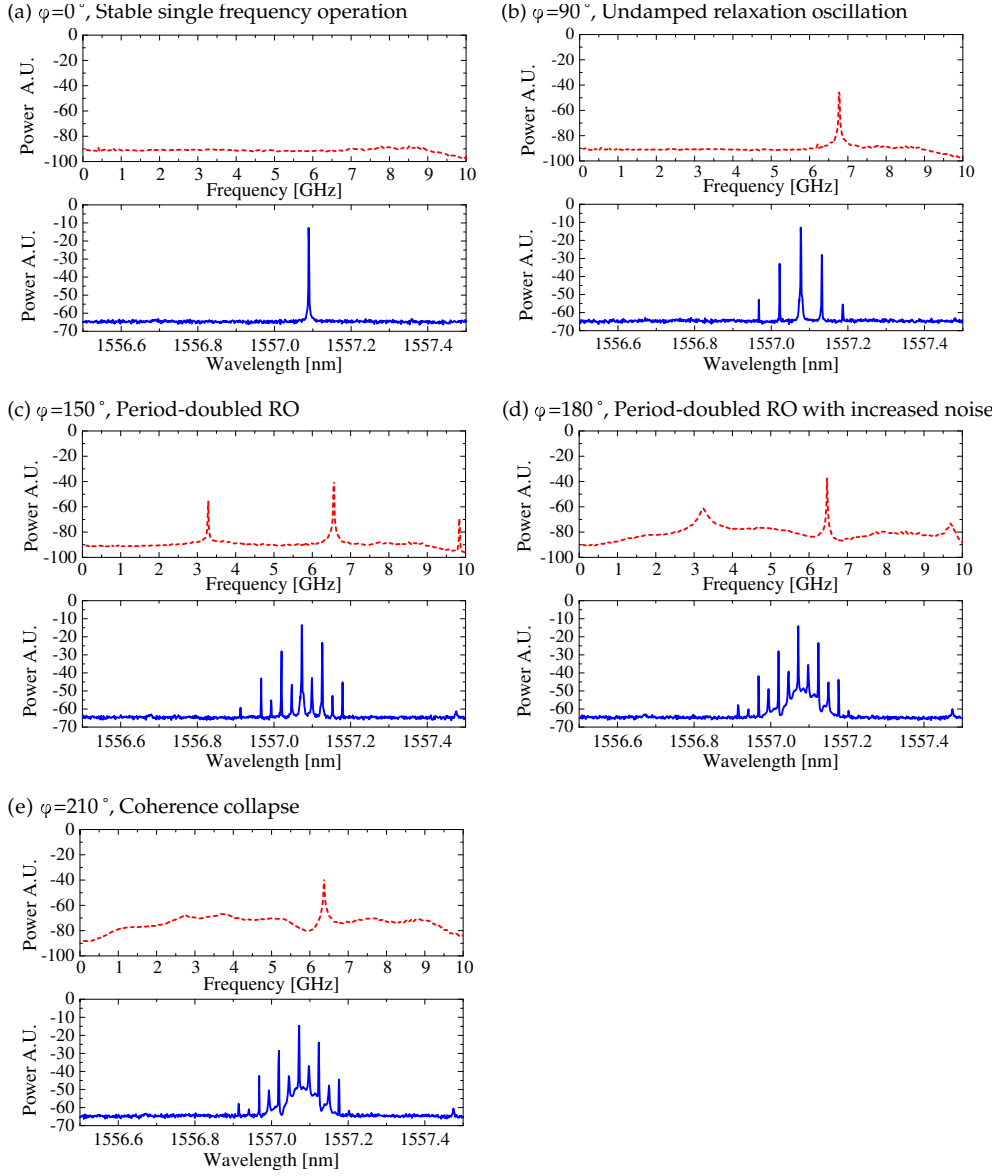
Figure 4.10: Intensity noise (dashed lines) and optical spectral (solid lines) from the ESA and OSA, respectively, for different feedback phase tuning 0º, 90º, 150º, 180º, 210º
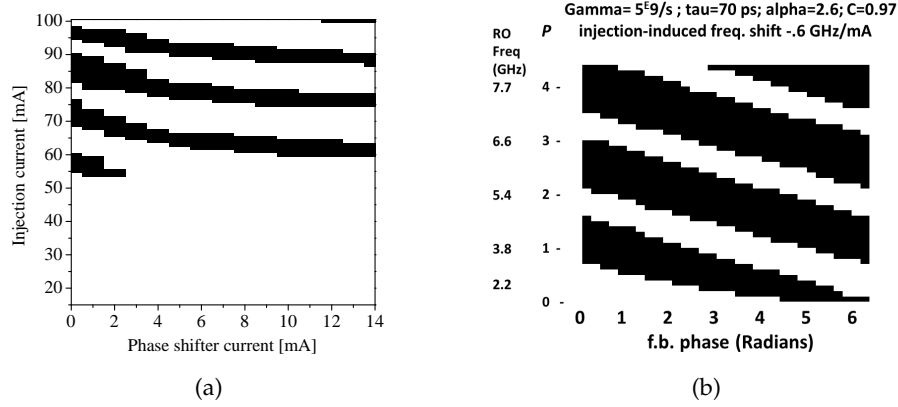
Figure 4.11: Measured map of laser stability versus phase shifter current with differ-
ent injection currents. The dark region is the unstable region and the bright region
is the stable region. (b) Theoretical stability diagram from Fig. 4.8

4.5.2   Stability analysis

As was mentioned in Sec. 4.4.2, we have applied a numerical stability analysis to the
laser with feedback by investigating the dynamical system determinant. Using the
value $\alpha = 2.6$ for the linewidth enhancement factor, as obtained from injection lock-
ing measurements (see Chapter 3), and the external cavity length and loss estimated
as above, we find for the case of injection current of 65 mA (pump strength $p{\sim}3$) that
over a phase range interval of about 100° the single frequency operation is stable,
whereas it is unstable for other values of the applied feedback phase. Apparently,
Fig. 4.10a is within this stability interval.

Fig. 4.11b is the stability map generated from the theoretical model. The stability
situation is recorded as a function of the feedback phase (0-2π; horizontal axis) and
pump strength (injection current from threshold up to 80 mA, $p = 4$, vertical axis).
The parameter values used for this diagram are given in the caption. It is to be noted
that zero phase on the horizontal scale in Fig. 4.11b is arbitrary; it does not neces-
sarily coincide with zero current in Fig. 4.11a. Comparing this with the measured
map Fig. 4.11a, the structures of stable and unstable bands with negative slope show
good qualitative agreement between experiment and theory, although theory pre-
dicts wider unstable bands. The slope is due to the injection current induced phase
shift inside the FP laser cavity. Based on this model, it is possible to optimize the
feedback parameters to enlarge the stable area of the laser, in order to design an
inherently stable feedback laser.

4.6   Conclusion

The design and performance of a filtered-feedback four channel multi-wavelength laser are presented in this chapter. With the short laser cavity formed by the MIRs, combined with the filtered-feedback scheme, the laser threshold current is lower and the output power is higher compared to the AWG-based lasers with the AWG filter inside the main lasing cavity. The four channel laser realizes simultaneous lasing with a wavelength spacing according to the channel spacing designed into the AWG, and an SMSR better than 40 dB. By experimentally and theoretically investigating the linewidth of this filtered-feedback laser, we show that this laser has a very narrow linewidth, which is demanded, for example, in telecommunication applications and sensing. In order to study instabilities and to control stable single-frequency operation, the laser feedback dynamics have been measured as a function of the feedback phase on an integrated external cavity laser. Several nonlinear regimes were observed and controlled by the phase shifter. Comparison of the measurements with the results from a stability model, confirms that the theory that was developed for longer external cavities is still valid for short cavities. We are able to simulate the stability of the device with respect to pump current, feedback phase and delay time. This can lead to optimized designs which have the laser in stable condition for 0 to 2π feedback phase, which means the laser is inherently stable for any value of the feedback phase, thus reducing the complexity of the laser device itself and of the control signals.

Chapter 5

Multi-wavelength transmitter for analog applications

In this chapter the multi-wavelength transmitter and its corresponding analog photonic link using this transmitter are discussed. First we describe the design of the multi-wavelength transmitter and show the measured DC performance of the integrated Mach-Zehnder modulator. We then introduce the analog photonic link and key parameters, such as link gain, frequency response, noise, and distortion of the link. After that, we describe the application of the transmitter in an analog photonic link, which is characterized with respect to the key link parameters. Finally, we investigate the crosstalk between the channels of the multi-channel transmitter.

5.1 Introduction

A fibre-optic link is an opto-electronic system that provides a data connection between two points (point-to-point connection). It essentially consists of a data transmitter formed by a laser light source and a modulation device, a transmission fibre (possibly with built-in fibre amplifiers), and a receiver with photodetector. The modulation device imprints the electrical (RF) signal onto an optical carrier. The photodetector converts the modulated optical signal back into the electrical signal.

As described in the introduction chapter, the analog optic links have recently enjoyed an increasing interest in both scientific research and applications such as antenna remoting, radio astronomy, and radio-over-fibre for wireless systems. In all these cases, the optical link offers low transmission loss, transparency to all modulation formats, as well as light weight and flexibility. The antenna units can be simplified, while the system complexity can be located at a centralized location.

Merging analog optical links with wavelength division multiplexing (WDM) technologies will simplify the system configuration and increase the overall system capacity [112]. In this chapter a monolithically integrated photonic multi-wavelength transmitter is presented. It consists of the four-channel filtered-feedback multi-wavelength laser [100] described in chapter 4, and a Mach-Zehnder modulator array. The transmitter is designed to be used as the wavelength-division-multiplexing (WDM) source to achieve a multi-signal path in a true-time-delay optical beam forming network [113] for the application in a 3~5 GHz smart antenna system.

The circuit design of the multi-wavelength transmitter is divided into two parts: the filtered-feedback multi-wavelength laser (FFMWL) and four identical Mach-Zehnder (MZ) modulators that are connected to each laser channel. The FFMWL has been extensively described in chapter 4. In the present transmitter device, the output of each channel is coupled to one MZ modulator. The modulator outputs, containing the modulated signals, are coupled out of the chip through a 7° angled facet with anti-reflective coating. The schematic layout of this device is shown in Fig. 5.1a. A microscope photograph of the fabricated multi-wavelength transmitter is shown in Fig. 5.1b. As a proof of concept in this first run, this transmitter has a separate output for each channel to allow easy characterisation. In the next runs, the output of different channels will be routed to another AWG to realize a multiplexed output for the WDM source. In each modulator, two 1×2 multi-mode-interference (MMI) couplers are used as power splitter and combiner for the MZ modulator. The phase shift function in the modulator arm is achieved with a 1-mm-long lumped-element electrode on a 1.2-μm-wide deeply-etched ridge waveguide with p-i-n doped epitaxial layers which contain an InGaAsP MQW core. For each modulator, the two arms can be driven independently. The footprint of the transmitter chip is 2×4 mm^2.

5.2   Key parameters in an analog photonic link

The main function of an analog photonic link (APL) is to transmit an analog signal from point to point with high fidelity. Compared to digital optical links, APLs are relatively susceptible to various signal impairments, such as signal loss, noise and nonlinearities. The performance of a link is defined by three primary link parameters: link gain, noise figure and dynamic range. In this section, the definition and the mathematical expression of these parameters will be introduced [114].

5.2.1   Link gain

The photonic link gain is the basic parameter in an APL, on which the other link parameters also depend. A general schematic of an APL is shown in Fig. 5.2. In general an APL can be recognised as a two-port radio frequency (RF) black-box component, which is characterised by an RF input and an RF output. There are two signal con-
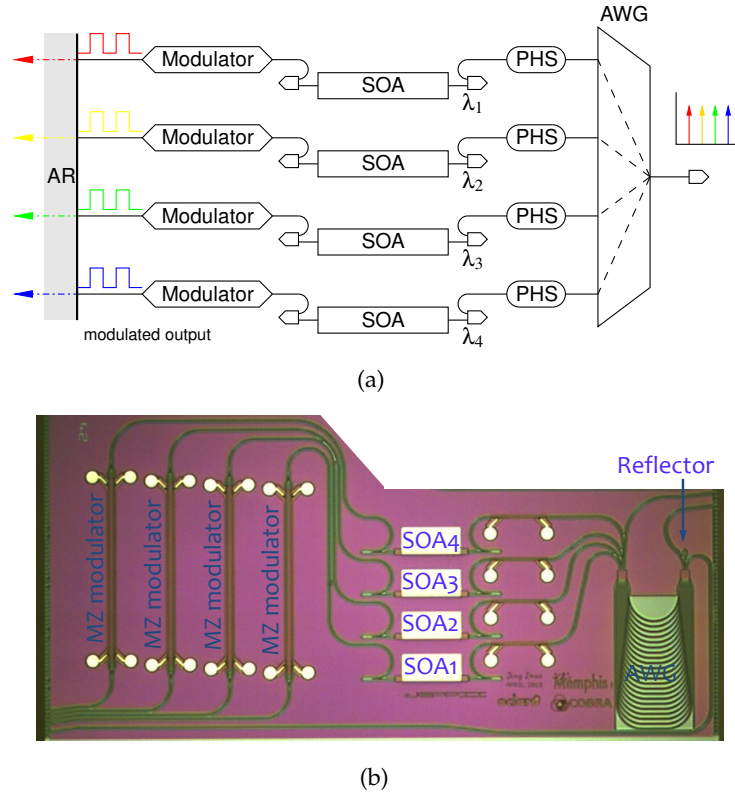
(a)

(b)

Figure 5.1: (a) Schematic of the 4-channel transmitter device and (b) Microscope photograph of the realized device. The chip dimension is 2×4 mm^2.
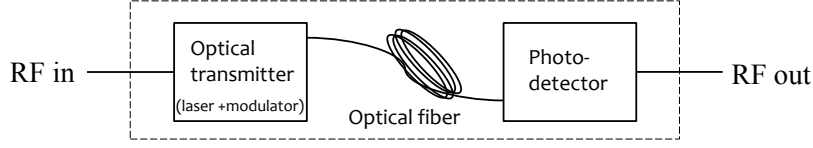
Figure 5.2: Schematic of an analog photonic link.
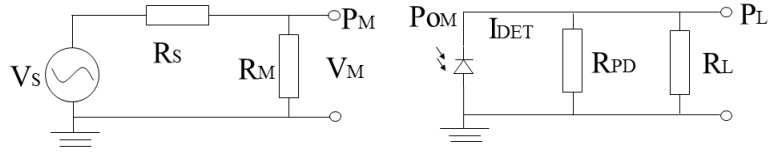
Figure 5.3: Equivalent circuit representation of a photonic link using an impedance-matched Mach-Zehnder modulator and a photodiode detector. P_M is the electrical power available from the signal source; P_{OM} is the optical power from the modulator.

versions in between, from the electrical to the optical domain (E/O), and back from the optical to the electrical domain (O/E). The link gain is the ratio of the RF power observed at the output of the APL relative to the input power. There is no requirement from this definition that the gain be greater than one. Since here our focus is to understand impact of modulation on the link gain, we concentrate on the intrinsic link gain, which is the link gain of an optical link without either optical amplifiers or electrical amplifiers.

Consider our case of an optical link with external modulation, with a source voltage V_s and a source impedance R_s, which is loaded with an impedance-matched Mach-Zehnder modulator (Fig. 5.3). The available power is the electrical power delivered to the modulator. The link gain is the ratio of the RF output, which is the detected power delivered in to a matched load P_L, to the RF input, the power available from the source on the modulator P_M.

$$g = \frac{P_L}{P_M} = \frac{I_L^2 R_L}{V_S^2/4R_S} \tag{5.1}$$

I_L is the current flowing though the load. In case of a matched load $R_L = R_{PD}$, the current $I_L = 1/2 I_{DET}$, i.e. half of the photocurrent generated by the detector. The photocurrent,

$$I_{DET} = \mathscr{R}_{PD} P_{OM} = 2I_L \tag{5.2}$$

with $\mathscr{R}_{PD}$ the responsivity of the detector in units of A/W, and P_{OM} the optical output from the modulator. The optical output from the modulator P_{OM} is based on the

MZ modulator transfer function and the input optical power. Inserting the transfer function of the MZ modulator, using Eq. 2.3, we get

$$P_{OM} = P_{in} T_{MZM} = \frac{P_{in} L_{loss}}{2}[1 + \cos(\Delta\varphi(V_Q))]$$ (5.3)

where V_Q is the reverse bias voltage on the modulator at the quadrature point, and L_{loss} is the insertion loss of the modulator. Substituting Eq. 5.2 and 5.3 into 5.1 yields:

$$g = \frac{P_L}{P_M} = \frac{(\mathscr{R}_{PD} P_{in} T_{MZM})^2}{V_S^2/4R_S} R_L = \frac{\left\{\mathscr{R}_{PD} P_{in} L_{loss}[1 + \cos(\Delta\varphi(V_Q))]\right\}^2}{4V_S^2} R_S R_L$$ (5.4)

where, in an impedance matched system, $R_S = R_L$. From Eq. 5.4 we notice that there are the following ways to increase the intrinsic gain of the link:

1. Increase the responsivity of the detector

2. Reduce the insertion loss of the modulator

3. Increase the optical power input of the modulator

Among these three, increasing the detector responsivity is out of the scope of this thesis. In the measurement, the link uses a commercial detector with 0.8 A/W responsivity; reducing the insertion loss is already achieved by monolithically integrating the modulator with the laser and thereby avoiding additional coupling losses. Hence the optical link gain is mainly dependent on the optical input power of the modulator.

5.2.2 Noise in APLs

There are three dominant noise terms in APLs, thermal noise, shot noise and laser intensity noise. These noises are modeled as current sources and they are independent of each other [114]. In this case, the total noise power in the link is the sum of the noise power generated by individual sources. The total noise measured from the link p_{tot} is expressed as

$$p_{tot} = p_{th} + p_{sh} + p_L \quad [W]$$ (5.5)

with p_{th} the power of the thermal noise, p_{sh} the power of the shot noise and p_L the power of the laser intensity noise.

Thermal noise arises from the thermally induced, random movement of charge carriers in conductors. All the electronics including the load resistance, amplifiers,

photodetector etc., produce thermal noise. The thermal noise does not depend on the optical power and is a constant value with frequency. It only depends on the equivalent temperature of the electrical circuit, the load impedance and electrical bandwidth of the detection system. Nyquist showed that the mean-square fluctuations in the value of the noise current $\left\langle i_{\text{th}}^2 \right\rangle$ across a resistor R_{L} at an absolute temperature T as measured in a bandwidth Δf is given by

$$\left\langle i_{\text{th}}^2 \right\rangle = 4kT\Delta f / R_{\text{L}} \quad [\text{A}^2] \tag{5.6}$$

where k is Boltzmann's constant, which has a value of $1.38 \cdot 10^{-23}$ J/K and Δf is the equivalent noise bandwidth of the receiver in Hz. The temperature used in calculating the noise is the physical temperature of the component. Eq. 5.6 shows that thermal noise has a flat white spectrum, meaning that its power spectral density is nearly constant throughout the frequency spectrum. The power of the thermal noise is

$$p_{\text{th}} = \left\langle i_{\text{th}}^2 \right\rangle R_{\text{L}} \tag{5.7}$$

Shot noise N_{sh} is produced by the quantum nature of photons arriving at the detector. This generates a random fluctuation in the detected photocurrent, which increases proportionally to the the amount of light incident on the photodetector. It can be determined by the measurement of the photo current at the photodiode according to

$$\left\langle i_{\text{sh}}^2 \right\rangle = 2qI_{\text{ph}}\Delta f \quad [\text{A}^2] \tag{5.8}$$

where I_{ph} is the average photocurrent at the load resistance R_{L} and $q = 1.6 \cdot 10^{-19}$ C is the electron charge. The photo current can be determined by measuring the average optical power P_{o} that reaches the photo detector according to $I_{\text{ph}} = \mathscr{R}_{\text{PD}}P_{\text{o}}$ where $\mathscr{R}_{\text{PD}}$ is the responsivity of the photodetector. The power of the shot noise is

$$p_{\text{sh}} = \left\langle i_{\text{sh}}^2 \right\rangle R_{\text{L}} \tag{5.9}$$

Relative intensity noise (RIN) describes fluctuations in the optical power of a laser, mainly stemming from intrinsic optical phase and frequency fluctuations caused by spontaneous emission. Genernal RIN is not white noise, but in the banwidth of interest, assuming that RIN is white noise (constant for all frequencies); moreover, for convenience, RIN is always normalized to a 1 Hz bandwidth so that it becomes easier to compare the intensity fluctuations of the laser when receivers with different bandwidths are used [115], then in linear

scale[1]

$$\text{rin} = \frac{\langle \Delta P(t)^2 \rangle}{P_{\text{Opt}}^2 \Delta f} \quad [1/\text{Hz}] \tag{5.10}$$

where P_{Opt} is the average optical power, and $\Delta P(t)$ represents the fluctuations of optical power from the laser

$$\text{RIN}[\text{dB}/\text{Hz}] = 10 \log \left(\frac{\langle \Delta P(t)^2 \rangle}{P_{\text{Opt}}^2} \right) [\text{dB}] - 10 \log(\Delta f[\text{Hz}]) \tag{5.11}$$

where Δf is the filter bandwidth of the measurement apparatus.

Noise Figure NF is the logarithm of the noise factor F, i.e. $\text{NF} = 10\log_{10}(F)$. The noise factor of a device with input and output ports is defined as the ratio of the available output noise spectral density to the portion of that noise caused by the actual noise source connected to the input of the device, measured at the standard temperature of 290 K [114].

When the input noise is simply the thermal noise from a matched resistor, a more useful definition of the noise figure is the ratio of the input signal-to-noise ratio (SNR) to the output SNR. Suppose that the input and output signal powers are S_{in} and S_{out} and the input and output noise powers are N_{in} and N_{out}, the noise figure can be written as

$$\text{NF} = 10\log_{10} \left(\frac{S_{in}/N_{in}}{S_{\text{out}}/N_{\text{out}}} \right). \tag{5.12}$$

Since the input noise power is the thermal noise from a resistive matched load, $N_{\text{in}} = kT\Delta f$. Moreover, we can identify that $S_{\text{out}} = g \cdot S_{\text{in}}$, which means that the output signal is amplified (or attenuated) by the link gain. For APLs considered here, the output noise is simply the total link noise defined in Eq.5.5, which means that $N_{\text{out}} = p_{\text{tot}}$. Thus, the noise figure expression can be re-written as

$$\text{NF} = 10\log_{10} \left(\frac{p_{\text{tot}}}{gkT\Delta f} \right). \tag{5.13}$$

5.2.3 Nonlinear distortion

To this point, only the linear behaviours of the analog photonic link have been discusses for the link gain and noise figure. However, due to the inherent nonlinearity of the transfer function of the modulator device, the link is a nonlinear system. The nonlinear distortions will limit the range of input power of the APL and in turn limit its performance.

---

[1]Lowercase indicates it is a linear value; uppercase indicates it is a logarithmic value.

Unlike the linear distortion, which can be repaired with a filter, the nonlinear distortion will generate new frequency components that are not present in the original signal [114]. A device could have a perfectly linear transfer function over certain range of input power and still produce distortion when the magnitude of a modulation exceeds the linear range of the device. The power range of the input that can be accommodated by the APL is regarded as the dynamic range. It can be quantified as a ratio between two input power levels subject to some constraints: the noise will limit the minimum signal level that can be transmitted by the link, while the level of distortion defines the upper limit of the signal level.

There are different types of distortion considered here, when a signal is injected into a system.

1. Harmonic distortion (HD) occurs when a single frequency ω (single tone) is injected into a system which is not perfectly linear. Additional output signals (spurs) are generated at harmonics of the input frequency (2ω, 3ω, 4ω, etc). The strength of each harmonic depends on the linearity of the system.

2. Intermodulation distortion (IMD) occurs when 2 (or more) frequencies are injected in to a nonlinear system. Consider two signals ω_1 and ω_2 (two-tone) simultaneously injected into a system. The non-linear interaction of the two signals creates new output signal products (spurs) at the sum and difference frequencies of the two fundamental frequencies, which are so called second order (see Tab. 5.1); In addition to these second order effects, interactions occur between the fundamental frequencies and the harmonics. Third order effects (between one fundamental frequency and the second harmonics of other frequencies) are considered most troublesome, as they usually occur at a frequency near the fundamental frequency and are in the pass band of the system. The frequency and amplitude relation of the intermodulation distortion and the harmonic distortion is listed in table 5.1. The derivation and explanation of this table are in the Appendix on page 88 of this thesis. In the linear part of a system the amplitude of second-order spurs will increase by 2 dB for every 1 dB of increase in the amplitude of the fundamental frequencies. And the third-order spurs will increase 3 dB for every 1 dB the input signals are increased.

A parameter to measure the distortion is the spurious-free dynamic range (SFDR). The SFDR of a system is the range between the minimum signal that can be detected above the noise floor, and the maximum signal that can be introduced into a system without creating distortions (distortion signal is just below the noise level) in a certain measurement bandwidth. The "low" end of this range is limited by noise; the "high" end is determined by the so called third-order intercept point (IP3). As mentioned in previous paragraph, the third order spurs increase by 3 dB for every 1 dB increase in the fundamental frequency. A plot of the output power of the fundamental frequency versus input power would have a slope of 1 at the linear region. A plot of output power at the third order frequency versus input would have a slope of

Component	Harmonic (HD)		Intermodulation (IMD)	
	Frequency	Amplitude	Frequency	Amplitude
DC	0	$a_0 + \frac{1}{2}a_2 A^2$	0	$a_0 + a_2 A^2$
Fundamental	ω	$a_1 A + \frac{3}{4}a_3 A^3$	ω_1, ω_2	$a_1 A + \frac{9}{4}a_3 A^3$
2$^{\text{nd}}$-order	2ω	$\frac{1}{2}a_2 A^2$	$\omega_1 \pm \omega_2$	$a_2 A^2$
3$^{\text{rd}}$-order	3ω	$\frac{1}{4}a_3 A^3$	$2\omega_1 \pm \omega_2,$	$\frac{3}{4}a_3 A^3$
			$2\omega_2 \pm \omega_1$	

Table 5.1: Harmonic (single frequency) and intermodulation (two frequency) modulation.

3 in the linear region of the system. If extending the linear parts of these two plots on the same graph, they would eventually intersect. This intersection point is called the third-order intercept point (IP3). Because there are two different distortions, there are also two types of IP_3 for harmonic distortion and intermodulation distortion. According to Tab. 5.1, the power of harmonic distortion (HD_2) and intermodulation distortion (IMD_2) differ by 3 dB; the power of harmonic distortion (HD_3) and intermodulation distortion (IMD_3) differ by 4.8 dB as

$$P_{\text{IMD}_2}[\text{dBm}] = P_{\text{HD}_2}[\text{dBm}] + 10\log 2 = P_{\text{HD}_3}[\text{dBm}] + 3\,\text{dB} \tag{5.14}$$

$$P_{\text{IMD}_3}[\text{dBm}] = P_{\text{HD}_3}[\text{dBm}] + 10\log 3 = P_{\text{HD}_3}[\text{dBm}] + 4.8\,\text{dB} \tag{5.15}$$

5.3 Measurement setup

In the previous sections we have introduced the important parameters in an analogue photonic link. In the following section, we are going to measure the performance of our filtered-feedback multi-wavelength transmitter in a photonic link based on these parameters.

To measure the performance of the transmitter, the chip and a thermistor are mounted on a dedicated copper cold finger platform as shown in Fig. 5.4a. A Peltier element placed underneath the copper platform is used to stabilize the chip temperature at 28 °C. All the electrodes on the chip have been wire-bonded to their corresponding tracks on a custom-designed printed circuit board (PCB) which is surrounding the copper platform (Fig. 5.4b). Laser current drivers and voltage controllers are connected to the PCB pins, to control the lasers and phase shifters on the chip. For the MZ modulators, push-pull operation can be realised electrically, when the two arms of the modulator are driven by RF signals with opposite phase. This is achieved by

Temperature control circuit

(a)
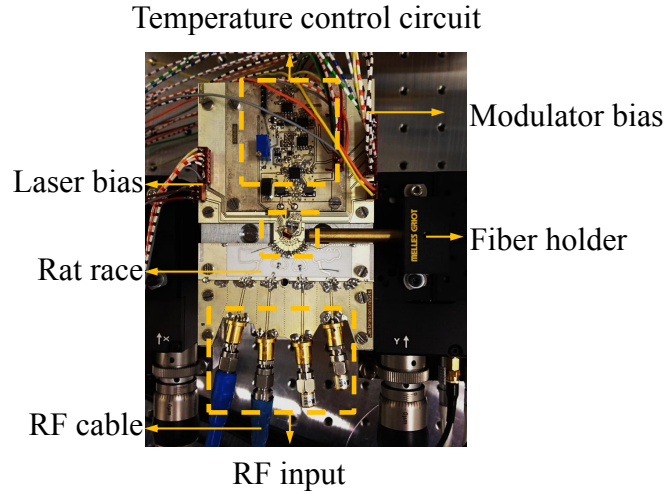
Modulator 50Ω termination
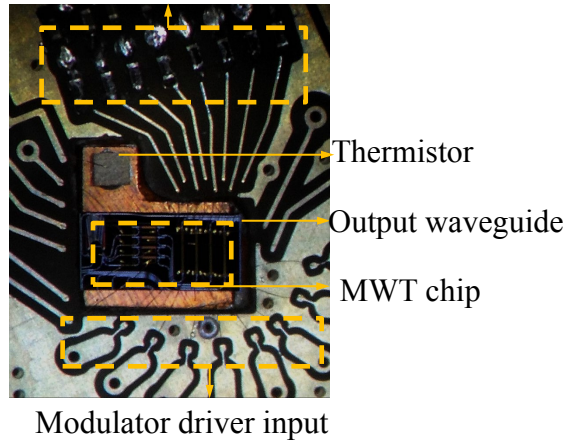
(b)

Figure 5.4: (a) Microscope photograph top view of the transmitter chip on the sub-mount system. PCB A is temperature control system, B is the PCB where the chip is wire-bonded to, C is the rat-race PCB to split the input RF signal in to 2 branches with opposite phase, D is the board with SMA RF connectors; (b) Zoom in of part B: the transmitter chip mounted and wire-bonded to the testing board.

(a)   (b)
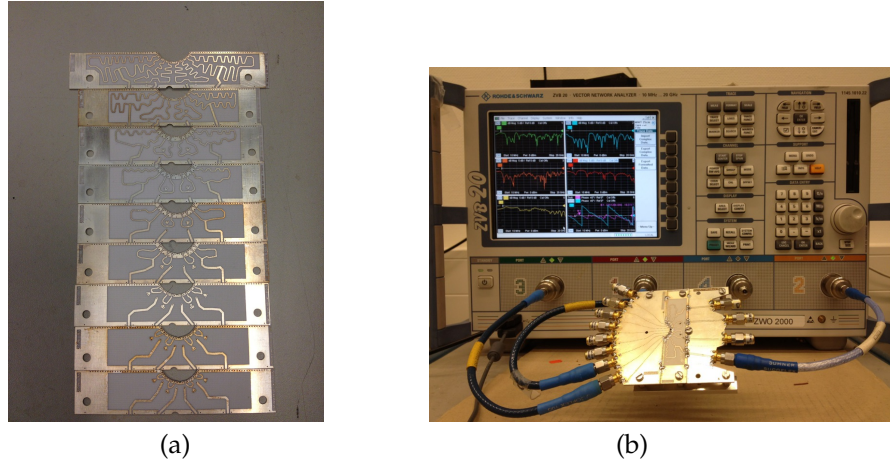
Figure 5.5: (a) Rat-race PCBs. From top to bottom, boards are shown with the operational frequencies centered at 1.5, 2.5, 3.5, 4.5, 6, 8, 10, 12 and 15 GHz, respectively; (b) Measurement setup for characterisation of the rat-race PCBs. The unused channels are terminated with a 50 Ω load.

making use of a so-called rat-race coupler which is integrated on the PCB. The rat-race coupler behaves like a 3-dB splitter, which, for a specific designed frequency range, divides the input signal into two branches with opposite phase [116]. A series of rat-race couplers has been designed and tested, as shown in Fig. 5.5. The electrodes on the output side are terminated with 50 Ω impedances. The modulators are wired-bonded to the PCB as shown schematically in Fig. 5.6a. Coaxial RF SMB (Sub-Miniature version B) connectors are soldered on the board to connect to RF cables for the RF input signal. The light emitted from the output wavelength of the MZ modulators is collected by a lensed fibre that is positioned at the output waveguide of the chip with a 3-axes alignment stage.

The laser used in this transmitter has the same design and properties as presented in chapter 4 with a threshold current of 16 mA and lasing at a wavelength in the range of 1557 nm to 1563 nm. The bias voltages of the MZ modulator are controlled with a voltage supply. In the following measurementthe RF signal is either supplied to the modulator from the port 1 of a electrical network analyser (ENA) or from a microwave signal generator. The network analyser used is HP 7820, 50 MHz to 20 GHz, while the microwave signal generator is from Rohde & Schwarz with a frequency range of 10 MHz up to 30 GHz. After modulation, the optical signal from the modulator is coupled by a lensed fibre and then detected by a photodetector (R2560A) from Emcore. The detector reverse bias is 10 V and the maximum average optical power that can be handled by the detector is 12 dBm which is limited by the distortion of the detector. The output impedance of the photodetector is 50 Ω.
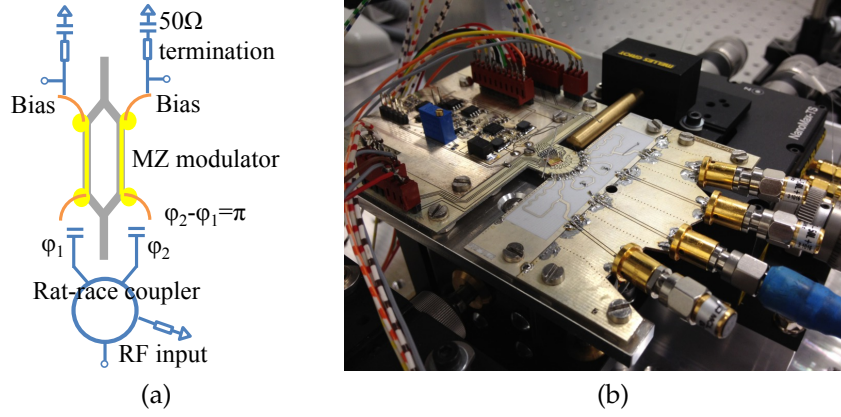
Figure 5.6: (a) Schematic drawing of the connection of each MZ modulator driven in a push-pull manner through a rat-race coupler on the PCB. All the components on the PCB are indicated in blue colour; (b) Side view of measurement setup.

The detector output is connected to a bias-T (100 kHz up to 14 GHz from Ortel). The DC output of the bias-T is connected to a multimeter, while the RF output is either connected to the port 2 of ENA or to an electrical spectrum analyser (ESA) with a frequency range of 9 kHz up to 13.6 GHz, from Rohde & Schwarz. The photograph of the measurement board is shown in Fig. 5.6.

5.4 DC characterisation of the MZM

The MZ modulator DC characterisation is done by measuring the optical power coming out of the modulator as a function of the modulator reverse bias voltage, without applying RF signal on the modulator. In the following measurement laser channel 2 is presented. The laser is injected with a current of 68 mA, and emits a single-wavelength signal at 1559.28 nm. This laser light is guided to the on-chip modulator. A fibre-coupled power of 1 mW (0 dBm) is measured at the output facet of the modulator, when both of the modulator arms are grounded. Then one arm of the modulator remains grounded and the reverse bias voltage on the other arm increases from 0 V to 7 V with steps of 0.2 V. The power from the modulator output is measured by power meter and recorded in linear scale shown with symbols, as shown in Fig. 5.7, where the power is normalised with respect to the zero bias output. The figure shows the nonlinear behaviour of the modulator as discussed previously in 2.4.

In the modulator that exploits the MQW QCSE effect, the relation between index change Δn and bias voltage V_b is nonlinear. Assuming that this nonlinear relation is relevant only up to the second order, we model the relation between the phase
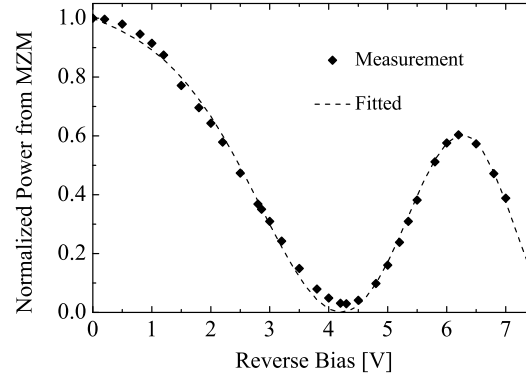
Figure 5.7: Normalized modulator output power versus reverse bias at wavelength of 1559.28 nm with the fitted curve. The symbols are the measured data and the dashed line indicates the fitted MZ modulator translation function based on Eq. 5.16 with $a = -0.25$, $b = 0.188$ and $c = 0.08$.

change and the bias voltage as a second order polynomial, $\Delta\varphi = aV_b + bV_b^2$, where a and b are the coefficients of the linear term and the quadratic term. Besides the nonlinear phase relation, there is also a nonlinear absorption effect as a function of bias voltage, which we model as $\exp(cV_b)$. Here c is the absorption coefficient due to the applied voltage. This parameter includes the information of the the optical confinement factor and the modulation length. So the transfer function of the output power of the MZ modulator using the QCSE, as a function of the reverse bias, is modeled as:

$$T_{\text{MZM}} = e^{cV_b}[1 + \cos(aV_b + bV_b^2)]/2 \tag{5.16}$$

As shown in Fig. 5.7, for this modulator, the voltage required for π phase change (V_π) is 4.1 V and the extinction ratio is 21 dB. Although the QCSE is wavelength dependent, within the 5 nm wavelength range that is relevant in this transmitter, V_π and the extinction ratio (ER_{DC}) for the four wavelength channels are quite similar ($V_\pi = 4.1 \pm 0.1$ V, $\text{ER}_{\text{DC}} = 20 \pm 1$ dB).

5.5 Bandwidth and link gain

The small-signal RF electrical-to-optical (EO) measurement setup is shown in Fig. 5.8. The laser is again injected with a current of 68 mA, and emits a single-wavelength signal at 1559.28 nm. The laser light is fed into the MZM. First one arm of the modulator is grounded, and the other arm is biased at the quadrature point
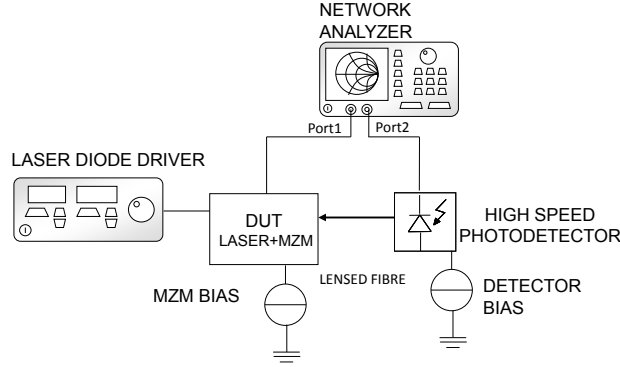
Figure 5.8: Schematic for the transmitter EO measurement setup.

of the modulator ($V_b = 2.8$ V); it is also connected to the RF signal from port 1 of the electrical network analyser (ENA), through the coaxial RF SMB on the PCB. The fibre-coupled modulated optical output is routed to a high-speed photodiode. The detected signal is sent back to port 2 of the ENA. Thus a microwave photonic link is built. During the measurement the input RF signal frequency is swept from 50 MHz to 10 GHz, with a power of -10 dBm. At the quadrature bias, the modulator optical output power is around -3 dBm in the fibre, an intrinsic analog photonic link gain (S_{21}) is measured around -45 dB up to 7 GHz as shown in Fig. 5.9. The MZM can have a bandwidth up to ~10 GHz, according to the platform data. Here the lower bandwidth would be due to the electronics of the sub-mount setup, e.g. the too long wire bond, or unmatched impedance. It is also observed from Fig. 5.9, that S_{11} goes higher than -10 dB below 7 GHz. This indicates that the high reflection already decreases the transmission of the power. The bandwidth is not limited by the bandwidth MZM itself, but is limited by the impedance mismatch from the sub-mount to the MZM arms.

To get a 3 dB higher link gain, a push-pull operation of the MZM has been implemented. The rate-race PCB of 1.5 GHz and 4.5 GHz are used in the measurement. The laser condition is same as for the single arm operation and both of the modulator arms are biased in such a way that the modulator output is at the quadrature point. Fig. 5.10 is measured by the ESA, with an RF output of -10 dBm. With the same optical power the link gain is constant at -42 ± 1 dB in the two measured frequency ranges 1.1 GHz to 1.9 GHz and 3.3 GHz to 5.3 GHz. So this transmitter can meet the required frequency specification of the smart antenna system, which will be operated at the frequency of 2 to 5 GHz. However, in a real system the push-pull driving circuit needs to be adapted to a broadband solution rather than the passive narrow-band rat-race coupler that was used in this experiment.
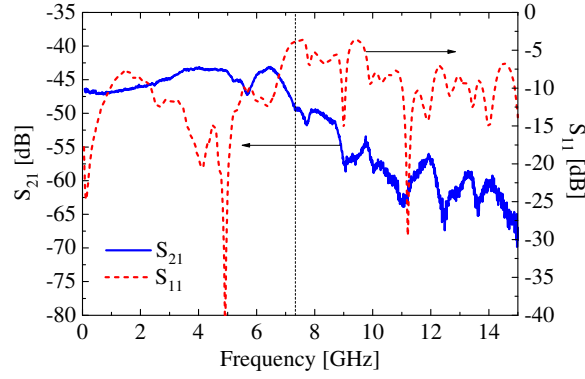
Figure 5.9: Result of the single arm EO measurement. S_{21} is the transmission coefficient of the network and here it is the link gain as a function of the frequency; S_{11} is the reflection coefficient, which describes the reflection from the modulator RF input back to the ENA.
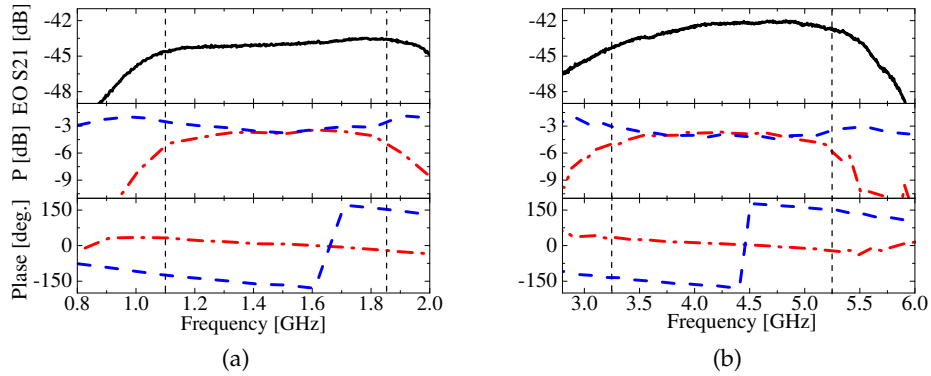
Figure 5.10: From top to bottom there are the intrinsic optical link gain, power coupling and phase coupling of two branches of the rat-race coupler as a function of input RF frequency, for two coupler PCBs at central frequency of (a) 1.5 GHz, and (b) 4.5 GHz. The vertical dotted lines indicate 1-dB bandwidth of the rat-race coupler. The loss is 0.7 dB and 0.9 dB for 1.5 GHz and 4.5 GHz coupler, respectively.
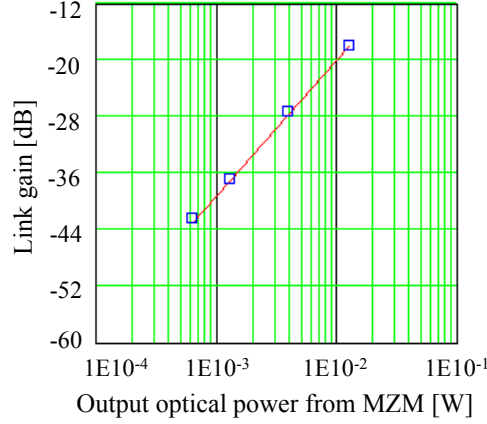
Figure 5.11: Link gain of the filter-feedback transmitter APL with a quadrature-biased MZM as a function of the optical output. The symbols indicate the measured points, the solid line is the calculated value.

The measured link gain of $-42\,\mathrm{dB}$ is rather low for a real application. In order to investigate how much the link gain can be improved by adding an SOA after the laser, an Erbium-doped fibre amplifier (EDFA) is added in between the output from the transmitter chip and the detector, to boost the output optical power. The link gain is recorded at an intrinsic optical output power of $-3\,\mathrm{dB}$ ($0.5\,\mathrm{mW}$), with the optical output power boosted to $1.5\,\mathrm{mW}$, $4\,\mathrm{mW}$ and $10.5\,\mathrm{mW}$ ($< 12\,\mathrm{dBm}$ which is limited by the detector). The link gains are plotted as symbols in Fig. 5.11, and they show a good agreement with the gain calculated by Eq. 5.4, which is plotted as the solid line. This shows that by adding an SOA, which could provide a gain around $15\,\mathrm{dB}$, the link with our transmitter can reach a link gain in the order of $-10\,\mathrm{dB}$.

5.6   Noise measurement

In sec. 5.2.2 we discussed the three dominant noise terms in the APLs. In this section once again, we investigate the noise figure of the APL formed by the filtered-feedback transmitter. The laser is injected with a current of $68\,\mathrm{mA}$, and emits a single-wavelength signal at $1559.28\,\mathrm{nm}$. The laser light is coupled to the fibre from the MZM output and fed to the faster photodetector (R2560A) from EMCORE. At the quadrature bias voltage the output optical power is $-3\,\mathrm{dB}$. Photocurrent on the detector is measured though a bias-T, and the high frequency fluctuation signal from the detector is sent to the ESA through a LNA. The LNA (NF $= 3\,\mathrm{dB}$, $G = 32\,\mathrm{dB}$) is used to increase the sensitivity of the ESA to the noise power. The bandwidth of the

ESA is set to $\Delta f = 10^5$Hz.

When measuring the relative intensity noise, as defined in Eq. 5.10, the optical power P_{Opt} is detected with a fast photodetector, and the optical power fluctuation $\Delta P(t)$ is transformed into an electrical power fluctuation which is measured with an electrical spectrum analyser (ESA). However, because the squared optical power is proportional to the detected electrical power, $p_{\text{O}}^2 \propto i^2 \propto p_{\text{E}}$, Eq. 5.10 can be rewritten as:

$$\text{rin} = \frac{p_L}{p_{\text{Eavg}}\Delta f} = \frac{p_{\text{tot}} - p_{\text{th}} - p_{\text{sh}}}{p_{\text{Eavg}}\Delta f}, \tag{5.17}$$

where p_{Eavg} is the average received electrical power from the photodetector. In the numerator, the laser intensity noise p_{L} is obtained by subtracting extra noise sources from the total noise p_{tot}. The thermal noise and shot noise can be measured separately.

Thermal noise p_{th} is measured by running the setup when the laser is turned off. Without optical power, only the thermal noise is measured on the ESA. This term includes the dark photocurrent of the detector and the thermal noise sources of the electronics (total background noise). The thermal noise was measured to be $P_{\text{th}}=-121.1$ dBm. When the laser is on, P_{tot} is measured as -120.5 dBm (the values are real value after considering 32 dB gain from LNA).

Although the shot noise can be calculated from the measured photocurrent when the laser is turned on, $p_{\text{sh}} = 2qI_{\text{ph}}R_L\Delta f$, the average electrical power can be calculated from the photocurrent I_{ph}, $P_{\text{Eavg}} = I_{\text{ph}}^2R_L$, the power of the laser coupled into the detector is too low to to get an accurate RIN measurement.

As $\Delta f = 10^{-5}$ Hz, the total noise of the link is $p_{\text{tot}}/\Delta f = -170.5$ dBm/Hz; using the link gain $g = -43$ dB, and at a temperature $T = 290$ K, with Eq. 5.13, we calculate the noise figure of the link as

$$\text{NF} = 10\log_{10}\left(\frac{p_{\text{tot}}}{gkT\Delta f}\right) = 46.5\,\text{dB} \tag{5.18}$$

Here the high noise figure is mainly due to the low optical power. The link noise figure will improve with optical power, because the signal power increases quadratically with the optical power, whereas the the shot noise increases only linearly. However, the benefit of increasing this optical power is lost if RIN is the dominant source. It again shows that adding amplifiers to increase the optical output power needs to be done in order to have a better performance of the link.
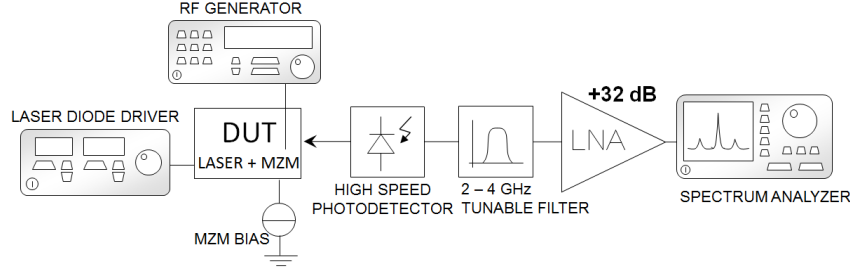
Figure 5.12: Schematic of the measurement setup for 2nd and 3rd order harmonic generated in the modulators. The tunable passband filter is to filter out the high power fundamental signal to assure that the distortion which is measured only from modulator rather than from the amplifier or the spectrum analyser due to an amplified high-power fundamental signal.

5.7   Distortion measurement

For analog modulation, The purpose of this filtera high degree of linearity is desirable in order to maintain the dynamic range of a photonic link. The distortion measurement of the link is done on this filtered-feedback transmitter link with a setup as illustrated schematically in Fig. 5.12. The tunable passband filter has a bandwidth of 20 MHz, and it is tunable in the frequency range from 2 GHz to 4 GHz. The purpose of this filter is to remove the high power fundamental signal, in order to avoid the nonlinear distortion from the amplifier or spectrum analyser excited by the fundamental signal. In this way, the distortion is measured only from the modulator.

In the filtered-feedback transmitter discussed in this thesis, the Mach-Zehnder modulator exhibits the nonlinear transfer characteristics shown in Sec. 5.4. The output optical power of the MZM is

$$P_{\text{out}}(V_{\text{b}}) = P_{\text{in}} T_{\text{MZM}}(V_{\text{b}}) = P_{\text{in}} e^{cV_{\text{b}}} [1 + \cos(aV_{\text{b}} + bV_{\text{b}}^2)]/2 \qquad (5.19)$$

Taking the first, second and third derivatives of Eq. 5.19, the bias dependencies of the gain (fundamental), second and third order harmonic distortions are obtained, respectively [114]:

$$P_{\text{fund}}(V_{\text{b}}) = \frac{\partial P_{\text{out}}(V_{\text{b}})}{\partial V_{\text{b}}} \qquad (5.20)$$

$$P_{\text{HD}_2}(V_{\text{b}}) = \frac{\partial^2 P_{\text{out}}(V_{\text{b}})}{\partial V_{\text{b}}^2} \qquad (5.21)$$

$$P_{\text{HD}_3}(V_{\text{b}}) = \frac{\partial^3 P_{\text{out}}(V_{\text{b}})}{\partial V_{\text{b}}^3} \qquad (5.22)$$
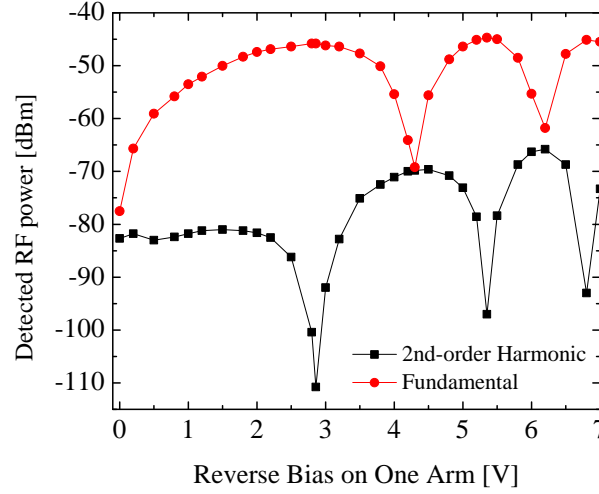
Figure 5.13: Plots of the fundamental and second-order hamonic distortion versus the Mach-Zehnder bias voltage (one arm is biased, and the other arm is grounded).

Fig. 5.13 plots the fundamental signal and the second order harmonic distortion (HD$_2$) measured as a function of modulator bias voltage. The power of HD$_3$ is too small to be detected at most of the bias points.

An RF signal with a frequency of 1.2 GHz and a power of 0 dBm is supplied from the signal generator to the RF input port of the MZM. The modulator bias voltage varies from 0 to 7 V with steps of 0.2 V. In this measurement the link is not using the +32 dB low noise amplifier shown in the setup (Fig. 5.12). Comparing Fig. 5.13 with Fig. 5.7 shows that the power of the fundamental signal and HD$_2$ indeed have the shapes as the first and second derivatives of the output optical power. At V_π, where $V_b = 4.1$ V, the link has the lowest gain and the highest HD$_2$. At the quadrature bias point, where the power transfer function is most linear, the gain reaches the maximum value, and the HD$_2$ is minimized. However, according to Eq. 5.22, HD$_3$ will reach maximum when HD$_2$ is minimized. The fundamental signal and the HD$_3$ are both odd-order derivatives of the power transfer function. Therefore, in a standard MZM, it is possible use the bias point to eliminate the second-order distortion but not the third-order distortion.

At a bias voltage of $V_b = 2.8$ V, the HD$_2$ and HD$_3$ are measured as a function of RF input power. In this measurement, the setup in Fig 5.12 is used with the +32 dB low noise amplifier amplifier (LNA) from Miteq, to be able to detect also the HD$_3$ signal. The RF input signal increases from 0 dBm to 9 dBm with a frequency of 1.2 GHz, while the power of the HD$_2$ and HD$_3$ measured on the spectrum analyser is recor-
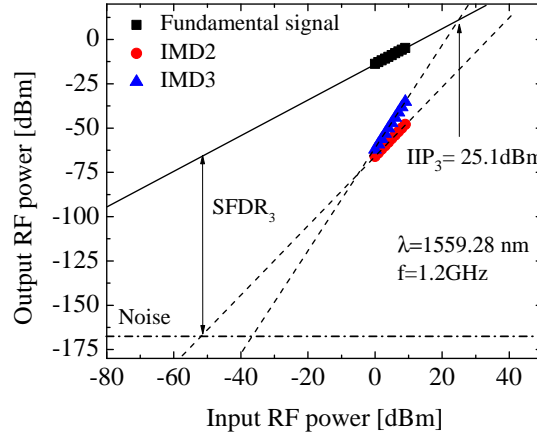
Figure 5.14: The SFDR measurement of the APL form with the transmitter device.

ded. According to Eq. 5.14 and Eq. 5.15 the power of IMD_2 and IMD_3 can be calculated. The IMD measurement results for are plotted in Fig. 5.14. The input power, where the IMD power is equal to the fundamental signal power, is the input interception point (IIP). The IIP_3 is 25.1 ± 0.5 dBm and the $SFDR_3$ is 105 dB·Hz$^{2/3}$.

5.8 Crosstalk measurement

The RF-crosstalk is an important specification in the multi-channel transmitter. In the transmitter circuit, the distance between two adjacent modulators is $350\,\mu$m. To investigate the RF-crosstalk, we applied an RF signal to one modulator, and recorded the light signal from the adjacent channel and from the 2nd adjacent channel on the ENA. The difference in Electro-Optical (EO) transmission between the channel with RF input and the neighbouring channels is the crosstalk. The neighbouring channels are without RF input, but are biased at the quadrature point. In order to have the EO transmission of adjacent channels above the noise level, the optical power is boosted by an EDFA to 6 dBm before feeding the signals to the detector.

The measurement results are presented in Fig. 5.15. The crosstalk performance for all the channels is quite comparable. The crosstalk to an adjacent channel is less than −30 dB and to a 2nd adjacent channel it is less than −40 dB for the frequency range from 1 GHz to 2 GHz. For higher frequencies clearly the crosstalk increases, and reaching −20 dB for the adjacent channel, and −30 dB for the 2nd adjacent channel at 5.2 GHz.

To further investigate the crosstalk, two different frequencies are applied to two
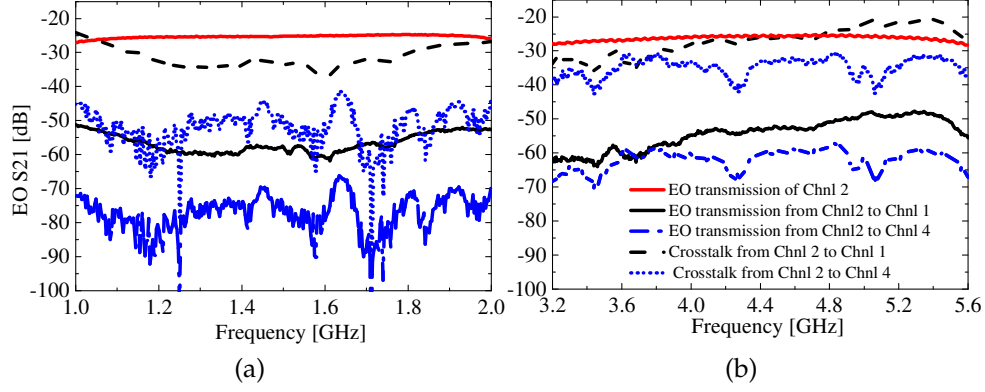
Figure 5.15: EO transmission of channel 2 with RF input, and its adjacent and 2nd adjacent channels (solid line and dash-dot line); The crosstalk from channel 2 to channel 1 and from channel 2 to channel 4 are plotted in dashed line and dotted line, respectively, for PCBs with a central frequency of (a) 1.5 GHz, and (b) 4.5 GHz.
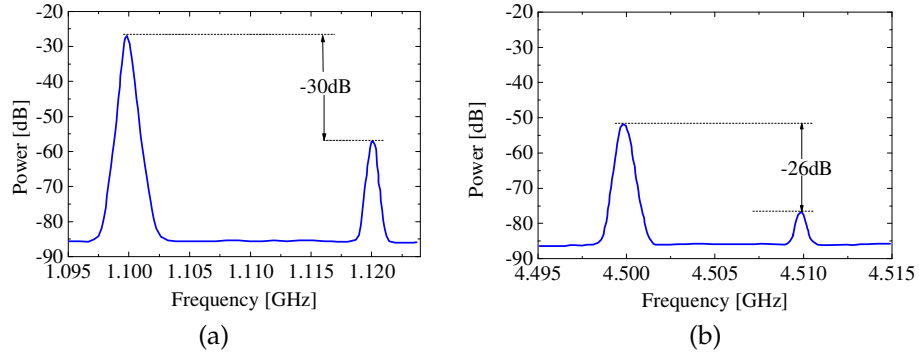
Figure 5.16: Electrical spectrum detected from (a) channel 1 boosted to 6 dBm, when 1.1 GHz, and 1.12 GHz, 0 dBm RF signals are applied on channel 1 and channel 2, respectively, from the rat-race coupler with central frequency of 1.5 GHz; (b) channel 1 with an optical output power of -4.5 dBm when two RF signals with a -10 dBm power level and a frequency of 4.5 GHz and 4.51 GHz on channel 1 and channel 2 respectively.

neighbouring modulators by two RF generators, and the modulated light from one channel is measured by the ESA connected with the detector.A clear RF signal at the frequency of the adjacent channel can be observed from the spectrum (Fig. 5.16). The power difference between the detected RF signal has a good agreement with the previous EO transmission crosstalk measurement, both at different optical power levels and at different RF powers.

5.9   Summary and discussion

This chapter introduced the design of a filtered-feedback transmitter and explored the performance of this transmitter in terms of using it in an analog link. The transmitter chip is mounted on a customized sub-mount for different characterisations. First, the DC measurement of the Mach-Zehnder modulator is carried out where $V_\pi = 4.1 \pm 0.1$ V and $ER_{DC} = 20 \pm 1$ dB are found. Furthermore, the nonlinear transfer function of MZM is investigated. Then the bandwidth of transmitter is measured with an RF signal on single arm, and with an RF push-pull signal on both arms. The bandwidth is limited at 7 GHz, due to the impedance mismatch between the modulator and the sub-mount. The bandwidth of the transmitter can fulfil the requirement of the smart antenna application operating at a frequency range of 2-5 GHz. To go for a higher modulation frequency, up to 10 GHz, the electronic board and matching impedance should be carefully designed. An intrinsic link gain of -42 dB and the noise figure of 46.5 dB, are not that satisfying. Both facts attribute to the too low output optical power. In the next design, spot-size convertor could be added to minimize the fibre coupling loss and SOAs need to be add to boost the laser power from each channel, in order increase the output power in turn improve the link gain and the noise figure. For the simultaneously multi-channel operation, the crosstalk from adjacent channels is also investigated and it is below -20 dB upto 5 GHz. For higher frequency low cross talk, the long wire bond is not a optimal solution, and flip boding and advanced RF connectors are prefered. The distance between the modulators in the array should be also optimized with respect to the cross talk and the compactness.

Appendix

Nonlinear distortion

A device could have a perfectly linear power transfer function over some range of inputs. But if the magnitude of the modulation exceeds the linear range of the device, it will produce distortion. There is no "distortion" if no new frequency is created. Consider the transfer function of a MZ modulator that exploits a linear EO effect and which is biased at the quadrature point with a sine wave RF input signal $\sin(\omega t)$,

detected by a distortionless photodiode of responsivity r_{PD}. The time dependent detector photocurrent is then given by:

$$i_d(t) = r_{PD}P_i\cos\left(\frac{\pi v_m\sin(\omega t)}{V_\pi}\right).$$

It will show that for a single frequency at the input, the output current will have the more spectral components at 3ω, 5ω, 7ω, $\ldots$ with different amplitudes. For small-signals, the most common way to approximate the non-linear transfer function is by using the Taylor series [117]. A function $f(x)$ can be expressed as a infinite sum of derivatives of the function with respect to x evaluated at a given point, a[114]:

$$f(x) = \sum_{k=0}^{\infty} \frac{(x - x_0)^k}{k!} \left(\frac{d^k f}{dx^k}\right)_{x=x_0} = \sum_{k=0}^{\infty} a_k(x - x_0)^k, \tag{5.23}$$

where

$$a_k = \frac{1}{k!} \left(\frac{d^k f}{dx^k}\right)_{x=a}$$

The Taylor series provides another way to distinguish linear and non-linear devices. For a linear device, all the derivatives of its transfer function are zero, except for the first order one.

Here it is assumed that the APL nonlinearity is dominated by the response of the modulator, and that the other devices such as the photodetector are strictly linear in the power level considered. Moreover the nonlinearity is limited to static weak nonlinearities, which means the nonlinear characteristic of the modulator can be described as Eq. 5.23. When the input signal has the form of $x(t) = x_0 + A\cos(\omega t)$, where ω is the angular frequency of the modulating signal, A is the amplitude and x_0 is the bias voltage. Substituting this expression into the 5.23 up to the 3rd order, the modulator response is expressed as:

$$\begin{aligned} f(t) &\approx a_0 + \tfrac{1}{2}a_2 A^2 + \left(a_1 A + \tfrac{3}{4}a_3 A^3\right)\cos(\omega t) + \\ &\quad \tfrac{1}{2}a_2 A^2\cos(2\omega t) + \tfrac{1}{4}a_3 A^3\cos(3\omega t) \end{aligned} \tag{5.24}$$

It consists of a DC component which is independent of frequency, the signal component with frequency of ω, and spurious component at frequency of 2ω and 3ω. The spurious frequencies are an integer times ω, which are known as harmonic distortion (HDs). However, a more common RF practice is often to use two equal-amplitude sinusoids for characterising distortion: the input signal has the form of $x(t) = x_0 + A\left[\cos(\omega_1 t) + \cos(\omega_2 t)\right]$. Substituting this input into Eq. 5.23 up to

the 3rd-order, a similar form of Eq. 5.24 is obtained using the trigonometric relation $\cos \alpha \cos \beta = 1/2 \left[\cos (\alpha - \beta) + \cos (\alpha + \beta) \right]$

$$
\begin{aligned}
f(t) \quad \approx \quad & a_0 + a_2 A^2 + \left(a_1 A + \tfrac{9}{4} a_3 A^3 \right) \left\{ \cos(\omega_1 t) + \cos(\omega_2 t) \right\} \\
& + \tfrac{1}{2} a_2 A^2 \left\{ \cos(2\omega_1 t) + \cos(2\omega_2 t) \right\} \\
& + \tfrac{1}{4} a_3 A^3 \left\{ \cos(3\omega_1 t) + \cos(3\omega_2 t) \right\} \\
& + a_2 A^2 \left\{ \cos \left[(\omega_1 - \omega_2) t \right] + \cos \left[(\omega_1 + \omega_2) t \right] \right\} \\
& + \tfrac{3}{4} a_3 A^3 \left\{ \cos \left[(2\omega_1 - \omega_2) t \right] + \cos \left[(2\omega_2 - \omega_1) t \right] \right. \\
& \qquad \left. + \cos \left[(2\omega_1 + \omega_2) t \right] + \cos \left[(2\omega_2 + \omega_1) t \right] \right\}
\end{aligned} \tag{5.25}
$$

Here we limited the order to 3. It is evident that not only the harmonic terms for each frequency are generated but additionally spurious components with two frequencies also appear. They are referred to as the intermodulation terms. The 2nd-order intermodulation distortion terms (IMD$_2$) occur at the sum and the difference of the modulating frequencies, while the 3rd-order intermodulation terms (IMD$_3$) occur at the sum and the difference of twice of one frequency with the other frequency. The components and coefficients listed in table 5.1 on page 75.

Chapter 6

Conclusions and recommendations

6.1 Conclusions

The main objective of this research is to demonstrate a monolithically integrated multi-wavelength transmitter. This work has achieved significant milestones in realizing an integrated photonic transmitter circuit with four channels, high wavelength stability and narrow linewidth.

The development of the multi-wavelength transmitter (MWT) has been carried out in the framework of an analog application operating in the telecom-wavelength range. This led to a series of designs for (1) a novel Fabry-Pérot laser with on-chip broadband multi-mode-interference reflectors (MIRs), (2) the multi-wavelength laser (MWL) and (3) the multi-wavelength laser monolithically integrated with Mach-Zehnder modulators (MZMs). The multi-wavelength lasers makes use of a filtered-feedback design and demonstrates successful simultaneous operation on four channels. The integrated MZM with its corresponding electronics achieves a bandwidth of 7 GHz. With this work, a demonstration has been given not only of the feasibility of the design, but also of the great potential for implementation in real systems. The filtered-feedback multi-wavelength transmitter here developed can provide a much more compact solution for use in photonic analog applications, compared to traditional optical transmitters based on discrete laser and modulator components. And of course, the application is not only limited to analog links: this multi-wavelength transmitter can be a good transmitter in digital systems as well. The filtered-feedback MWL is therefore a good building block for any application that needs a multi-wavelength narrow-linewidth source.

We now summarize the highlights of this research.

Generic integration

The generic-integration platform is explored during the process of realizing the multi-wavelength transmitter described in this thesis. The FP lasers with MIRs were designed in the first trial run of an industrial generic InP-based integration process, and fabricated in a multi-project wafer run. In this first trial run, the generic platform started with the active-passive integration. Then in the following trial runs, more building blocks such as phase shifters became available, which have been implemented in our transmitter design. The successful realisation of our transmitter device also demonstrates the success of the generic-integration concept.

Filtered feedback

Compared with the more traditional AWG-based lasers, the innovation of our multi-wavelength laser is to use feedback from an AWG to select the desired lasing mode. Instead of using the AWG as the wavelength filter inside the main laser cavity, it is now used outside the main cavity. This configuration eliminates the complexity introduced by an intra-cavity AWG, which causes extra loss and possible reflections inside the main cavity. The filtered-feedback concept reduces the threshold current, reduces the linewidth of the laser and also enables easier integration with other devices on the chip.

FP laser with MIR reflectors

In order to realize the filtered-feedback structure of the laser, a novel type of FP laser using multi-mode-interference reflectors has been developed in this work. The MIR is an on-chip reflector with a broadband reflection range which can be fabricated within a standard active-passive integration process. Due to its simple fabrication and by enabling accurate control of the cavity dimension, the FP laser with MIRs will become very a promising building block for large-scale photonic integration.

Linewidth

The linewidth for our filtered-feedback laser is theoretically found to be smaller than for a solitary laser without feedback by a factor of ~4 to 5 under a proper feedback phase. It has indeed been observed that the filtered-feedback laser developed in this thesis has a quite narrow linewidth ($< 150\,\text{kHz}$) compared with usual DBR and DFB lasers (~1 MHz).

Feedback stability

For a laser with feedback configuration, the introduction of delayed optical feedback may cause instabilities to the laser like the undamping of relaxation oscillations and coherence collapse. In this work, a theoretical and experimental investigation of the stability of the filtered-feedback with an electrically controlled feedback phase has been carried out. The good agreement between the experimental results of the laser optical power spectrum and noise power spectrum, on the one hand, and the theoretical study on the other hand, demonstrate our understanding of the stability of the feedback laser.

Simultaneous lasing and transmitting

An important general requirement for the multi-wavelength device is that all of the wavelength channels should be working stably at the same time. The four-channel laser presented here satisfies this requirement. This laser can operate at the four channels simultaneously, with an accurate wavelength spacing which is defined by the channel spacing designed for the AWG, with an SMSR better than 40 dB. The transmitter made with a multi-wavelength laser and modulators also shows a good simultaneous operation with RF cross-talk lower than -20 dB up to a signal frequency of 5 GHz.

6.2   Recommendations

While the work in this dissertation has yielded the proof-of-concept of the filtered-feedback multi-wavelength transmitter, there are always improvements that could be done to enhance the performance further.

1. In a real system, transmitters with more channels and multiplexed output signal are definitely required. Therefore, the four-channel transmitter needs to be scaled to a larger number of channels by using an AWG with more channels. In this case, an additional AWG, or, in a different configuration, the same AWG can be used to multiplex the modulated signals from all the channels, as discussed in Chapter 2.

2. When we are moving towards high-density photonic integration with more channels working at higher frequency, the crosstalk becomes a significant issue. The distance between the modulators needs to be carefully designed in relation to the working frequency to optimize the trade-off between the crosstalk and the distance between the channels.

3. With higher frequency, the driving circuit and sub-mount of the transmitter need to be as close as possible to the modulator impedance to avoid reflection. Also a flip-chip bonding technique [118] is preferred to increase the high-frequency performance of the transmitter.

4. As known from Chapter 5, the link gain depends strongly on the optical power. The optical power is always demanded to be higher. Increase of the optical power can be achieved by adding an SOA in each channel between the FP laser and the modulator. The SOA boosts the laser output power first, before modulation. Moreover, by reducing the loss of MIR and adjusting the reflection and transmission of the two-port MIR and the one-port common MIR the laser output power could also be improved.

5. In this thesis work, all optical signals on the chip are coupled by a lensed fibre from the deeply-etched waveguide. The fibre-chip coupling loss is dominating the optical loss of the whole photonic link. The use of a spot-size converter can reduce the coupling loss while simultaneously improving the alignment tolerances. The spot size has to be designed to match that of the pig-tail fibre connection. Alternatively, the chip can be glued to an interposer chip with a matched spot-size and which also provides low-loss coupling to the fibre.

Summary

Integrated Multi-Wavelength Transmitter using Filtered-Feedback

The main objective of this research is to demonstrate a monolithically integrated multi-wavelength transmitter. This work has achieved significant milestones in realising the integrated photonic transmitter circuit with more channels, high wavelength stability and narrow linewidth.

The development of the multi-wavelength transmitter has been carried out in the framework of an analog application operating in the telecom-wavelength range. This led to a series of designs for (1) a novel Fabry-Pérot laser with on-chip broadband multi-mode-interference reflectors, (2) the multi-wavelength laser and (3) the multi-wavelength laser monolithically integrated with Mach-Zehnder modulators.

Compared with the more traditional AWG-based lasers, the innovation of our multi-wavelength laser is to use the feedback from the AWG to select the desired lasing mode. Instead of using the AWG as the wavelength filter inside the main laser cavity, it is now used outside the main cavity. This configuration eliminates the complexity introduced by an intra-cavity AWG, which causes extra loss and possible reflections inside the main cavity. The filtered-feedback concept reduces the threshold current, reduces the linewidth of the laser and also enables easier integration with other devices, such as modulators to form transmitters, on the chip.

In order to realize the filtered-feedback structure of the laser, a novel type of FP laser using multi-mode-interference reflectors (MIRs) has been developed in this work. The MIR is an on-chip reflector with a broadband reflection range which can be fabricated within a standard active-passive integration process. These FP lasers with MIRs are among the first integrated photonic devices that were fabricated using an industrial generic integration technology. They are proven to be versatile building blocks for large-scale integrated photonic circuits.

By using the FP lasers with MIRs, the world's first filtered-feedback multi-wavelength laser was designed. A four-channel monolithically integrated filtered-feedback laser has been successfully demonstrated with the four channels operating simultaneously. The lasers show accurate channel spacing which is defined by the channel spacing designed for the AWG, high sidemode suppression ratio (>40 dB), low threshold current (<16 mA) and narrow linewidth (<150 kHz). For a laser with feedback configuration, the introduction of delayed optical feedback may cause instabilities to the laser like the undamping of relaxation oscillations and coherence collapse. In this work, stability of the filtered-feedback laser was investigated as well. The theoretical and experimental investigation of the stability of the filtered-feedback with an electrically controlled feedback phase has been carried out. The good agreement between the experimental results of the laser optical power spectrum and noise power spectrum, on the one hand, and the theoretical study on the other hand, demonstrate our understanding of the stability of the feedback laser.

Based on the good performance of the filtered-feedback multi-wavelength laser, the integrated multi-wavelength transmitter was further developed. An array of Mach-Zehnder modulators was connected to each laser channel respectively to form a multi-wavelength transmitter. The DC performance of the filtered-feedback laser with Mach-Zehnder modulators was presented and the nonlinear transfer function of MQW based MZM was investigated. The modulator shows a $V_\pi = 4.1 \pm 0.1$ V and $ER_{DC} = 20 \pm 1$ dB. Furthermore, the performance of this transmitter in terms of using it in an analog link was explored. The transmitter can fulfill the requirement of smart antenna application operating at a frequency range of 2-5 GHz with an intrinsic link gain of -42 dB. As a multi-channel device, the transmitter also shows a good simultaneous operation with RF cross-talk lower than -20 dB up to a signal frequency of 5 GHz. With this work, a demonstration has been given not only of the feasibility of the design, but also of the great potential for implementation in real systems.

The filtered-feedback multi-wavelength transmitter here developed can provide a much more compact solution for use in photonic analog applications, compared to traditional optical transmitters based on discrete laser and modulator components. And of course, the application is not only limited to analog links, this multi-wavelength transmitter can be a good transmitter in digital systems as well. Furthermore, the filtered-feedback MWL is also a good building block for any application that needs a multi-wavelength narrow-linewidth source.

List of publications

International Journals

- J. Zhao, K. Dijkstra, M.J. Wale, P. Maat, M.K. Smit, and X.J.M. Leijtens, "Filtered-feedback Laser Based Multi-wavelength Analog Optical Transmitter", in preparation for submission to *IEEE Photonics Technology Letters*.

- J. Zhao, D. Lenstra, R.M. Lemos Alvares Dos Santos, M.J. Wale, M.K. Smit, and X.J.M. Leijtens, "Stability of a monolithic integrated filtered-feedback laser", *Optics Express*, 20(26), B270-B278, (2012).

- J. Zhao, D. Lenstra, R.M. Lemos Alvares Dos Santos, M.J. Wale, M.K. Smit, and X.J.M. Leijtens, "Feedback phase influence on an integrated filtered-feedback laser". *IEEE Photonics Technology Letters*, 24(23), 2195-2107, (2012).

- J. van Gurp, M. Tichem, U. Staufer, and J. Zhao, "Passive Photonic Alignment with Sub-micrometer Repeatability and Accuracy", accepted in *IEEE Transactions on Components, Packaging and Manufacturing Technology*, (2013).

International Conference

- J. Zhao, D. Lenstra, R. Santos, M.J. Wale, M.K. Smit, and X.J.M. Leijtens, "Feedback Phase Influence on an Integrated filtered-feedback laser", *Proc. European Conference of Optical Communication (ECOC 2012)*, 17 - 19 September 2012, Amsterdam, the Netherlands.

- J. Zhao, K. Dijkstra, M.J. Wale, P. Maat, M.K. Smit, and X.J.M. Leijtens, "Monolithically integrated filtered-feedback multi-wavelength laser with Mach-Zehnder modulators", *Proc. 16th European Conference of Integrated Optic and technical exhibition 2012 (ECIO 2012)*, 18-20 April 2012, Barcelona, Spain.

- J. Zhao, P.J. Williams, M.K. Smit, and X.J.M. Leijtens, "Monolithic Integrated Filtered-feedback Multi-wavelength Laser", *Proc. Optical Fibre Communication Conference (OFC 2012)*, 4-8 March 2012, Los Angeles, California, US.

- J. Zhao, P.J. Williams, M.K. Smit, and X.J.M. Leijtens, "On-chip laser with multi-mode-interference reflectors realized in a generic integration platform" (invited), *Proc. 23rd International Conference on Indium Phosphide and Related Materials (IPRM 2011)*, 22-26 May 2011, Berlin, Germany.

- J. Zhao, E. Kleijn, M.K. Smit, P.J. Williams, I. Knight, M.J. Wale, and X.J.M. Leijtens, "Novel lasers using multi-mode-interference reflector", *Proc. Information Photonics (IP), 2011 ICO International Conference*, 18-20 May 2011, Ottawa, Canada.

- D. Lenstra, J. Zhao, R. Santos, M.K. Smit, and X.J.M. Leijtens, "Relaxation Oscillation Dynamics in Monolithic Integrated Diode Lasers", *Proc. the 38th European Semiconductor Laser Workshop (ESLW)*, 21-22 September 2012, Brussels, Belgium.

- T. Spuesens, L. Liu, D. Vermeulen, J. Zhao, P. Rojo Romeo, P. Regreny, L. Grenouillet, J. M. Fedeli, and D. van Thourhout, "Integration of photodetectors with lasers for optical interconnects using 200 mm waferscale III-V/SOI technology", *Proc. Optical Fibre Communication Conference (OFC 2011)*, 8-10 March 2011, Los Angeles, California, US.

Local Conferences

- J. Zhao, K. Dijkstra, M. J. Wale, P. Maat, M.K. Smit, and X.J.M. Leijtens, "Filtered-feedback Laser Based Multi-wavelength Transmitter", *Proc. the 16th Annual Symposium of the IEEE Photonics Benelux Chapter*, 29-30 November 2012, Mons, Belgium.

- J. Zhao, P.J. Williams, M.K. Smit, and X.J.M. Leijtens, "Multi-wavelength Laser Based on Filtered-feedback", *Proc. the 16th Annual Symposium of the IEEE Photonics Benelux Chapter*, 1-2 December 2011, Gent, Belgium.

- J. Zhao, E. Kleijn, M.K. Smit, and X.J.M. Leijtens, "Design of multi-wavelength transmitters using on-chip MMI reflectors", *Proc. the 15th Annual Symposium of the IEEE Photonics Benelux Chapter*, 18-19 November 2010, Delft, The Netherlands.

- J. Zhao, X.J.M. Leijtens, B. Docter, and M.K. Smit, "Integrated multi-wavelength lasers: a design study", *Proc. the 14th Annual Symposium of the IEEE Photonics Benelux Chapte*r, 5-6 November 2009, Brussels, Belgium.

Acknowledgement

Here I am in the most pleasant part of my thesis writing. I planned to write the acknowledgement part in the end of my writing so that I can feel I am almost done, and this is the part where I can look back into the exciting PhD ride and recollect all the good old days. I wish to thank each and every one by name who were supportive during this 4 year journey, but this would lead to a new thesis book. So I am going to thank only the dearest individuals in this page.

First and foremost I would like to thank Prof. Meint Smit for giving me the opportunity to be a part of one of the most prestigious group in the field of photonics integration. I would like to express my special thanks to my PhD committee members for reviewing my thesis, and providing their constructive comments.

I can't even begin to describe how deeply grateful I am to Dr. Xaveer Leijtens for patiently supervising, guiding and helping me for these more than 4 years. I would like to say "thank you boss". I feel very fortunate to have Prof. Daan Lenstra as my co-promoter in my third year, for his help and advices concerning the theory of filtered feedback in lasers, and for the time he spent on motivating me, correcting and reviewing my thesis work.

Special thanks to Mike for providing me the opportunity of internship in Oclaro, and for his advices on my work. I also want to thank Dave who has always been willing to offer support in the research. The transmitter measurement would not have been possible without the collaboration with Astron photonic team. Peter and Klaas' help with sub mount design, along with their RF measurement experience, made my life much easier.

I would like acknowledge Erwin for the valuable discussions and lab guidance, and Jos for the pleasant and "debatable" conversations :P. I am thankful to Jolanda, Jose, and Susan for taking care of all the administrative hassles. My sincere thanks to the old group members, Fouad for the help inside and outside the cleanroom and his encouragement even after leaving the group, Hans, Siang Youcai and for their help, encouragement and concern.

Our cleanroom staff is first-rate. I greatly appreciate Barry's help for cleaving and gluing my chips. I still remember the you once got my chip ready on the rainy

Friday late evening. Thanks go out to Huub, Tjibbe, Jeroen, Erik-Jan, for teaching and helping me with practical work in cleanroom, and also for teasing me :P

I am also indebted to the past PhDs of the group. Martijn, you are the OLA mentor for me, who showed me to the way to squeeze the result from chips. Ling, Pietro, you shared a lot with me on your working and life experience, which were really helpful for me when I just stated. Boudewijn, Bauke, Milan, thank you for all the interesting discussions. Jan Hendrik, Luc and Ronald, thank you for your help not only on my Phd work, but also on my job selection.

Here comes our X-men team: Kasia, Emil, Staszek, Deepak, I really enjoyed the time in our happy transparent aquarium office, and they are all my nice memories. Thanks to Rui, the co-author who helped me with the measurements and reviewed my papers.

Ray, Yuqing, Saeed we are from the same batch. But I am the last one for the defence. Thank you for helping me (bothered so much by me :P) and sharing the experience. Saeed, I'm so happy to be your "roomie", and thanks a lot for your inspiration and help.

I wish to thank Manuela, Vala and Kasia for the "ladies nights", climbing and all other happy hours we had together. The activities should definitely continue. Josselin, Dima, Elton, Antonio, Srivathsa, Domenico, it has been my pleasure to work with you. Good luck with the work~ Sylwester, Hadi, Giovanni, Dominik, the postdoc gang, thank you for helping me in the lab and the discussions. To the new colleagues in our group, enjoy the journey, and all the very best with your research projects~

I'm grateful for ECO group colleague Piet for his nice advice on my design as well as measurement. I would like also to thank Oded, Jim, Haoshuo, Pang and Jun for their equipment support on my measurement. Thank Pinxiang, Yan, Abhi, Nicos for the nice trips and dinners we had together.

Thank my friends within and outside the Netherlands: Dier, minmin, Xiaoying (outside NL), lala, Xu, Alex, Sumy, Noémie, Xianxian, Xue (inside NL) for their caring, company, and joyful gatherings. Special thank to sister Liang and neighbour Raghu, for being there for me during my happy and frustrating moments.

Last, but certainly not least (in fact, most importantly), I wish to express my gratitude and thanks to my parents who let me choose my path in life and supported whichever decision I made and to my grandparents for their endless love and support to me.

Curriculum Vitae

Jing Zhao was born in Xi'an, China in 1983. In 2005, she obtained her B.Sc. degree in Electrical Engineering from Xiamen University (Xiamen, China). She received the M.Sc. degree in Electrical Engineering from the Linköping University (Linköping, Sweden) in 2008. During her master degree, she did her master thesis work at NXP semiconductor (Eindhoven, the Netherlands) on the design and characterisation of galvanic piezoelectric MEMS (Micro-electro-mechanical system) switches.

From 2008 to 2012 she has been working towards the Ph.D. degree in the Photonic Integration (formerly Opto-Electronic Devices) group of the COBRA Research Institute. Supervised by Dr. X. Leijtens, Prof. Dr. D. Lenstra and Prof. Dr. M.K. Smit, she worked on the monolithically integrated multi-wavelength transmitter using Filtered-feedback. During her PhD project she spent 4 months at Oclaro (Caswell, UK) to work on FP lasers with on-chip reflectors in generic integration technology.

From December 2012, Jing Zhao started working in ASML (Veldhoven, the Netherlands) in EUV Development & Engineering department as a design engineer.

References

[1] D. Welch, F. Kish, S. Melle, R. Nagarajan, M. Kato, C. Joyner, J. Pleumeekers, R. Schneider Jr., J. Bäck, A. Dentai, V. Dominic, P. Evans, M. Kauffman, D. Lambert, S. Hurtt, A. Mathur, M. Mitchell, M. Missey, S. Murthy, A. Nilsson, R. Salvatore, M. Van Leeuwen, J. Webjorn, M. Z. S. Grubb, D. Perkins, M. Reffle, and D. Mehuys, "Large-scale InP photonic integrated circuits: enabling efficient scaling of optical transport networks," *IEEE J. Sel. Topics in Quantum Electron.*, vol. 13, pp. 22–31, Jan./Feb. 2007.

[2] S. E. Miller, "Integrated optics: An introduction," *Bell Syst. Tech. J.*, vol. 48, pp. 2059–2069, Sept. 1969.

[3] B. Verbeek, E. Teunissen, and H. van den Vlekkert, eds., *MEMPHIS, Merging Electrics and Micro and nano Photonics in Integrated System*. The MEMPHIS consortium, 1 ed., 2012. ISBN : 978-94-90314-14-9.

[4] M. Burla, C. Roeloffzen, L. Zhuang, D. Marpaung, R. Khan, P. Maat, K. Dijkstra, A. Leinse, M. Hoekman, and R. Heideman, "System integration and radiation pattern measurements of a phased array antenna employing an integrated photonic beamformer for radio astronomy applications," *Appl. Opt.*, vol. 51, p. 789, Mar. 2012. doi:10.1364/AO.51.000789.

[5] L. Zhuang, C. G. H. Roeloffzen, R. Heideman, A. Borreman, A. Meijerink, and W. van Etten, "Single-chip ring resonator-based 1×8 optical beam forming network in CMOS-compatible waveguide technology," *IEEE Photon. Technol. Lett.*, vol. 19, no. 15, pp. 1130–1132, 2007.

[6] M. Burla, "Research in Optical Beamforming at UT-TE," *Presentation in MEMPHIS General Assembly*.

[7] M. Burla, M. Khan, L. Zhuang, and C. Roeloffzen, "Multiwavelength optical beam forming network with ring resonator-based binary-tree architecture for broadband phased array antenna systems," in *Proc. IEEE/LEOS Symposium (Benelux Chapter)*, pp. 99–102, Enschede, The Netherlands, Nov. 2008.

[8] K. Sato and K. Asatani, "Analogue baseband TV transmission experiments using semiconductor laser diodes," *Electron. Lett.*, vol. 15, no. 24, pp. 794–795, 1979.

[9] T. D. Michaelis, "Laser diode evaluation for optical analog link," *IEEE Transactions on Cable Television*, vol. CATV-4, no. 1, pp. 30–42, 1979.

[10] H. Al-Raweshidy and S. Komaki, *Radio over Fiber Technologies for Mobile Communications Networks*. Boston: Artech House, 2002.

[11] S. Pappert, R. J. Sun, C.K.and Orazi, and T. E. Weiner, "Photonic link technology for shipboard RF signal distribution," *SPIE Proceedings Photonics and Radio Frequency II*, vol. 3463, pp. 123–134, 1998.

[12] D. Wake, A. Nkansah, N. Gomes, C. Lethien, C. Sion, and J.-P. Vilcot, "Optically powered remote units for Radio-over-Fiber Systems," *J. Lightwave Technol.*, vol. 26, no. 15, pp. 2484–2491, 2008.

[13] S. Montebugnoli, M. Boschi, F. Perini, P. Faccin, G. Brunori, and E. Pirazzini, "Large antenna array remoting using Radio-over-Fiber techniques for radio astronomical application," *Microwave and Optical Techn. Lett.*, vol. 46, pp. 48–54, 2005.

[14] W. Shillue, "Fiber distribution of local oscillator for Atacama large millimeter array," in *Optical Fiber communication/National Fiber Optic Engineers Conference, 2008. OFC/NFOEC 2008. Conference on*, pp. 1–3, 2008.

[15] "The Allen Telescope Array." `http://www.seti.org/ata`.

[16] "Atacama Large Millimeter/submillimeter Array." `http://www.almaobservatory.org`.

[17] "LOFAR website." `http://www.lofar.org`.

[18] "The Square Kilometre Array." `http://www.skatelescope.org/`.

[19] J. Van Campenhout, P. Romeo, D. Van Thourhout, C. Seassal, P. Regreny, L. Di Cioccio, J.-M. Fedeli, and R. Baets, "Design and optimization of electrically injected InP-based microdisk lasers integrated on and coupled to a SOI waveguide circuit," *J. Lightwave Technol.*, vol. 26, pp. 52–63, Jan. 2008.

[20] J. den Besten, R. Broeke, M. van Geemert, J. Binsma, F. Heinrichsdorff, T. van Dongen, E. Bente, X. Leijtens, and M. Smit, "A compact digitally tunable seven-channel ring laser," *IEEE Photon. Technol. Lett.*, vol. 14, pp. 753–755, June 2002.

[21] C. Zah, F. Favire, B. Pathak, R. Bhat, C. Caneau, P. Lin, A. Gozdz, N. Andreadakis, M. Koza, and T. Lee, "Monolithic integration of multiwavelength compressive-strained multiquantum-well distributed-feedback laser array with star coupler and optical amplifiers," *Electron. Lett.*, vol. 28, pp. 2361–2362, Dec. 1992.

[22] L. Ketelsen, J. Grenko, S. Sputz, M. Focht, J. Vandenberg, J. Johnson, C. Reynolds, J. Geary, J. Levkoff, K. Glogovsky, D. Stampone, S. Chu, T. Siegrist, T. Pernell, F. Walters, J. Sheridan-Eng, J.L.Lentz, M. Alam, R. People, M. Hybertsen, E. Isaacs, K. Evans-Lutterodt, R. Leibenguth, G. Przybyiek, L. Zhang, K. Feder, S. Shunk, D. Tennant, L. Peticolas, D. Romero, J. Freund, B. Falk, N. Tzafaras, L. Smith, L. Luther, M. Geva, W. Gault, and J. Zilko, "Multiwavelength DFB laser array with integrated spot size converters," *IEEE J. Quantum Electron.*, vol. 36, pp. 641–648, June 2000.

[23] S. Ménézo, A. Talneau, F. Delorme, S. Grosmaire, F. Gaborit, and S. Slempkes, "10-wavelength 200-GHz spacing emitter integrating DBR lasers with a PHASAR on InP for WDM applications," *IEEE Photon. Technol. Lett.*, vol. 11, pp. 785–787, July 1999.

[24] J. den Besten, R. Broeke, M. van Geemert, J. Binsma, F. Heinrichsdorff, T. van Dongen, E. Bente, X. Leijtens, and M. Smit, "An integrated 4×4-channel multi-wavelength laser on InP," *IEEE Photon. Technol. Lett.*, vol. 15, pp. 368–370, Mar. 2003.

[25] P. Pepeljugoski, D. Kuchta, Y. Kwark, P. Pleunis, and G. Kuyt, "15.6-Gb/s transmission over 1 km of next generation multimode fiber," *IEEE Photon. Technol. Lett.*, vol. 14, pp. 717–719, Mar. 2002.

[26] S. McCall, A. Levi, R. Slusher, S. Pearton, and R. Logan, "Whispering-gallery mode microdisk lasers," *Appl. Phys. Lett.*, vol. 60, no. 3, pp. 289–291, 1991.

[27] J. Hong, M. Cyr, H. Kim, S. Jatar, C. Rogers, D. Goodchild, and S. Clements, "Cascaded strongly gain-coupled (SGC) DFB lasers with 15-nm continuous-wavelength tuning," *IEEE Photon. Technol. Lett.*, vol. 11, pp. 1214–1216, Oct. 1999.

[28] R. Nagarajan, M. Kato, J. Pleumeekers, P. Evans, S. Corzine, S. Hurtt, A. Dentai, S. Murthy, M. Missey, R. Muthiah, R. A. Salvatore, C. Joyner, R. Schneider Jr., M. Ziari, F. Kish, and D. Welch, "InP photonic integrated circuits," *IEEE J. Sel. Topics in Quantum Electron.*, vol. 16, pp. 1113–1125, Sep./Oct. 2010.

[29] V. Jayaraman, Z.-M. Chuang, and L. A. Coldren, "Theory, design, and performance of extended tuning range semiconductor lasers with sampled gratings," *IEEE J. Quantum Electron.*, vol. 29, pp. 1824–1834, June 1993.

[30] A. Ward, D. Robbins, G. Busico, E. Barton, L. Ponnampalam, J. Duck, N. Whitbread, P. Williams, D. Reid, A. Carter, and M. Wale, "Widely tunable DS-DBR laser with monolithically integrated SOA: design and performance," *IEEE J. Sel. Topics in Quantum Electron.*, vol. 11, pp. 149 – 156, Jan. 2005.

[31] M. Zirngibl and C. Joyner, "12 frequency WDM laser based on a transmissive waveguide grating router," *Electron. Lett.*, vol. 30, pp. 701–702, Apr. 1994.

[32] J. den Besten, "Multi-wavelength lasers using AWGs," in *Proc. IEEE/LEOS Annual Meeting (LEOS '03)*, vol. 2, pp. 720–721, Tucson, Arizona, USA, Oct. 26–30 2003. Invited paper.

[33] J. den Besten, R. Broeke, M. van Geemert, J. Binsma, F. Heinrichsdorff, T. van Dongen, E. Bente, X. Leijtens, and M. Smit, "An integrated coupled-cavity 16-wavelength digitally tunable laser," *IEEE Photon. Technol. Lett.*, vol. 14, pp. 1653–1655, Dec. 2002. with correction: vol. 15, p. 353, Feb. 2003.

[34] D. Van Thourhout, L. Zhang, W. Yang, B. Miller, N. Sauer, and C. Doerr, "Compact digitally tunable laser," *IEEE Photon. Technol. Lett.*, vol. 15, pp. 182–184, Feb. 2003.

[35] J. Gallo and R. Whiteman, "Optical modulators for fiber systems," in *Gallium Arsenide Integrated Circuit (GaAs IC) Symposium, 25th Annual Technical Digest 2003. IEEE*, pp. 145–148, 2003.

[36] G. L. Li and P. K. L. Yu, "Optical intensity modulators for digital and analog applications," *J. Lightwave Technol.*, vol. 21, pp. 2010–2030, Sept. 2003.

[37] W.-J. Choi and A. E. Bond, "Low insertion loss and low dispersion penalty InGaAsP quantum-well high-speed electroabsorption modulator for 40-Gb/s," *J. Lightwave Technol.*, vol. 20, pp. 2052–2056, Dec. 2002.

[38] Y. Zhuang, "Peripheral-coupled-waveguide MQW electroabsorption modulator for near transparency and high spurious free dynamic rang RF fiber optic link," *IEEE Photon. Technol. Lett.*, vol. 16, pp. 2033–2035, Sept. 2004.

[39] Y.-S. K. Jeha Kim, "Development and RF characteristics of analog 60-GHz electroabsorption modulator module for RF/optic conversion," *IEEE Transactions on Microwave Theory and Techniques*, vol. 54, pp. 780–787, Feb. 2006.

[40] J.-W. Shi, "Dual-depletion-region electroabsorption modulator with evanescently coupled waveguide for high-speed (>40GHz) and low driving-voltage performance," *IEEE Photon. Technol. Lett.*, vol. 19, pp. 345–347, Mar. 2007.

[41] J. W. Raring, "40-Gb/s widely tunable low-drive-voltage electroabsorption modulated transmitters," *J. Lightwave Technol.*, vol. 25, pp. 239–248, Jan. 2007.

[42] H. Fukano, "Design and fabrication of low-driving-voltage electroabsorption modulators operating at 40 Gb/s," *J. Lightwave Technol.*, vol. 25, pp. 1961–1969, Aug. 2007.

[43] T.-H. Wu, "High speed (60 GHz) and low-voltage-driving electroabsorption modulator using two-consecutive-steps selective-undercut-wet-etching waveguide," *IEEE Photon. Technol. Lett.*, vol. 20, pp. 1261–1263, July 2008.

[44] M. Chaciński, U. Westergren, B. Willen, B. Stoltz, and L. Thylen, "Electroabsorption modulators suitable for 100-Gb/s ethernet," *IEEE Electron Device Lett.*, vol. 29, no. 9, pp. 1014–1016, 2008.

[45] N. Dagli, "Wide-bandwidth lasers and modulators for RF photonics," *IEEE Transactions on Microwave Theory and Techniques*, vol. 47, pp. 1151–1171, July 1999.

[46] Y. Akulova, G. Fish, P. Koh, P. Kozodoy, M. Larson, C. Schow, E. Hall, H. Marchaod, P. Abraham, and L. Coldren, "10 Gb/s Mach-Zehnder modulator integrated with widely-tunable sampled grating DBR laser," in *Techn. Digest Opt. Fiber Comm. (OFC '04)*, San Jose, California, USA, Feb. 23–27 2004.

[47] S. Akiyama, "Wide-wavelength-band (30 nm) 10 Gb/s operation of InP-based Mach-Zehnder modulator with constant driving voltage of 2 Vpp," *IEEE Photon. Technol. Lett.*, vol. 17, pp. 1408–1410, July 2005.

[48] H. Klein, H. Chen, D. Hoffmann, S. Staroske, A. Steffan, and K.-O. Velthaus, "1.55 μm Mach-Zehnder modulators on InP for optical 40/80 Gbit/s transmission networks," in *Proc. IPRM conference*, pp. 171–173, Princeton, New Jersey USA, May 7–11 2006.

[49] T. Yasui, "10-Gb/s 100-km SMF transmission using InP Mach-Zehnder modulator monolithically integrated with semiconductor optical amplifier," *IEEE Photon. Technol. Lett.*, vol. 20, pp. 1178–1180, July 2008.

[50] S. Akiyama, H. Itoh, S. Sekiguchi, S. Hirose, T. Takeuchi, A. Kuramata, and T. Yamamoto, "InP-based Mach-Zehnder modulator with capacitively loaded traveling-wave electrodes," *J. Lightwave Technol.*, vol. 26, pp. 608–615, Mar. 2008.

[51] K. Tsuzuki, "Full C-band Mach-Zehnder modulators for telecom applications," *IEEE J. Quantum Electron.*, vol. 15, pp. 521–527, May 2009.

[52] R. Walker, "High-speed III-V semiconductor intensity modulators," *IEEE J. Quantum Electron.*, vol. 27, no. 3, pp. 654–667, 1991.

[53] B. Liu, J. S. Y. en Chiu, A. Keating, J. Piprek, and J. E. Bowers, "Analog characterization of low-voltage MQW traveling-wave electroabsorption modulators," *J. Lightwave Technol.*, vol. 21, pp. 3011–3019, Dec. 2003.

[54] J. S. Barton, *The integration of Mach-Zehnder modulator with Sampled Grating DBR*. PhD thesis, University of California Santa Barbara, Santa Barbara, The USA, 2004.

[55] A. Liu, M. J. Paniccia, and R. Jones, *Transmitter-receiver with integrated modulator array and hybrid bonded multi-wavelength laser array*. US Patent No. 7,257,283 B1, 2007.

[56] M. Kato, R. Nagarajan, J. Pleumeekers, P. Evans, A. Chen, A. Mathur, A. Dentai, S. Hurtt, D. Lambert, P. Chavarkar, M. Missey, J. Bäck, R. Muthiah, S. Murthy, R. Salvatore, C. Joyner, J. Rossi, R. Schneider, M. Ziari, F. Kish, and D. Welch, "40-channel transmitter and receiver photonic integrated circuits operating at per channel data rate 12.5 Gbit/s," *Electron. Lett.*, vol. 43, Apr. 2007.

[57] J. Zhao, D. Lenstra, R. Santos, M. Wale, M. Smit, and X. Leijtens, "Feedback phase influence on an integrated filtered-feedback laser," *IEEE Photon. Technol. Lett.*, vol. 24, no. 23, pp. 2195–2197, 2012.

[58] J. Zhao, E. Kleijn, P. Williams, M. Smit, and X. Leijtens, "On-chip laser with multimode interference reflectors realized in a generic integration platform," in *Compound Semiconductor Week (CSW/IPRM), 2011 and 23rd International Conference on Indium Phosphide and Related Materials*, pp. 1–4, 2011.

[59] J. Zhao, P. J. Williams, M. K. Smit, and X. Leijtens, "Monolithic integrated filtered-feedback multi-wavelength laser," in *Techn. Digest Opt. Fiber Comm. (OFC/NFOEC '12)*, p. OM3E.3, Los Angeles, CA, USA, Mar. 2012.

[60] J. Zhao, D. Lenstra, R. Lemos Alvares Dos Santos, M. Wale, M. Smit, and X. Leijtens, "Stability of a monolithic integrated filtered-feedback laser," *Optics Express*, vol. 20, pp. B270–B278, Sept. 2012.

[61] M. Smit, "New focusing and dispersive planar component based on an optical phased array," *Electron. Lett.*, vol. 24, no. 7, pp. 385–386, 1988.

[62] A. Vellekoop and M. Smit, "Low-loss planar optical polarisation splitter with small dimensions," *Electron. Lett.*, vol. 25, no. 15, pp. 946–947, 1989.

[63] A. Vellekoop and M. Smit, "Four-channel integrated-optic wavelength demultiplexer with weak polarization dependence," *J. Lightwave Technol.*, vol. 9, no. 3, pp. 310–314, 1991.

[64] M. Smit and C. van Dam, "PHASAR-based WDM-devices: principles, design and applications," *J. of Sel. Topics in Quantum Electron.*, vol. 2, pp. 236–250, June 1996.

[65] C. Joyner, C. Doerr, L. Stulz, M. Zirngibl, and J. Centanni, "Low-threshold nine-channel waveguide grating router-based continuous wave transmitter," *J. Lightwave Technol.*, vol. 17, pp. 647–651, Apr. 1999.

[66] N. Dutta, N. Olsson, L. Koszi, P. Besomi, R. Wilson, and R. Nelson, "Frequency chirp under current modulaton in InGaAsP injection lasers," *J. Appl. Phys.*, vol. 56, no. 7, pp. 2167–2169, 1984.

[67] B. Docter, J. Pozo, S. Beri, I. Ermakov, J. Danckaert, M. Smit, and F. Karouta, "Discretely tunable laser based on filtered feedback for telecommunication applications," *IEEE J. Sel. Topics in Quantum Electron.*, vol. 16, no. 5, pp. 1405–1412, 2010.

[68] B. Docter, E. Geluk, M. Sander-Jochem, F. Karouta, and M. Smit, "Deep etched DBR gratings in InP for photonic integrated circuits," in *Proc. IPRM conference*, pp. 226–228, Matsue, Japan, 2007.

[69] E. Kleijn, M. Smit, and X. Leijtens, "Multimode interference reflectors: a new class of components for photonic integrated circuits.," *J. Lightwave Technol.*, 2013. doi:10.1364/AO.51.000789.

[70] P. Muñoz, R. García-Olcina, J. Doménech, M. Rius, J. Capmany, L. Chen, C. Habib, X. Leijtens, T. de Vries, M. Heck, L. Augustin, R. Nötzel, and D. Robbins, "Multi-wavelength laser based on an arrayed waveguide grating and Sagnac loop reflectors monolithically integrated on InP," in *Proc. 15th Eur. Conf. on Int. Opt. (ECIO '10)*, p. WeF2, Cambridge, UK, Apr. 2010.

[71] F. Pockels, *Lehrbuch der Kristalloptik.* Leipzig, Teubner, 1 ed., 1906.

[72] D. Miller, D. Chemla, A. Damen, T.C.and Gossard, and W. Wiegmann, "Band-edge Electro-absorption in Quantum Well Structures: The Quantum Confined Stark Effect," *Phys. Rev. Lett.*, vol. 53, pp. 2173–2177, 1984.

[73] U. Koren, T. Koch, H. Presting, and B. Miller, "InGaAs/InP multiple quantum well waveguide phase modulator," *Appl. Phys. Lett.*, vol. 50, no. 7, pp. 368–370, 1987.

[74] R. Nagarajan, M. Kato, V. Dominic, C. Joyner, R. Schneider, A. Dentai, T. Desikan, P. Evans, M. Kauffman, D. Lambert, S. Mathis, A. Mathur, M. Mitchell, M. Missey, S. Murthy, A. Nilsson, F. Peters, J. Pleumeekers, R. Salvatore, R. Taylor, M. Van Leeuwen, J. Webjorn, M. Ziari, S. Grubb, D. Perkins, M. Reffle, D. Mehuys, F. Kish, and D. Welch, "400 Gbit/s (10 channel ×40 Gbit/s) DWDM photonic integrated circuits," *Electron. Lett.*, vol. 41, pp. 347 – 349, Mar. 2005.

[75] M. Smit, X. Leijtens, E. Bente, J. Van der Tol, H. Ambrosius, D. Robbins, M. Wale, N. Grote, and M. Schell, "Generic foundry model for InP-based photonics," *Optoelectronics, IET*, vol. 5, no. 5, pp. 187–194, 2011.

[76] "Joint European platform for InP-based photonic integrated components and circuits." `http://www.jeppix.eu`.

[77] X. J. M. Leijtens, "JePPIX: the platform for InP-based photonics," *IET Optoelectronics*, vol. 5, no. 5, pp. 202–206, 2011.

[78] "EU FP7 project EuroPIC: the European manufacturing platform for Photonic Integrated Circuits." `http://europic.jeppix.eu`.

[79] "EU FP7 project PARADIGM: Photonic Advanced Reseach And Development for Integrated Generic Manufacturing." `http://paradigm.jeppix.eu`.

[80] M. Smit, R. Baets, and M. Wale, "InP-based photonic integration: Learning from CMOS," in *Proc. 35th Eur. Conf. on Opt. Comm. (ECOC '09)*, Vienna, Austria, Sep. 20–24 2009.

[81] M. Maximov, E. Ramushina, V. Skopina, E. Tanklevskaya, V. Solov'ev, Y. Shernyakov, I. Kaiander, M. Kaliteevski, S. Gurevich, N. Ledentsov, V. Ustinov, Z. Alferov, C. Sotomayor Torres, and D. Bimberg, "Edge-emitting InGaAs/GaAs lasers with deeply etched semiconductor/air distributed bragg reflector mirrors," *Semicond. Sci. Technol.*, vol. 17, pp. 69–71, 2002.

[82] P. Muñoz, R. García-Olcina, C. Habib, L. Chen, X. Leijtens, T. de Vries, M. Heck, L. Augustin, R. Notzel, and D. Robbins, "Sagnac loop reflector and arrayed waveguide grating-based multi-wavelength laser monolithically integrated on InP," *IET Optoelectronics*, vol. 5, no. 5, pp. 207–210, 2011.

[83] Y. Zheng, D. Keh-Ting Ng, Y. Wei, W. Yadong, Y. Huang, Y. Tu, C.-W. Lee, B. Liu, and S.-T. Ho, "Electrically pumped heterogeneously integrated Si/III-V evanescent lasers with micro-loop mirror reflector," *Appl. Phys. Lett.*, vol. 99, no. 1, p. 011103, 2011.

[84] L. Xu, X. Leijtens, B. Docter, T. de Vries, E. Smalbrugge, F. Karouta, and M. Smit, "MMI-reflector: A novel on-chip reflector for photonic integrated circuits," in *Proc. 35th Eur. Conf. on Opt. Comm. (ECOC '09)*, Vienna, Austria, Sep. 20–24 2009.

[85] E. Kleijn, M. Smit, M. Wale, and X. Leijtens, "New two-port multimode interference reflectors," in *Proc. 16th Eur. Conf. on Int. Opt. (ECIO '12)*, Sitges, Spain, Apr. 2012.

[86] L. Soldano and E. Pennings, "Optical multi-mode interference devices based on self-imaging: Principles and applications," *J. Lightwave Technol.*, vol. 13, pp. 615–627, Apr. 1995.

[87] D. M. Sullivan, *Electromagnetic Simulation Using the FDTD Method*, vol. ISBN: 978-0-7803-4747-2. Wiley-IEEE Press, July 2000.

[88] P.-A. Besse, J.-S. Gu, and H. Melchior, "Reflectivity minimization of semi-conductor laser amplifiers with coated and angled facets considering two-dimensional beam profiles," *IEEE J. Quantum Electron.*, vol. 27, pp. 1830–1836, June 1991.

[89] L. Coldren and S. Corzine, "Diode lasers and photonic integrated circuits," in *Wiley Series in Microwave and Optical Engineering*, John Wiley & Sons Inc., New York, USA, 2005. ISBN 0-471-11875-4.

[90] D. Ackerman, L. Zhang, L.-P. Ketelsen, and J. Johnson, "Characterizing residual reflections within semiconductor lasers, integrated sources, and coupling optics," *IEEE J. Quantum Electron.*, vol. 34, pp. 1224–1230, July 1998.

[91] L. Olofsson and T. Brown, "On the linewidth enhancement factor in semiconductor lasers," *Appl. Phys. Lett.*, vol. 57, no. 26, pp. 2773–2775, 1990.

[92] J. Ehrhardt, A. Villeneuve, G. Stegeman, H. Nakajima, J. Landreau, and A. Ougazzaden, "Interferometric measurement of the linewidth enhancement factor of a 1.55μm strained multiquantum-well InGaAs/InGaAsP amplifier," *IEEE Photon. Technol. Lett.*, vol. 4, no. 12, pp. 1335–1338, 1992.

[93] H. Li, "RF-modulation measurement of linewidth enhancement factor and nonlinear gain of vertical-cavity surface-emitting lasers," *IEEE Photon. Technol. Lett.*, vol. 8, no. 12, pp. 1594–1596, 1996.

[94] T. Newell, D. Bossert, A. Stintz, B. Fuchs, K. Malloy, and L. Lester, "Gain and linewidth enhancement factor in InAs quantum-dot laser diodes," *IEEE Photon. Technol. Lett.*, vol. 11, no. 12, pp. 1527–1529, 1999.

[95] K. Iiyama, K. Hayashi, and Y. Ida, "Simple method for measuring the linewidth enhancement factor of semiconductor lasers by optical injection locking," *Opt. Lett.*, vol. 17, no. 16, pp. 1128–113, 1992.

[96] D. Lenstra and W. van der Graaf, "Diode lasers with optical feedback and injection: similarities and differences," in *Proc. IEEE/LEOS Annual Meeting*, vol. 2, pp. 343–344, 1996.

[97] I. Petitbon, P. Gallion, G. Debarge, and C. Chabran, "Locking bandwidth and relaxation oscillations of an injection-locked semiconductor laser," *IEEE J. Quantum Electron.*, vol. 24, pp. 148–154, Feb. 1988.

[98] C. Henry, N. Olsson, and N. Dutta, "Locking range and stability of injection locked 1.54μm InGaAsP semiconductor lasers," *IEEE J. Quantum Electron.*, vol. 21, no. 8, pp. 1152–1156, 1985.

[99] R. Lang, "Injection locking properties of a semiconductor laser," *IEEE J. Quantum Electron.*, vol. 18, pp. 976–983, June 1982.

[100] J. Zhao, P. Williams, M. Smit, and X. Leijtens, "Monolithic integrated filtered-feedback multi-wavelength laser," in *Techn. Digest Opt. Fiber Comm. (OFC '12)*, Los Angeles, CA, USA, Mar. 2012.

[101] P. Kuindersma. Private communication, December 2011.

[102] C. Doerr, M. Shirasaki, and C. Joyner, "Chromatic focal plane displacement in the parabolic chirped waveguide grating router," *IEEE Photon. Technol. Lett.*, vol. 9, pp. 625 –627, May 1997.

[103] C. Henry, "Phase noise in semiconductor lasers," *J. Lightwave Technol.*, vol. 4, pp. 298 – 311, Mar. 1986.

[104] G. Agrawal, "Line narrowing in a single-mode injection laser due to external optical feedback," *IEEE J. Quantum Electron.*, vol. 20, pp. 468 – 471, May 1984.

[105] T. Okoshi, K. Kikuchi, and A. Nakayama, "Novel method for high resolution measurement of laser output spectrum," *Electron. Lett.*, vol. 16, pp. 630 –631, 31 1980.

[106] M. Yousefi and D. Lenstra, "Dynamical behavior of a semiconductor laser with filtered external optical feedback," *IEEE J. Quantum Electron.*, vol. 35, pp. 970 –976, June 1999.

[107] G. van Tartwijk and D. Lenstra, "Semiconductor lasers with optical injection and feedback," *Quantum and Semiclassical Optics: Journal of the European Optical Society Part B*, vol. 7, pp. 87 –143, 1995.

[108] G. Acket, D. Lenstra, A. Den Boef, and B. Verbeek, "The influence of feedback intensity on longitudinal mode properties and optical noise in index-guided semiconductor lasers," *IEEE J. Quantum Electron.*, vol. 20, pp. 1163 – 1169, Oct. 1984.

[109] J. Mork, B. Tromborg, and J. Mark, "Chaos in semiconductor lasers with optical feedback: theory and experiment," *IEEE J. Quantum Electron.*, vol. 28, pp. 93 –108, Jan. 1992.

[110] S. Strogatz, *Nonlinear Dynamics and Chaos: With Applications to Physics, Biology, Chemistry, and Engineering*. Westview Press, 1 ed., 2001. ISBN : 0738204536.

[111] D. Lenstra, B. Verbeek, and A. Den Boef, "Coherence collapse in single-mode semiconductor lasers due to optical feedback," *IEEE J. Quantum Electron.*, vol. 21, pp. 674–679, June 1985.

[112] C. Lim, A. Nirmalathas, M. Attygalle, D. Novak, and R. Waterhouse, "The merging of a WDM fiber-radio backbone with a 25 GHz WDM ring network," in *Microwave Symposium Digest, 2003 IEEE MTT-S International*, vol. 1, pp. 273 – 276, June 2003.

[113] M. Burla, C. Roeloffzen, L. Zhuang, D. Marpaung, R. Khan, P. Maat, K. Dijkstra, A. Leinse, M. Hoekman, and R. Heideman, "System integration and radiation pattern measurements of a phased array antenna employing an integrated photonic beamformer for radio astronomy applications," *Appl. Opt.*, vol. 51, p. 789, Mar. 2012.

[114] C. H. Cox III, *Analog Optical Links: Theory and Practice*. Cambridge University Press, 1 ed., 2006. ISBN : 9780521027786.

[115] L. A. Coldren and S. W. Corzine, *Diode lasers and photonics integrated circuits*. New York, USA,: P45, John Wiley& sons, 1 ed., 1995.

[116] M. Sisodia and V. L. Gupta, *Microwaves : Introduction to Circuits, Devices and Antennas*. New Age International Ltd., 1 ed., 2001. ISBN : 9788122413380.

[117] G. B. Thomas, *Calculus and Analytic Geometry*. Addison-Wesley Publishing Co., 1968.

[118] J. Bagrowski, J. Konsowski, S., and G. Spencer, "Interconnection of monolithic integrated circuits through the use of advanced materials and techniques," *IEEE Transactions on Parts, Materials and Packaging*, vol. 2, no. 4, pp. 90–98, 1966.